공학박사 학위논문

Finite element based virtual fields method for identifying constitutive parameters

구성방정식 재료상수 결정을 위한 유한요소 기반 가상필즈법 개발

2021 년 8 월

서울대학교 대학원
재료공학부
김 찬 양

Finite element based virtual fields method for identifying constitutive parameters

구성방정식 재료상수 결정을 위한 유한요소 기반 가상필즈법 개발

지도 교수 이 명 규

이 논문을 공학박사 학위논문으로 제출함
2021 년 7 월

서울대학교 대학원
재료공학부
김 찬 양

김찬양의 공학박사 학위논문을 인준함
2021 년 7 월

위 원 장 _____ 유 웅 열 _____

부위원장 _____ 이 명 규 _____

위 원 _____ 한 흥 남 _____

위 원 _____ 김 대 용 _____

위 원 _____ 김 진 환 _____

Abstract

In this study, a novel virtual fields method (VFM) based on the finite element (FE) scheme, namely FE-VFM, is proposed as an inverse method for identifying the parameters of constitutive models. In the FE-VFM, experimentally measured full-field displacements are mapped onto FE meshes using global and local shape functions, and the internal virtual work is integrated using the Gauss quadrature rule.

To validate the new method, a well-designed sensitivity study is conducted using the ideal deformation obtained from FE simulations for anisotropic linear elastic and isotropic plastic materials. In the case of anisotropic elasticity, the residuals of the internal and external virtual work are not significantly affected by the order and size of FE meshes, and the order of the numerical integration has a marginal effect on the quality of the results. Conversely, substantial impacts are obtained for the plastic case, in which the size and order of the FE meshes and the order of the numerical integration are all critical to the accuracy of identification owing to large, localized deformation.

As an applications of the FE-VFM, homogeneous and nonhomogeneous strain hardening of the metal sheets were identified. The first application is identifying homogeneous strain hardening of the advanced hardening. Additional to the FE-VFM, the concept of a pseudo-real deformation field is

newly proposed as a virtual field, which improves the accuracy of the FE-VFM for optimizing the constitutive parameters of the plastic material. Finally, the inverse identification of the plastic hardening law for press-hardened steel is conducted using the FE-VFM with real experimental data. The results show that the FE-VFM can successfully reproduce the full-field displacements even with relatively low-quality full-field data if an optimum FE mesh is adopted. In addition, the results of the U-notch tensile tests were performed for the validation of the FE-VFM results, and the simulated load–displacement curve of U-notch tests with strain hardening identified by FE-VFM is in good agreement with the experimental results

As an advanced application, the FE-VFM was applied for identifying nonhomogeneous strain hardening of the friction stir welded aluminum alloy sheets. In this study, weld affected zone (WAZ) boundary was identified first, then, local flow stresses were identified in the WAZ. In addition, the area of interest was divided into subdomains, and FE-VFM was applied to each subdomain independently, to avoid a uniqueness problem. Also, material constants in each subdomain are interpolated with a quadratic function. To uniquely identify the interpolated material parameters, three independent normal distribution type virtual fields were used. These numerical approaches were validated through feasibility tests based on FE simulation data, then, the validated method was applied to identify the local flow stresses of the friction stir welded AA6061-T6 sheets. The friction stir welding was conducted with

two tool rotation speed conditions, 1200 and 1600 RPM. FE-VFM could successfully identify the boundary of the WAZ and distributions of the strain hardening parameters in the WAZ. Also, tensile tests were conducted for the validation of the identified non-homogeneous strain hardening parameters, and the predictions using FE-VFM results were in good agreement with experiments.

Keywords: Virtual fields method; Finite element; Smooth full-field measurement; Constitutive model; Plastic strain hardening; non-homogeneous local properties

Student number: 2018-39025

Contents

List of Tables

List of Figures

1. Introduction

1.1. Conventional method for identifying constitutive parameters

In modern solid mechanics, numerical simulations are widely used for solving various engineering problems. In many cases, the accuracy of the simulations is highly dependent on the capability of constitutive laws and the exact identification of their model parameters. Conventionally, mechanical tests that introduce uniform deformations in well-designed standard specimens are commonly used to investigate the mechanical behavior of materials (for instance, by using standard tensile tests). These tests can determine the values of stress components under proportional loading conditions, and deformation is often measured by contact-type sensors, such as a strain gauge or an extensometer.

Fig. 1-1 shows an example of the standard tensile tests with a mechanical extensometer. In conventional tensile tests, Applied (resultant) load is measured by the load cell of the test machine. Also, strains in loading (or longitudinal) direction are measured by a mechanical extensometer, as shown in Fig. 1-1(a). If strains in the transverse direction are required, two different types of mechanical extensometers are attached in the gauge of the specimen. There are several standards for the tensile test including ASTM international, ISO, or KS. Also, specimen geometries can vary for the different types of materials. Fig. 1-1(b) and (c) shows the ASTM standard specimens for fiber-

reinforced composites [1], and metal sheets [2], respectively.

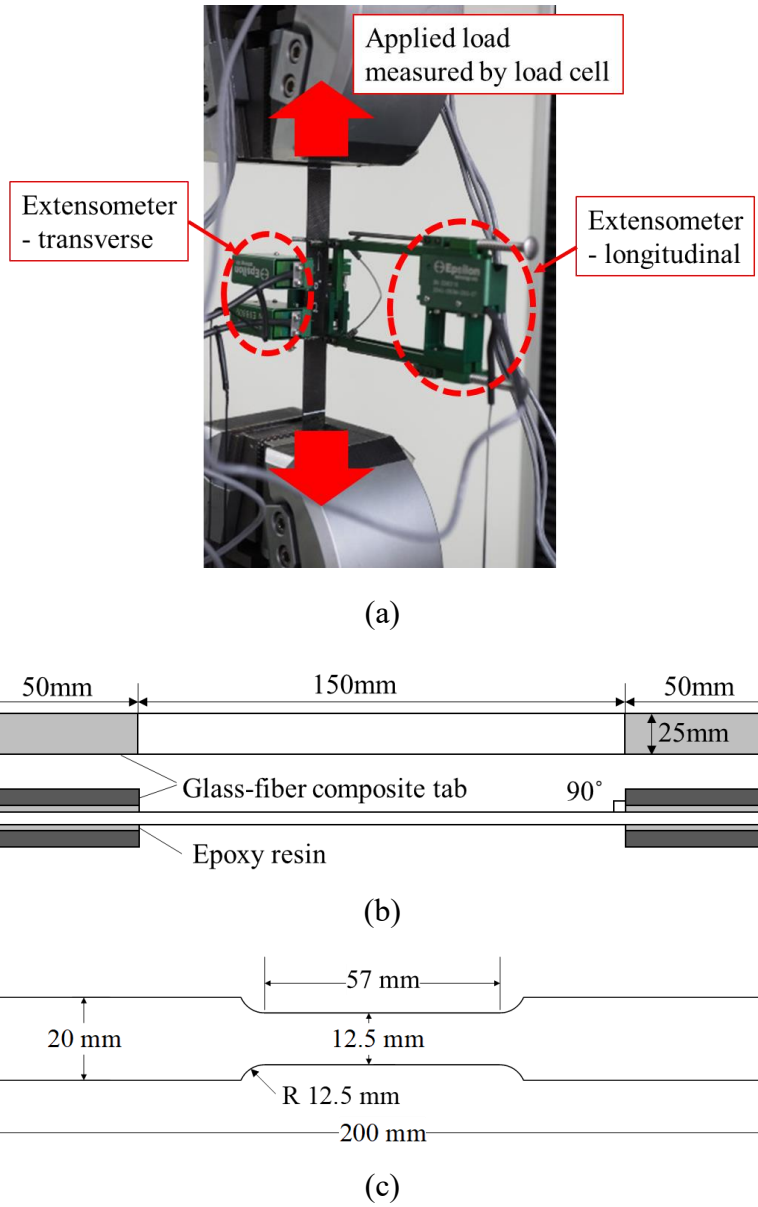

Fig. 1-1. Example of standard tensile tests. (a) is an illustration of tensile tests setup, (b) and (c) are standard specimen geometries for fiber-reinforced composite sheets [2] and metal sheets [1], respectively.

After obtaining direct stress–strain relation using conventional mechanical tests, constitutive parameters are calculated based on these experimental data. In that process, mathematical fitting [3,4], analytical calculation [5], or numerical optimization [6,7] methods are used depends on constitutive law.

Although conventional strain measurement methods are efficient and effective, they cannot measure the full deformation field in the region of interest. Accordingly, the parameters of constitutive models are also identified from the relationship between stress and strain under the assumption of homogeneous deformation and proportional loading. Conventional approaches may not be efficient for identifying the parameters of modern complex constitutive models for describing anisotropic and/or non-proportional mechanical properties. For instance, multiple tensile tests for the different material orientations are required to obtain the anisotropy of materials [8–11]. In addition, complex geometry and specially designed types of equipment are needed for tension-shear tests [12,13] or to introduce a multi-axial stress state such as biaxial tension [14,15].

1.2. Full-field measurement and the virtual fields method

As alternatives to conventional strain measurements, non-contact full-field measurements [16] enable the acquisition of displacement fields on the specimen surface. Various technique can measure full-field displacements

such as the speckle photography [17,18], grid method [19,20], Moiré interferometry [21,22], electronic speckle pattern interferometry (EPSI) [23,24], and digital image correlation (DIC) [25–27]. These techniques utilize the optical pattern and measure the displacements on the surface of the specimen. Speckle photography uses the pattern of the distribution of the scattered wave due to the rough surface of the specimen illuminated with coherent light. In the grid method, regular grid lines are marked on the surface of the specimen, and it measured the displacements and strains by analyzing Moiré fringes formed by regular grid marks. Moiré interferometry is based on the same phenomenon used in the grid method, but it utilizes the interference and fringes of the two coherent laser beams rather than the fringe due to the physical grid mark. EPSI uses the scattered light from the surface added to the reference laser beam.

Among these techniques, DIC is one of the most widely used techniques, and various commercial software–hardware packages are available in the global market. The DIC uses the physical speckle pattern usually made by spray paint, and it measures the displacements by correlating the undeformed and deformed spackle patterns in the digital photos. Fig. 1-2 shows the procedure for a mechanical test with the DIC. Fig. 1-2(a) illustrates the experimental setup with the DIC. In the tests, grayscale photos are taken for the spackle patterns on the specimen in the area of interest (AOI), during the mechanical tests. For the 2D-DIC, only a single camera is used, whereas

stereo-DIC uses at least two cameras with a different camera orientation, as shown in Fig. 1-2(a). The 2D-DIC cannot consider the out-of-plane motion of the specimen, hence it requires that the orientation of the camera should be perpendicular to the flat specimen plane. The stereo-DIC uses two or more photos with a different camera orientation to account for the out-of-plane motion (or position) of the surface. Also, recognition of the camera position—which includes the angle between cameras, the distance between cameras, etc.—is required, and it is called “calibration”.

Fig. 1-2(b) illustrates the schematics of the DIC post-processing. In this process, AOI is divided into smaller image regions with a size of n×n pixels, which are called the subset. Then, tracking of the spackle pattern is conducted through the different time frames, and the displacements are obtained based on the shape functions. In this process, several different matching criteria are used including the normalized sum of squared difference (NSSD), zero normalized sum of squared difference (ZNSSD), etc. Note that these post-processing options—the size of the subset, types of matching criterion, or the order of the shape functions—affect the quality of the DIC results, especially the resolution and the noise [27–29]. After the post-processing, displacement fields are calculated in the AOI, as shown in Fig. 1-2(c). Other kinematic values such as strains are calculated based on these displacements.

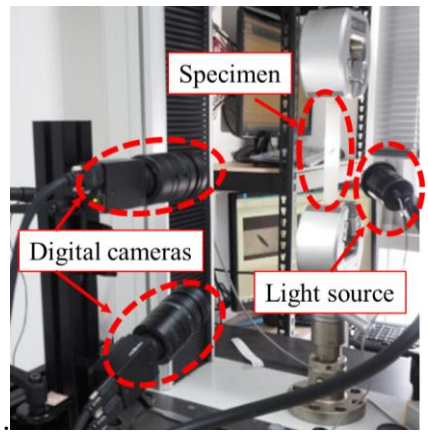

(a)

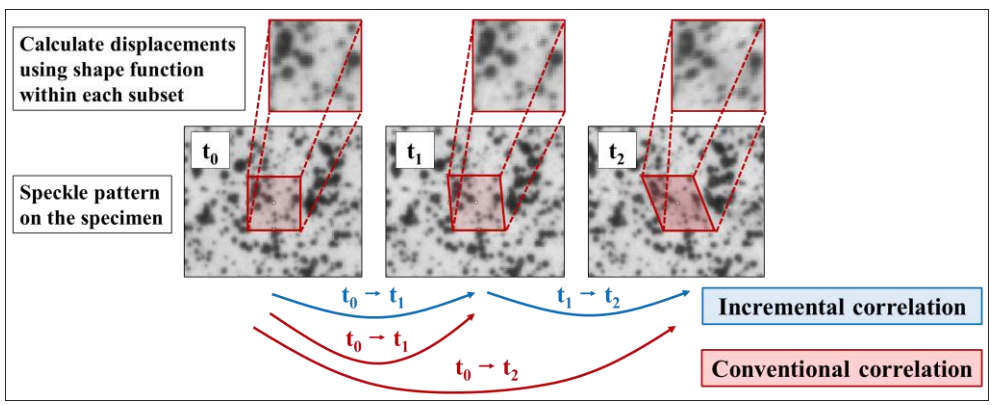

(b)

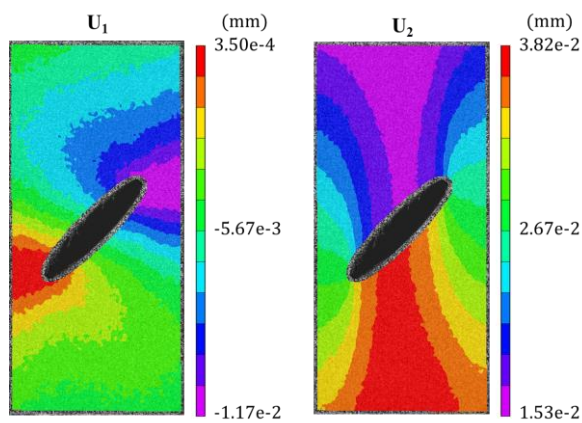

(c)

Fig. 1-2. Procedure for a mechanical test with the DIC. (a) Experimental setup, (b) schematics of DIC post-processing, and (c) example of displacements measured by DIC

New strategies for identifying the material parameters of constitutive laws with full-field measurements have been developed [30]. These new technologies include the virtual field method (VFM) [31,32], the finite element (FE) updating method (FEUM) [33–36], the constitutive equation gap method (CEGM) [37,38], the equilibrium gap method (EGM) [39,40]. Recently, researchers also investigated inversely optimizing the constitutive parameters using machine learning [41]. These non-conventional inverse identification approaches have overcome the limitations of conventional mechanical testing. Among these non-conventional approaches, the VFM utilizes the entire full-field measurement as an input to the governing equations, the principle of virtual work (PVM). The VFM has been successfully used to identify the constitutive model parameters of various solid and soft materials, such as linear elastic [42–44], hyper-elastic [45,46], viscoelastic [47], and elastic–plastic materials [48–50], under static or dynamic loading conditions [51,52]. Recently, Yunquan et al. used VFM to determine the material parameters of the thermo-mechanical model of the composites [53].

One of the benefits of the VFM (or other inverse methods) compared to conventional mechanical tests is that anisotropic material properties can be identified simultaneously with a single test. For this purpose, The VFM can use the non-homogeneous deformation and/or non-proportional loading data obtained by full-field measurement. Rather, the application of complex strain

(or stress) states is recommended during the mechanical tests to enrich the required (anisotropic) experimental data. Inducing non-homogeneous and complex strain states in the specimen requires specially designed non-uniform specimens. For identifying anisotropic linear elastic constants, researchers investigated using various specimen geometries including the un-notched Iosipescu shear tests [54], thick ring compression tests [55], plate bending tests [56,57], and tensile tests with an elliptic cut hole [44]. For the identification of anisotropic plastic constitutive parameters, various tests including notched tensile tests [58], tensile tests with rotated M shape specimens [59], and biaxial tests [60] were used.

Virtual fields—which are arbitrary test functions that satisfy the prescribed boundary conditions—play an important role in the quality of the VFM. Depending on the selection of virtual fields, the effect of experimental noise can be filtered, and meaningful data from the full-field measurement can be amplified. Therefore, special virtual fields [61–63] have been suggested for the linear elastic problem. Toussaint et al. proposed the piecewise virtual fields [64]. In this formulation, virtual fields are defined as polynomial shape functions within a subdomain similar to the FEM. Also, sensitivity-based virtual fields [65–67] have recently been developed for plastic materials.

Meanwhile, most of the studies of the VFM application were based on the 2D membrane deformation or the plane stress condition assumption. It is because that most of the full-field measurement techniques can only measure

in-plane displacements. In a theoretical aspect, the VFM can be applied to general 3D problems. Rossi and Pierron demonstrated the theoretical capability of VFM in 3D stress states using 3D displacements generated by FEM [68]. In a real application, an advanced full-field measurement technique is required to measure the 3D displacement fields such as digital volume correlation (DVC) based on x-ray tomography or MRI [69–71]. However, such techniques are not readily accessible, and the in-plane displacements on the outer surface of the specimen can only be measured even with stereo-DIC. As a result, the VFM can be used for the thin enough materials, so strains (or stresses) in the thickness direction can be ignored, and it can be assumed that strains are uniform through the thickness, in a practical sense.

1.3. Smoothing of the full-field measurement

The accuracy of the material properties identified using the VFM highly depends on the quality of the full-field measurement [31,72]. One of the challenges of full-field measurements is the inevitable noise and artifacts caused by its non-contact approach. In many cases, the constitutive laws in solid mechanics are described by the stress–strain relation [11,73–75]. In the full-field measurement approach, strains are calculated from the gradient of displacements (or velocity gradient), and the signal-to-noise ratio can be

significantly decreased during this process. Subsequently, the noise in the full-field measurement is another important factor in determining the quality of the VFM [72].

To reduce the noise in the full-field measurement, various smoothing algorithms have been developed. Among them, local smoothing has been widely used in strain calculation and is available in commercial software [27,76,77]. Local smoothing has been effective in reducing the noise of full-field measurement, but it requires prior knowledge and experience in the determination of algorithmic parameters such as smoothing level and filter size. Instead of local smoothing, global spatial smoothing based on the FE approach has also been used for noise reduction. In this approach, displacements are mapped onto FE meshes with the proper interpolations, and strains are calculated from the derivatives of the interpolation functions. Chen et al. and Tiren et al. used a linear quadrilateral element for the calculation of strain from displacements measured by DIC [33,78], while Yoneyama implemented a quadratic quadrilateral element [79]. Zhao et al. used Hermite FE interpolation for the full-field strain measurement over an arbitrary region of interest in DIC [80].

In previous studies on the VFM, a linear triangular FE has been generally used for global smoothing, mainly because of its simple implementation [49,81,82]. Another purpose of global smoothing is to fill the empty edges of the area of interest (AOI) when DIC is used. DIC is a powerful tool for

measuring the large deformation of elastic-plastic or hyper-elastic materials. Moreover, DIC is readily available in commercial software and hardware packages. However, the disadvantage of DIC is that there may be missing data at the edge of the AOI, in particular for the subset-based DIC. Subset based DIC technique requires a perfect (nxn) pixel rectangular subset. However, at the edge of the AOI, a perfect subset cannot be made, and deformation cannot be given during the post-processing [83]. Therefore, empty data at the edge should be restored when applying VFM, and data at the edge of the AOI are reconstructed using the FE. However, the strains are constant in a linear triangular element, which requires relatively fine meshes if the deformation is highly localized. However, fine linear triangular FE mesh may lead to a lower level of smoothing. For this reason, Kim et al. employed both global and local polynomial smoothing when they employed linear triangular elements. They also presented a comprehensive sensitivity study on the effect of FE mesh size and the order of polynomials for obtaining reliable VFM results [81].

1.4. Integration of the internal virtual work in the VFM

The VFM formulations presented in previous studies are limited in terms of the numerical integration of the internal virtual work (IVW). In most VFM studies, a primitive discretized sum was used for the integration of the IVW

[31,32,46,61–63,65–67,84]. Although it is simple to implement, it might be computationally inefficient, especially when deformation is highly localized and a large number of data points are required for an accurate integration. Also, the accuracy of the IVW integration might be reduced when fewer integration points are used with highly non-linear virtual fields. Another defect of the local discretized sum approach is that it is not computationally inefficient in terms of the stress update process in the identification of the plastic constitutive parameters. In that application, the stress update procedure is the most time-consuming step since multiple iterations are required for the accurate stress update with advanced plasticity constitutive laws [6,85–88]. Due to this, a large number of data points in the IVW integration with the discretized sum might require a large computational cost.

Usually, numerical integration such as Gauss quadrature is implemented on the conventional FEM. Though the finite element shape functions are applied in the global smoothing of the full-field measurement, advanced numerical integration schemes implemented on the FEM are not used in the VFM. In other words, only the shape functions are borrowed from the FE formulations as a global target function for the smoothing of the measured deformation fields. It can be numerically efficient and effective that implementing advanced numerical integration on the VFM with a higher-order global smoothing. However, in the previous literature, displacement fields are described with global coordinates functions because only the global position

of the measured data points are known values, whereas the deformation fields should be described in the regular natural coordinates space for implementing most of the advanced numerical integration.

1.5. Research objective

In this study, a novel virtual fields method (VFM), namely an FE-based VFM (hereafter, FE-VFM), is proposed. The purpose and strength of the FE-VFM are described as follows: First, for the smoothing of the full-field measurement, displacement fields are mapped or reconstructed into FE meshes using the local and global higher-order shape functions. In this process, global coordinates are converted into regular local (or natural coordinates), and nodal displacements of the FE meshes are obtained using linear least square operation. Therefore, the displacement fields can be described only with nodal values and interpolation (or shape) functions. The reconstruction procedure is formulated for general types of FEs. Second, the Gauss–Legendre quadrature is employed in the numerical integration of IVW to increase the numerical efficiency and accuracy. More details of the FE-VFM formulations are given in Chapter 2.

In Chapter 3, a sensitivity study on the FE mesh size, type of element, and integration order is provided to validate the efficiency and accuracy of the proposed FE-VFM. The sensitivity tests were based on the ideal deformation

fields that are obtained by FE simulations and conducted for both orthotropic linear elastic and elastic-plastic material cases. For the quantitative analysis, errors between internal and external virtual works were evaluated based on target constitutive parameters.

As an application, homogeneous and non-homogeneous strain hardening laws of the metal sheets are identified using the proposed FE-VFM, in Chapters 4 and 5. In Chapter 4, new types of virtual fields that are defined using real nodal displacements, namely the pseudo-real deformation field (PDF), are proposed to enhance the quality of the VFM for plastic constitutive parameters. Also, FE-VFM with the PDF is applied to characterize the homogeneous strain hardening of the advanced high-strength steel sheets. In Chapter 5, non-homogeneous strain hardening of the friction stir welded (FSWed) aluminum alloy sheets are identified using FE-VFM. In this chapter, feasibility tests based on the data generated by FE simulation are conducted priorly, and validated methods are applied for the real application.

2. Finite element-based virtual fields method

In Chapter 2, the formulations and calculation procedure of the FE-VFM are introduced. In Section 2.1, a general overview of the virtual fields method is provided. Then, the concept and procedure of the FE-VFM calculation are introduced in Section 2.2. In Sections 2.3 to 2.5, detailed formulations of the FE-VFM are introduced. Reconstruction of the displacements into the FE meshes is introduced in Section 2.3, and calculations of the kinematic variables such as deformation gradient and strains are shown in Section 2.4. Finally, integration of the internal virtual works (IVW) using Gauss quadrature during the parameter optimization is introduced in Section 2.5.

2.1. The virtual fields method: an overview

The virtual fields method (VFM) is a hybrid experimental–numerical approach for the inverse identification of constitutive parameters [31,32]. It is based on the PVW. Eq. (2.1) represents the PVW under the plane stress condition in a deformed configuration (or Lagrangian formulation).

$$t\int_S \sigma_{ij}\frac{\partial \delta u_i}{\partial x_j}ds = \int_{\partial S_f} f_k^s \delta u_k ds \tag{2.1}$$

where σ_{ij} is a Cauchy stress tensor, δu_i is the virtual displacement, x_j is the deformed coordinate, f_k^s is the surface traction vector acting on the force

boundaries, t is the thickness of an object, and S and ∂S_f denote an AOI and the force acting boundaries, respectively. Note that an index notation according to the Einstein convention will be used unless otherwise indicated. The term on the left-hand side of Eq. (2.1) is called the IVW exerted by internal stresses, while that on the right-hand side is the external virtual work (EVW) exerted by external forces. The integrand of IVW in Eq. (2.1) can be written as Eq. (2.2) by utilizing the symmetry of the Cauchy stress tensor, and the gradient of virtual displacement can be denoted as a strain-like variable, namely the virtual strain.

$$\sigma_{ij}\frac{\partial \delta u_i}{\partial x_j}=\sigma_{ji}\frac{\partial \delta u_i}{\partial x_j}=\sigma_{ij}\frac{1}{2}\left(\frac{\partial \delta u_i}{\partial x_j}+\frac{\partial \delta u_j}{\partial x_i}\right)=\sigma_{ij}\delta\varepsilon_{ij} \tag{2.2}$$

The PVW can also be expressed in an undeformed configuration or an Eulerian scheme as follows [67,84]:

$$t\int_{S_0} P_{ij}\frac{\partial \delta x_i}{\partial X_j}ds=\int_{\partial S_{0f}} f_{0k}^{s}\delta x_k ds \tag{2.3}$$

where P_{ij} is the first Piola–Kirchhoff (P–K) stress tensor, X_j is the undeformed coordinate, δx_i is the virtual position vector, f_{0k}^{s} is the traction vector in the initial configuration, and S_0 and ∂S_{0f} are the initial (reference) AOI and force acting boundaries, respectively. Note that Eqs. (2.1) and (2.3) are equivalent. However, the gradient of the virtual position cannot be

denoted as the virtual strain because the first P-K stress tensor is not symmetric. Instead, the gradient of virtual positions can be denoted as a virtual deformation gradient because of its similarity to a real deformation gradient.

$$\delta F_{ij} = \frac{\partial \delta x_i}{\partial X_j} \tag{2.4}$$

The relationship between the first P–K stress and the Cauchy stress is given as follows:

$$P_{ij} = J_{x-X} \left(F_{ki}\right)^{-1} \sigma_{kj} \tag{2.5}$$

where F_{ki} is a deformation gradient tensor and J_{x-X} is its determinant.

For linear elastic materials, Eq. (2.1) can be rewritten as follows:

$$t\int_S Q_{ijkl}\varepsilon_{kl}\delta\varepsilon_{ij}ds = \int_{\partial S_f} f_m^s \delta u_m ds \tag{2.6}$$

where Q_{ijkl} and ε_{kl} are the fourth-order elastic stiffness tensor and strain tensor, respectively. In VFM, the strain fields are measured a priori by the full-field measurement, whereas the material parameters of the constitutive law, or in this case, the components of the stiffness tensor, are to be solved. Note that the general displacement-based FEM solves the displacement fields with the given material parameters as inputs. Therefore, the VFM is based on the same governing equations as the FEM, but the solution process is reversed. Under this principle, Eq. (2.6) can be solved if the number of virtual fields

provided is the same as the number of independent (unknown) stiffness components [31,32,42].

The virtual fields are user-defined arbitrary fields that are admissible if they satisfy zero virtual displacements at the previously described displacement boundaries. One additional constraint of virtual fields for VFM is that the virtual fields should be constant at the prescribed external force boundaries [31,32]. This constraint is because only the resultant force can be measured in common experiments, and not the traction vector. If the virtual fields are constant at the force-acting boundaries, the EVW in Eq. (2.6) can be expressed as a product of the resultant forces and virtual displacements at the boundaries formulated in Eq. (2.7),

$$\int_{\partial S_f} f_k^s \delta u_k ds = \sum \left(F_k \delta u_k \right)_{\text{at boundary}} \tag{2.7}$$

where F_k is an external load vector measured during the experiment.

For materials with nonlinear constitutive laws, the PVW cannot be modeled as a linear system. Instead, a cost function is defined as the difference between the IVW and the EVW [31,46,47,49,81].

$$\Omega(k) = \left(t \int_S \sigma_{ij}\left(k, \varepsilon_{ij}\right) \delta\varepsilon_{ij} ds - \int_{\partial S_f} f_k^s \delta u_k ds \right)^2 \tag{2.8}$$

where the stress tensor σ_{ij} is a function of the strains ε_{ij} and material constant denoted by k. For some non-linear materials, such as elastic–plastic

materials, a proper stress update algorithm is required to obtain the stresses. The cost function in Eq. (8) is defined in a single time step. After calculating the values of the cost function over all the time steps, the unknown material parameter k can be obtained by minimizing the cost function with a numerical optimization such as a nonlinear least-squares method.

In many cases, the relation between Cauchy stress and kinematic values such as logarithmic strain is defined in the constitutive law. Hence, Eq. (2.1) is simple and intuitive for implementing the VFM. Also, for the small strain problem like a linear elasticity case, virtual displacmeents can be assigned as constant values easily. However, in the case of large deformations, the constant virtual displacements are not easily assigned at the force boundaries owing to the deformation of the boundaries of the AOI. In this case, Eq. (2.3) may be more efficient than Eq. (2.1) because the virtual positions can be defined as a function of the undeformed coordinates.

Meanwhile, in the conventional VFM, the IVW is calculated using a primitive discretized sum [31,32,44,46,61–63,65–67,84] as follows:

$$\delta W_{\text{int}} = t\sum_{n=1}^{ne}\left(\sigma_{ij}\delta\varepsilon_{ij}\right)_n A_n \tag{2.9}$$

where n is the index of data points, ne is the total number of data points, and A_n is the area of each data point.

2.2. Concept of the FE-VFM

In the FE-VFM, the displacement fields are mapped onto FE meshes using interpolation functions, and the Gauss quadrature is implemented for the calculation of IVW. Fig. 2-1 shows the schematic procedure of the FE-VFM at a single FE level. First, the global initial coordinates of the full-field data points are transformed to natural coordinates using shape functions. These shape functions are referred to as global coordinates; thus, they are termed "global shape functions." Then, the displacement fields are mapped onto the FEs of the natural coordinates with shape functions that apply to the natural coordinates or "natural shape functions." As a result, the (experimental) displacement fields were reconstructed as FE meshes, and the IVW was calculated using the Gauss quadrature rule. Although Fig. 2-1 illustrates only a 4-node linear quadrilateral element, the general formulations for other types of FEs are given in the following sections. Then, IVW was calculated using the Gauss quadrature rule with a given integration point.

Note that the use of the global shape functions is for mapping the natural coordinates of the full-field data points from the known global coordinates, for the numerical integration of the IVW using Gauss quadrature. In the conventional FEM, the isoparametric element is used. In that approach, both displacements and global coordinates are defined as a function of natural coordinates. However, in the full-field measurement, only the global (or real) coordinates are known for the measured data points. If the global coordinates

are mapped from the natural coordinates like the conventional FEM, it can be numerically inefficient since the natural coordinates of all the measured data points should be calculated by solving non-linear equations. For this reason, mapping of the coordinates is conducted in a reversed way compared to conventional FEM, instead of the isoparametric elements.

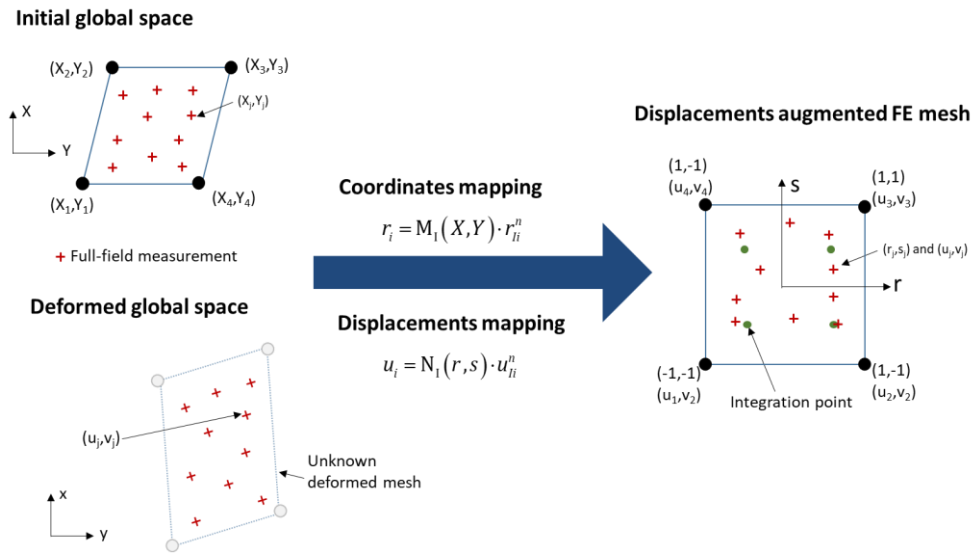

Fig. 2-1. Schematics of FE-VFM procedure in a single finite element

Fig. 2-2 shows a flow chart of the FE-VFM algorithm, which was implemented using MATLAB® in this study. The full-field displacements and FE meshes with the same geometries of the region of interest are prepared as the input data. The FE-VFM consists of three major steps. In the first step, the deformation field is reconstructed as FE meshes. In this step, the global shape functions are calculated for each element. Even for the same FE type, the global shape functions (in fact, the coefficients of the global shape functions) are different for each element because the global shape function depends on the initial global coordinates. In addition, the data points from the full-field measurement are identified by which elements they belong to. This process is conducted via the MATLAB® built-in closest simplex search function, *tsearchn*. Then, the (unknown) nodal displacements can be calculated using the local and global shape functions. As a result, displacement field-augmented FE meshes are constructed, and further calculations are made on the FE meshes without the original full-field data. More detailed formulations are given in Section 2.3.

Before parameter optimization, kinematic variables such as the deformation gradient and strain tensor at the integration points are calculated in a pre-processing step. In this step, a user selects the order of the Gauss quadrature rule, and the corresponding natural coordinates of the integration points are given. Note that the global coordinates of the integration points are also necessary to obtain the kinematic variables at each integration point

owing to the global shape function. The global coordinates of the integration points can be readily obtained by solving the non-linear global shape functions. In this study, a multi-variant Newton–Raphson method is used to solve the equations. Then, the kinematic variables are calculated based on the shape functions and nodal displacements. Finally, the IVW is calculated using the Gauss quadrature, and the parameter optimization process is performed as the last step. More details about these processes are provided in Sections 2.4 and 2.5.

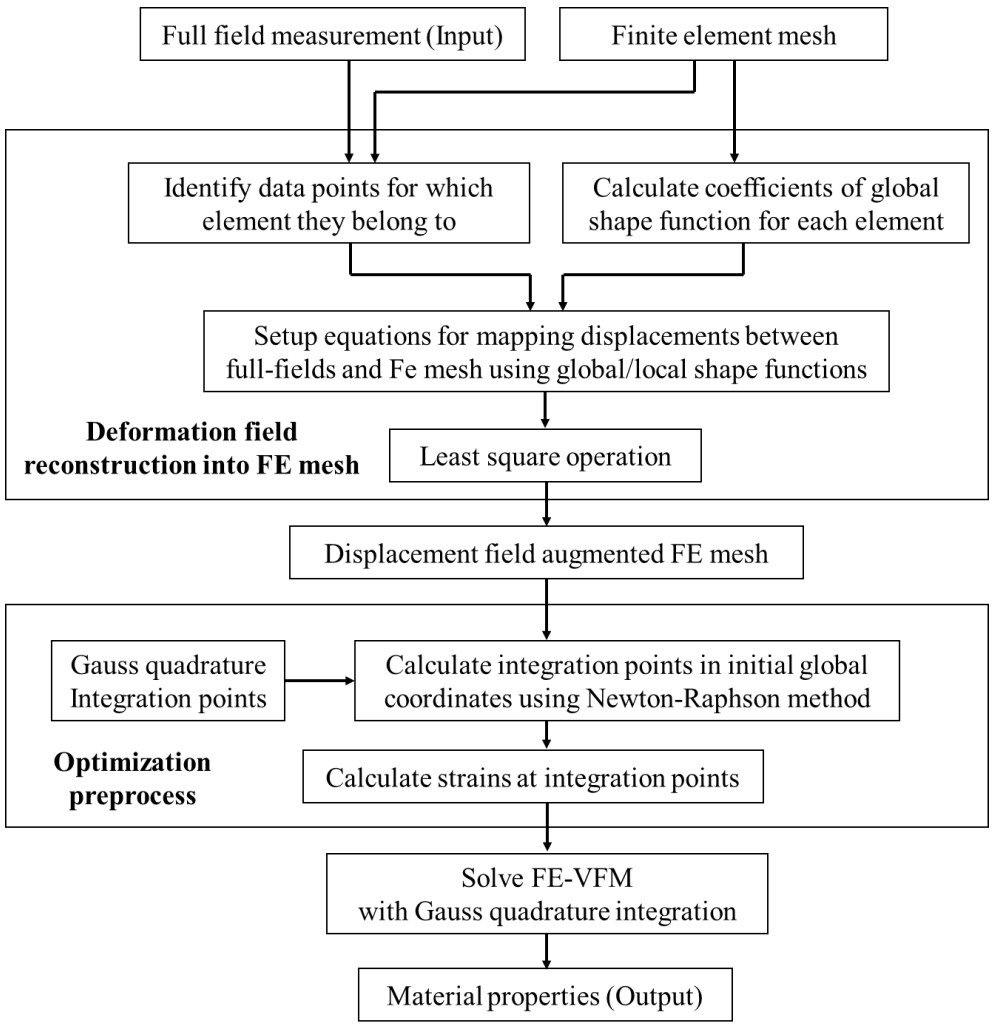

Fig. 2-2. Flow chart of FE-VFM process

2.3. Reconstruction of displacements on the finite element meshes

For a single element, the natural (or local) coordinates of a point can be interpolated as follows:

$$r_i\left(X_1, X_2\right) = \mathrm{M}_{\mathrm{I}}\left(X_1, X_2\right) \cdot r_{Ii}^n \tag{2.10}$$

where r_i represents the natural coordinates of a point in the element, r_{Ii}^n represents the natural nodal coordinates, and $\mathrm{M}_{\mathrm{I}}\left(X_1, X_2\right)$ are global shape functions referenced to the global coordinates. The notions of subscripts and superscripts in the equations are listed in Table 2-1, which are used hereafter unless otherwise noted.

Table 2-1. The notion of subscripts and superscripts used in the manuscript

Subscripts	
Latin lowercase letter	Vector and tensor indices, 1 and 2
Latin uppercase letter	Nodal index
Greek letters α and β	Full-field measurement point index
Greek letters λ and μ	Index for basis of shape function
Superscripts	
n	Nodal values
d	Full-field measurement point values
e	Local element values
g	Global FE mesh values

The global shape function $\mathrm{M}_{\mathrm{I}}\left(X_1, X_2\right)$ can be expressed by the product of the basis functions and their coefficients.

$$\mathrm{M}_{\mathrm{I}}\left(X_1, X_2\right)=\left(\mathrm{g}_\mu\right)^T \cdot a_{\mu I} \tag{2.11}$$

where g_μ is the vector for the basis function, and $a_{\mu I}$ is the coefficient of the global shape function. For example, the global shape function of a 4-node linear quadrilateral element can be written in matrix form as follows:

$$M_I=\begin{pmatrix}1 & X_1 & X_1 & X_1X_2\end{pmatrix}\begin{pmatrix}a_{11} & a_{12} & a_{13} & a_{14}\\ a_{21} & a_{22} & a_{23} & a_{24}\\ a_{31} & a_{32} & a_{33} & a_{34}\\ a_{41} & a_{42} & a_{43} & a_{44}\end{pmatrix} \tag{2.12}$$

The coefficients of the global shape functions can be determined using the zero-one property of the shape function[89]. That is, the value of each shape function becomes unity at the corresponding node, and zero at other nodes. From this, $a_{\mu I}$ can be obtained as an inverse of the basis function matrix, $G_{I\mu}^n$, constructed with nodal undeformed coordinates, as the product of $a_{\mu I}$ and $G_{I\mu}^n$ is the identity matrix.

$$a_{\mu I}=\left[G_{I\mu}^n\right]^{-1} \tag{2.13}$$

Then, the local coordinates of the full-field measurement points $r_{\alpha i}^d$ are calculated using the global shape functions as follows:

$$r_{\alpha i}^{d} = G_{\alpha\mu}^{d} \cdot a_{\mu I} \cdot r_{Ii}^{n} \tag{2.14}$$

where G_{kj}^{d} is the matrix of the global basis function calculated with the global coordinates of the full-field measurement points, and r_{Ii}^{n} represents the local nodal coordinates of the element.

Similar to the interpolation of local coordinates, the displacements are interpolated by local shape functions as follows:

$$u_i\left(r_1, r_2\right) = \mathrm{N}_{\mathrm{I}}\left(r_1, r_2\right) \cdot u_{Ii}^{n} \tag{2.15}$$

where $\left(r_1, r_2\right)$ are the local coordinates, and u_{Ii}^{n} represents the nodal displacements of the FE. The local shape functions $\mathrm{N}_{\mathrm{I}}\left(r_1, r_2\right)$ are denoted with the following matrix form:

$$\mathrm{N}_{\mathrm{I}}\left(r_1, r_2\right) = \left(\mathrm{h}_{\mu}\right)^{T} \cdot b_{\mu I} \tag{2.16}$$

where h_{μ} is the vector of the local basis functions similar to g_{μ} in Eq. (2.11), and $b_{\mu I}$ is the coefficient of the local shape function.

In general, global and local shape functions are not necessarily the same. However, in this study, identical types of interpolation functions were used. In addition, the coefficients of the global shape function $a_{\mu I}$ vary for each element, but those of the local shape functions $b_{\mu I}$ are constant. More details on the FEs and their shape functions are provided in **Appendix A**.

The relationship between displacements of the nodes and the data points (inside an element) can be established as follows:

$$u_{\alpha i}^{d} = H_{\alpha\mu}^{d} \cdot b_{\mu I} \cdot u_{Ii}^{n} = N_{\alpha I}^{e} \cdot u_{Ii}^{n} \tag{2.17}$$

where $H_{\alpha\mu}^{d}$ is the matrix of the local basis functions that are constructed with the local coordinates of the data points, as in Eq. (2.14). $N_{\alpha I}^{e}$ is the matrix of the local shape function values for an element. For all the FE meshes, the $N_{\alpha I}^{e}$ of each element should be assembled as its global matrix.

$$N_{\beta(\alpha)P(I)}^{g} = N_{\alpha I}^{e} \tag{2.18}$$

where $N_{\beta P}^{g}$ is the matrix of the shape function values for global FE meshes. Here, the local index of the data point α is associated with the global index of the corresponding data point β, and the local nodal index *I* corresponds to the global nodal index *P* through the connectivity arrays. With the known connectivity[1], the matrix for the global shape functions can be assembled.

Finally, the nodal displacements of an FE mesh are obtained using linear least-squares optimization:

[1] The global-local connectivity should be stored as a pre-processing procedure, as illustrated in Fig. 2-2.

$$u_{Pi}^{n} = \left(\left(N_{\alpha Q}^{g} \right)^{T} \cdot N_{\alpha P}^{g} \right)^{-1} \cdot \left(N_{\beta Q}^{g} \right)^{T} \cdot u_{\beta i}^{d} = A_{P\beta} \cdot u_{\beta i}^{d} \tag{2.19}$$

where $A_{P\beta}$ is the least-squares operator. For multiple time steps, the same $A_{P\beta}$ can be applied to every time step because the displacement mapping is conducted using the (fixed) initial global coordinates and (element) natural coordinates. In **Appendix B**, the reconstruction of the displacement fields for the linear quadrilateral element is given as an example.

2.4. Calculation of kinematic variables at the integration points

The deformation gradient, F_{ij}, is defined as follows:

$$F_{ij} = \frac{\partial x_i}{\partial X_j} = \frac{\partial}{\partial X_j}\left(X_i + u_i \right) = \frac{\partial u_i}{\partial X_j} + \delta_{ij} \tag{2.20}$$

where X_i and x_i are the undeformed and deformed coordinates, respectively, u_i is a displacement vector, and δ_{ij} is the Kronecker delta. Considering that the displacements are interpolated with the local shape functions, Eq. (2.20) can be rewritten as follows:

$$F_{ij} = \left(\left(\frac{\partial N_I}{\partial r_k} \frac{\partial r_k}{\partial X_j} \right)^{T} u_{Ii} \right)^{T} + \delta_{ij} \tag{2.21}$$

Moreover, the gradient of the local coordinates is given as:

$$\frac{\partial r_i}{\partial X_j} = \frac{\partial}{\partial X_j}\left(M_I r_{Ii}\right) = \left(\left(\frac{\partial M_I}{\partial X_j}\right)^T r_{Ii}\right)^T . \tag{2.22}$$

From Eqs. (2.21) and (2.22), Eq. (2.20) becomes

$$F_{ij} = \left(\left(\frac{\partial N_I}{\partial r_k}\right)^T u_{Ii}\right)^T \left(\left(\frac{\partial M_J}{\partial X_j}\right)^T r_{Jk}\right)^T + \delta_{ij} . \tag{2.23}$$

The derivatives of the local and global shape functions are calculated from Eqs. (2.11) and (2.16):

$$\left(\frac{\partial M_J}{\partial X_j}\right)^T = \left(\frac{\partial g_\mu}{\partial X_j}\right)^T a_{\mu J} \tag{2.24}$$

$$\left(\frac{\partial N_I}{\partial r_k}\right)^T = \left(\frac{\partial h_\mu}{\partial r_k}\right)^T b_{\mu I} \tag{2.25}$$

From Eqs. (2.23)–(2.25), the deformation gradient can be written as follows:

$$F_{ij} = \left(\left(\frac{\partial h_\mu}{\partial r_k}\right)^T b_{\mu I} u_{Ii}\right)^T \left(\left(\frac{\partial g_\lambda}{\partial X_j}\right)^T a_{\lambda J} r_{Jk}\right)^T + \delta_{ij} \tag{2.26}$$

The undeformed coordinates of the integration points are obtained using the global shape functions with Newton–Raphson(N–R) method. The target nonlinear equation $L_i\left(X,Y\right)$ for obtaining the undeformed coordinates of the integration points is given as follows:

$$L_i\left(X_1, X_2\right) = M_I\left(X_1, X_2\right) \cdot r_{Ii} - r_i = 0 \tag{2.27}$$

where r_i is the natural coordinate of an integration point. The linearization of Eq. (2.27) results in the following equation:

$$X_i^{n+1} = X_i^n - \left(\frac{\partial L_k}{\partial X_i}\right)^{-1} L_k^n = X_i^n - \left(\left(\frac{\partial g_\mu}{\partial X_k}\right)^T a_{\mu J} r_{Ji}\right)^{-1} L_k^n \tag{2.28}$$

where superscript n is the iteration number. The initial guess for the Eq. (28) is assumed to be the center of an element,

$$X_i^0 = \frac{1}{e}\sum_{I=1}^{e} X_{Ii} \ . \tag{2.29}$$

With the solution from Eq. (28), the derivatives of the global shape functions and deformation gradients at the integration points can be obtained.

Meanwhile, Constitutive laws are often given as relations between Cauchy stress tensor and logarithmic (or Hencky) strain tensor for elastic-plastic materials. Below, the logarithmic strains and related tensor values are introduced based on continuum mechanics. Note that rotation of materials is already taken cared since all calculation process is performed in Eulerian scheme. Here, superscripts g, d, p, and m denote undeformed global, deformed global, principal, and material coordinates, respectively. Values without superscript denote tensor values in global coordinates.

Right Cauchy-Green tensor

$$C_{ij} = \left(F_{ki}\right)^T F_{kj} = U_{ij}^2 \tag{2.30}$$

Stretch tensor

$$U_{ij}^g = \left(V_{ki}\right)^T \sqrt{C_{kl}^p} V_{lj} \tag{2.31}$$

Polar decomposition and material rotation tensor

$$R_{ij} = F_{ik}\left(U_{jk}\right)^{-1} \tag{2.32}$$

Logarithmic strain in the initial configuration

$$E_{ij}^g = \left(V_{ki}\right)^T \ln\left(U_{kl}^p\right) V_{lj} \tag{2.33}$$

Here, V_{ij} is a rotation tensor from global to principal coordinates, which are composed of eigenvectors of a given tensor. Also, a component of tensor in principal coordinates has eigenvalues as its diagonal components, and all off-diagonal components are zero. The rotation tensor V_{ij} and corresponding tensors in principal coordinates can be obtained from the calculation of eigenvalue and eigenvector.

Suppose the angle difference between undeformed global and material coordinates is θ. Rotation tensor ϖ_{ij} from undeformed global to material coordinates in 2D is as follows.

$$\varpi_{ij} = \begin{bmatrix} \cos\theta & -\sin\theta \\ \sin\theta & \cos\theta \end{bmatrix} \tag{2.34}$$

Then, logarithmic strain tensor in material and deformed global coordinates are as follows.

Logarithmic strain in material coordinates

$$E_{ij}^{m} = \left(\varpi_{ki}\right)^{T} E_{kl}^{g} \varpi_{lj} \tag{2.35}$$

Logarithmic strain in the deformed coordinates

$$E_{ij}^{d} = R_{ik} E_{kl}^{g} \left(R_{jl}\right)^{T} \tag{2.36}$$

2.5. Integration of the internal virtual work

In the FE-VFM, the Gauss quadrature is used for integrating the virtual work. The integration of the IVW is performed on the natural coordinates of each element. In the updated Lagrangian approach, the IVW of an element can be written as follows:

$$\delta W_{\text{int}}^{e} = t \int_{\Omega} \sigma_{ij} \delta\varepsilon_{ij} J_{x-X} J_{X-r} drds \tag{2.37}$$

where the superscript "e" denotes an element value, Ω represents the domain of an element, J_{x-X} and J_{X-r} are Jacobian determinants, which are defined as follows:

$$J_{x-X} = \det\left(\frac{\partial x_i}{\partial X_j}\right) = \det\left(F_{ij}\right) \tag{2.38}$$

$$J_{X-r} = \det\left(\frac{\partial X_i}{\partial r_j}\right) = \frac{1}{\det\left\{\left(\left(r_{il}\right)^T \frac{\partial M_I}{\partial X_j}\right)\right\}} \tag{2.39}$$

The IVW in the Eulerian configuration is written as follows:

$$\delta W_{\text{int}}^e = t\int_\Omega P_{ij}\delta F_{ij} J_{X-r} drds \tag{2.40}$$

In this study, the Eulerian approach is used. For a linear elastic material, Eq. (2.40) can be expressed as

$$\delta W_{\text{int}}^e = t\int_\Omega Q_{ikpq} E_{pq} \left(F_{jk}\right)^{-T} \delta F_{ij} J_{X-r} J_{x-X} drds \ . \tag{2.41}$$

For plastic materials, Eq. (2.40) can be rewritten under the plane stress assumption and for plastic incompressibility conditions, as follows:

$$\delta W_{\text{int}}^e = t_0\int_\Omega \exp\left(\varepsilon_t\right)\sigma_{ik} \left(F_{jk}\right)^{-T} \delta F_{ij} J_{X-r} J_{x-X} drds \tag{2.42}$$

where t_0 is the initial sheet thickness, and ε_t is the thickness strain, which is obtained as follows:

$$\varepsilon_t = \varepsilon_t^e + \varepsilon_t^p = -\frac{E}{\nu}\left(\sigma_{11} + \sigma_{22}\right) - \left(\varepsilon_{11}^p + \varepsilon_{22}^p\right) \tag{2.43}$$

Here, the superscripts “e” and “p” denote elastic and plastic components, respectively, and E and ν are Young’s modulus and Poisson’s ratio, respectively.

The IVW of the triangular elements integrated using the Gauss quadrature

is given as follows.

$$\delta W_{\text{int}}^{e} = \int_{\Omega} \omega(r,s)\,ds\,dr = \sum_{i=1}^{n} w_i \omega(r_i, s_i) \tag{2.44}$$

where $\omega(r,s)$ denotes the integrands in either Eq. (2.41) or (2.42), w_i is the weight of the Gauss quadrature, (r_i, s_i) are the natural coordinates of the integration point i, and n is the number of integration points. Note that (r,s) is equal to (r_1, r_2).

For a quadrilateral element, the IWV with Gauss quadrature can be written as follows:

$$\delta W_{\text{int}}^{e} = \int_{\Omega} \omega(r,s)\,ds\,dr = \sum_{i=1}^{n}\sum_{j=1}^{n} w_i w_j \omega(r_i, s_j) \tag{2.45}$$

The weights and natural coordinates of the integration points are listed in Tables 2-2 and 2-3.

Table 2-2. Gauss quadrature of a triangular element [90,91]

I [1]	N [2]	Natural coordinates	Weights
1	1	(a1, a1, a1) a1 = 0.3333333333333	0.5000000000000
2	3	(b1,b2,b2), (b2,b1,b2), (b2,b2,b1) b1 = 0.6666666666667, b2 = 0.1666666666667	0.1666666666667
3	4	(a1, a1, a1) a1 = 0.3333333333333	-0.2812500000000
		(b1,b2,b2), (b2,b1,b2), (b2,b2,b1) b1 = 0.6000000000000, b2 = 0.2000000000000	0.2604166666667
5	7	(a1, a1, a1) a1 = 0.3333333333333	0.1125000000000
		(a2,a1,a1), (a1,a2,a1), (a1,a1,a2) a1=0.4701420641051, a2=0.0597158717898	0.06619707639427
		(b2,b1,b1), (b1,b2,b1), (b1,b1,b2) b1=0.1012865073235, b2=0.7974269853531	0.0629695902724
7	13	(b2,b1,b1), (b1,b2,b1), (b1,b1,b2) b1=0.1012865073235, b2=0.7974269853531	0.0629695902724
		(b1,b2,b3), (b2,b1,b3), (b1,b3,b2), (b3,b1,b2), (b2,b3,b1), (b3,b2,b1) b1=0.3128654960049, b2=0.0486903154253, b3=0.6384441885698	0.0385568804451
		(c2,c1,c1), (c1,c2,c1), (c1,c1,c2) c1=0.2603459660790, c2=0.4793080678419	0.0878076287166
		(a1, a1, a1) a1 = 0.3333333333333	-0.0747850222339

[1] integration order, [2] number of integration points

Table 2-3. Gauss quadrature of a quadrilateral element [90,91]

I [1]	N [2]	Natural coordinates	Weights
1	1	0.0000000000000	2.0000000000000
3	2x2	±0.5773502691896	1.0000000000000
5	3x3	0.0000000000000	0.8888888888889
		±0.7745966692415	0.5555555555556
7	4x4	±0.3399810435849	0.6521451548625
		±0.8611363115941	0.3478548451375

[1] integration order, [2] number of integration points

3. Numerical sensitivity tests based on simulation data

In this chapter, numerical sensitivity tests of the FE-VFM proposed in the previous chapter are shown. In the sensitivity tests, deformation data generated by the finite element simulation was used as an input of the FE-VFM, to avoid the effect of the experimental errors, and for the investigation of the pure numerical effect of the FE-VFM conditions including FE order and size, and Gauss quadrature order. The tests were conducted for both orthotropic linear elastic and elastic-plastic cases, and the effect of the FE-VFM conditions are numerically analyzed by obtaining the residuals of the virtual works. The sensitivity test conditions are given in Section 3.1, and the sensitivity test results for the linear elastic and elastic-plastic cases are shown in Section 3.2 and 3.3, respectively. Exhaustive sensitivity tests demonstrated that the FE-VFM with higher and coarse finite elements accompanied with a higher order Gauss quadrature could provide promising results for the identification of the plastic hardening law parameters.

3.1. Sensitivity tests and FE simulation conditions

The validations of the FE-VFM are performed through the sensitivity study. In the sensitivity study, both the orthotropic linear elasticity and isotropic plasticity are considered, and the ideal full-field displacement fields are (virtually) produced using FE simulations, which provide data without experimental noise. In addition, this analysis enables a quantitative evaluation of the VFM results based on known target material constants. A sensitivity study is conducted on the effect of FE type, FE mesh size, and order of the Gauss quadrature. For the quantitative analysis, the difference between the IVW and EVW calculated from the input material parameters was examined. Ideally, IVW and EVW should be identical within a numerical tolerance.

Abaqus/Standard was used for the virtual experiments. For the orthotropic linear elastic material, a tensile test with a center hole specimen was performed. The geometry of the virtual specimen and the corresponding boundary conditions are illustrated in Fig. 3-1. The thickness of the specimen was defined as 2 mm. The model was discretized with 143,585 elements, and the element type was a 4-node plane stress quadrilateral element with reduced integration (CPS4R).

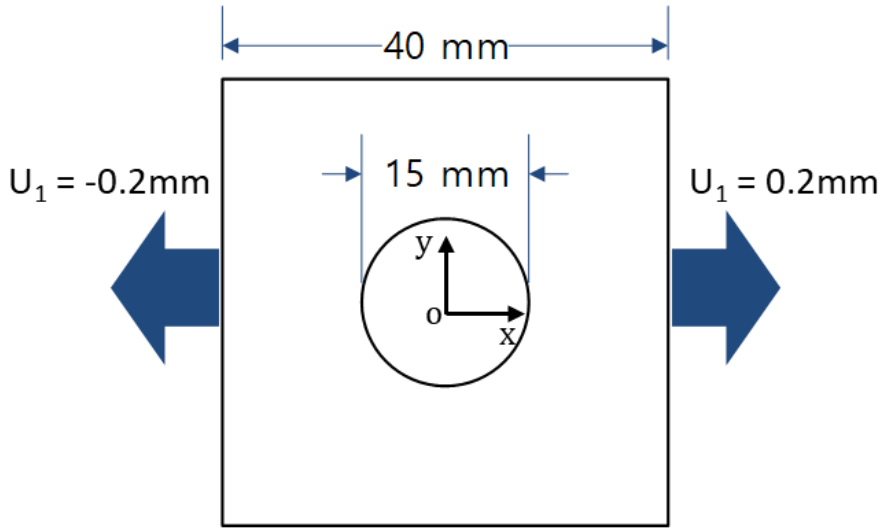

Fig. 3-1. Specimen geometry and boundary conditions for virtual FE simulations for (a) anisotropic linear elastic material and (b) elastic-plastic material.

The constitutive law for orthotropic linear elasticity is written as follows:

$$\begin{pmatrix} \sigma_1 \\ \sigma_2 \\ \sigma_6 \end{pmatrix} = \begin{pmatrix} Q_{11} & Q_{12} & 0 \\ Q_{12} & Q_{22} & 0 \\ 0 & 0 & Q_{66} \end{pmatrix} \begin{pmatrix} \varepsilon_1 \\ \varepsilon_2 \\ \varepsilon_6 \end{pmatrix} \tag{3.1}$$

where σ_i (i=1,2,6) and ε_i (i=1,2,6) are the components of the stress and strain tensor in Voigt notation, respectively, and Q_{ij} (i,j=1,2,6) is the orthotropic elastic stiffness. The constants used in the FE simulations are listed in Table 3-1.

Table 3-1. Orthotropic linear elastic constants used in the sensitivity study

Q_{11}	Q_{22}	Q_{12}	Q_{66}
41.0 GPa	10.3 GPa	3.1 GPa	4.0 GPa

For the elastic-plastic material, a notch tension test was conducted, as illustrated in Fig. 3-2. The virtual thickness of the specimen was defined as 2 mm. The number of elements was 31,309, and the same element type as in the elastic problem was used.

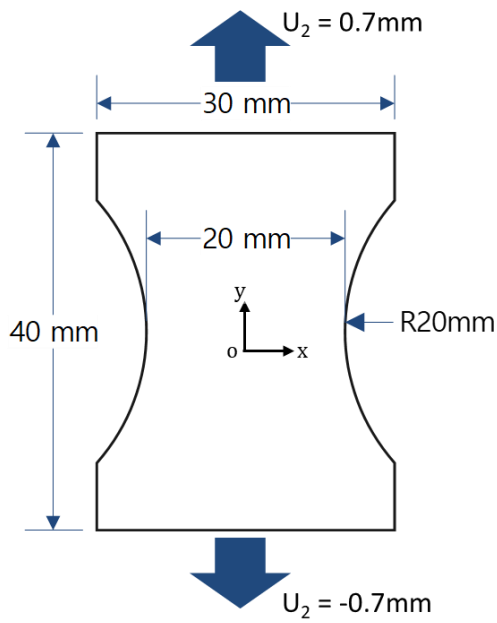

Fig. 3-2. Specimen geometry and boundary conditions for virtual FE simulations for elastic-plastic material.

For the elastic-plastic constitutive law, the material was assumed to be isotropic. The von Mises yield function and isotropic hardening using the

Swift hardening law in Eq. (3.2) were employed.

$$\bar{\sigma} = K\left(\bar{\varepsilon} + e_0\right)^n \tag{3.2}$$

where $\bar{\sigma}$ and $\bar{\varepsilon}$ are the equivalent stress and equivalent plastic strain, respectively, and K, e_0, and n are material constants. The material constants of the Swift law are listed in Table 3-2.

Table 3-2. Elastic-plastic material constants used in sensitivity tests

Elastic constants		Plastic strain-hardening law		
E(GPa)	ν	K (MPa)	e_0	n
70	0.33	350	0.045	0.15

In the FE simulation, the total displacement was incrementally applied over 100 time steps, and the simulation results over all the time steps were used for the sensitivity analysis. In this study, a tangent stiffness-based stress integration algorithm [92,93] was used.

The conditions for the sensitivity tests were: (1) element sizes of 1 mm to 5 mm; (2) element types of linear (T3[2]), quadratic (T6), and cubic (T10) triangular elements, and linear (Q4), quadratic (Q8), and cubic (Q12) quadrilateral elements; and (3) orders of the Gauss quadrature from 1 to 7.

[2] T and Q denote triangular and quadratic elements, respectively. Here, the numbers in the elements represent the number of nodes in each element.

Note that linear quadrilateral elements with the nodal coordinates shown in Fig. 3-3 had to be avoided because of the singularity in the calculation of global shape functions [89].

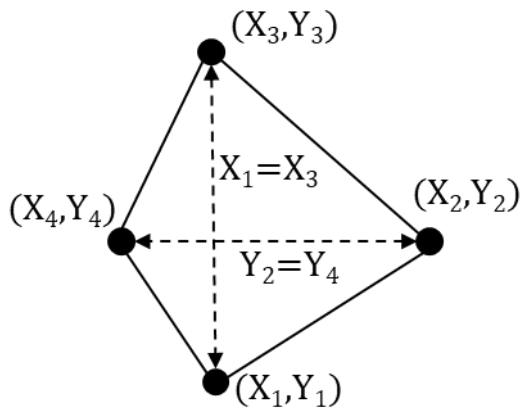

Fig. 3-3. Linear quadrilateral element should be avoided in the FE mesh

In this study, linear triangular and quadrilateral element meshes are generated by an Abaqus CAE pre-processor. higher-order element meshes are generated by modifying linear element meshes using in-house programming.

As schematically shown in Fig. 3-4, The meshing procedure from the linear to the higher-order elements is summarized as follows. First, new (trial) nodes are added between the existing nodes as initial guesses. For quadratic elements, the additional nodes are positioned at the center of the two connected nodes, while those for the cubic elements are added at 1/3 and 2/3 the distance between the two existing nodes. Additionally, a center node is added for cubic triangular elements.

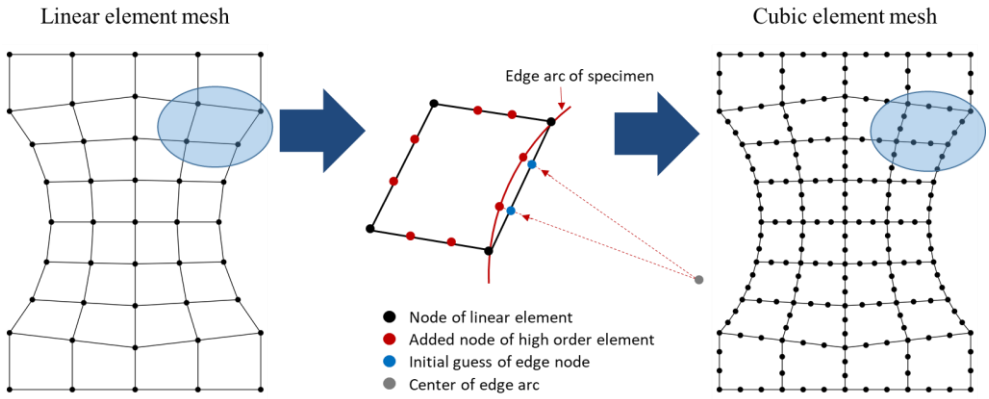

Fig. 3-4. Generation of higher order element meshes by modifying the linear elements

After that, the position of the nodes at the curved edges is corrected to the proper position. Curved edge nodes can be identified using the circle equation.

$$\left(X_n - X_0\right)^2 + \left(Y_n - Y_0\right) - r^2 < TOL \tag{3.3}$$

where $\left(X_n, Y_n\right)$ is the nodal position of the initial linear elements at the curved edge, $\left(X_0, Y_0\right)$ is the center of the curved edge arc, r and TOL is numerical tolerance. After the curved edge is identified, the correct added nodal position $\left(X_{cor}, Y_{cor}\right)$ can be calculated using arc center and radius, an initial guess of added node position $\left(X_{guess}, Y_{guess}\right)$.

$$\begin{cases} X_{cor} = \pm r\cos\theta + X_0 \\ Y_{cor} = \pm r\cos\theta + Y_0 \end{cases} \tag{3.4}$$

where angle θ is

$$\theta = \text{atan}\left(\frac{Y_0 - Y_{guess}}{X_0 - X_{guess}} \right). \tag{3.5}$$

Among possible 4 solutions in Eq. (3.4), most closet point to the initial guess is selected as a correct added nodal position for the higher-order elements on the curved edge.

Meanwhile, linear element meshes generated by Abaqus/CAE are shown in Figs. 3-5 and 3-6, for the linear elastic case and elastic-plastic case, respectively. Also, examples of higher order element meshes are shown in Figs. 3-7 and 3-8, for the linear elastic case and elastic-plastic case, respectively.

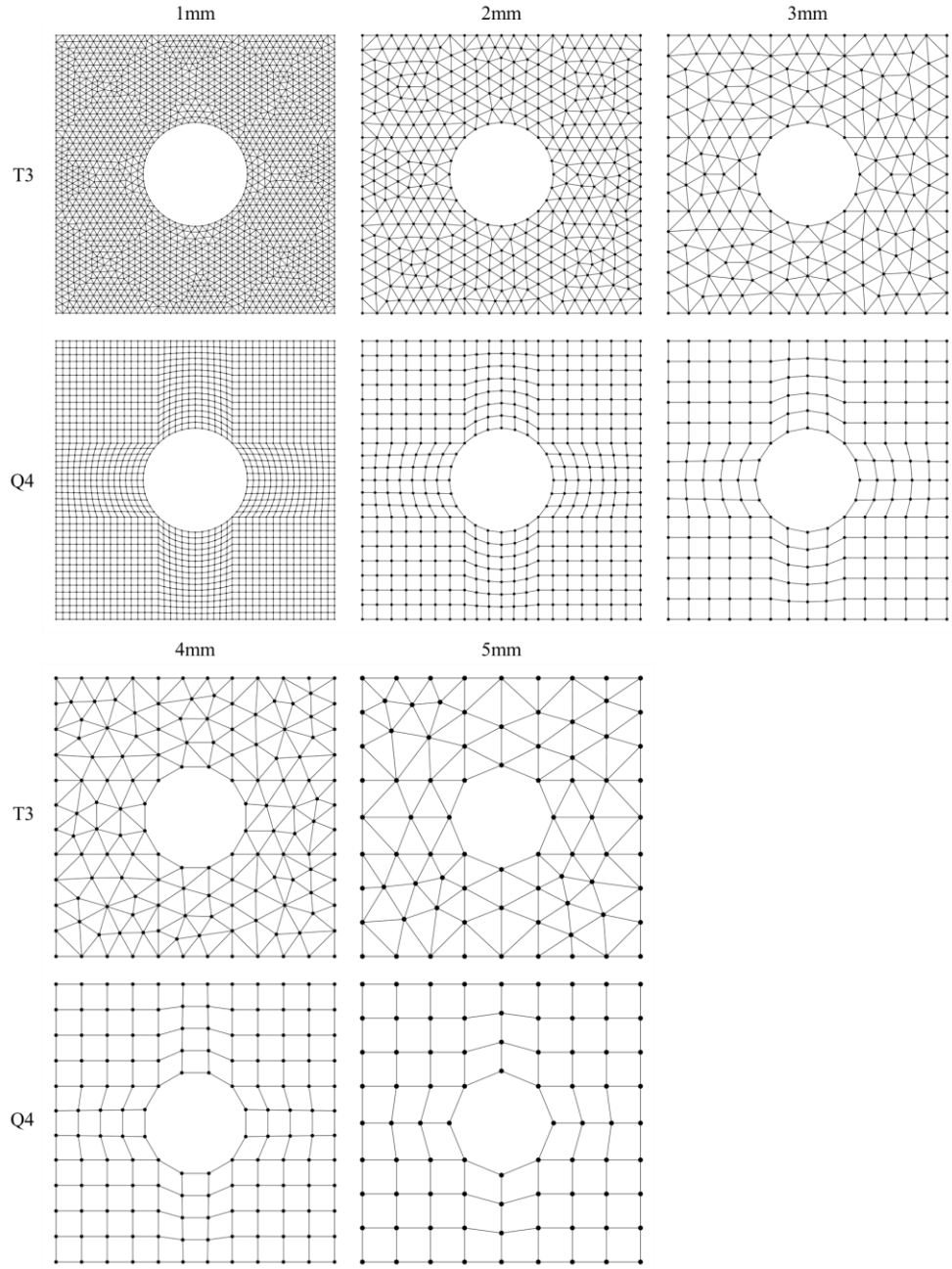

Fig. 3-5. Finite element meshes used for the sensitivity test of the orthotropic linear elastic problem. Meshes in the figure are linear element meshes generated by Abaqus/CAE with element sizes of 1mm to 5mm.

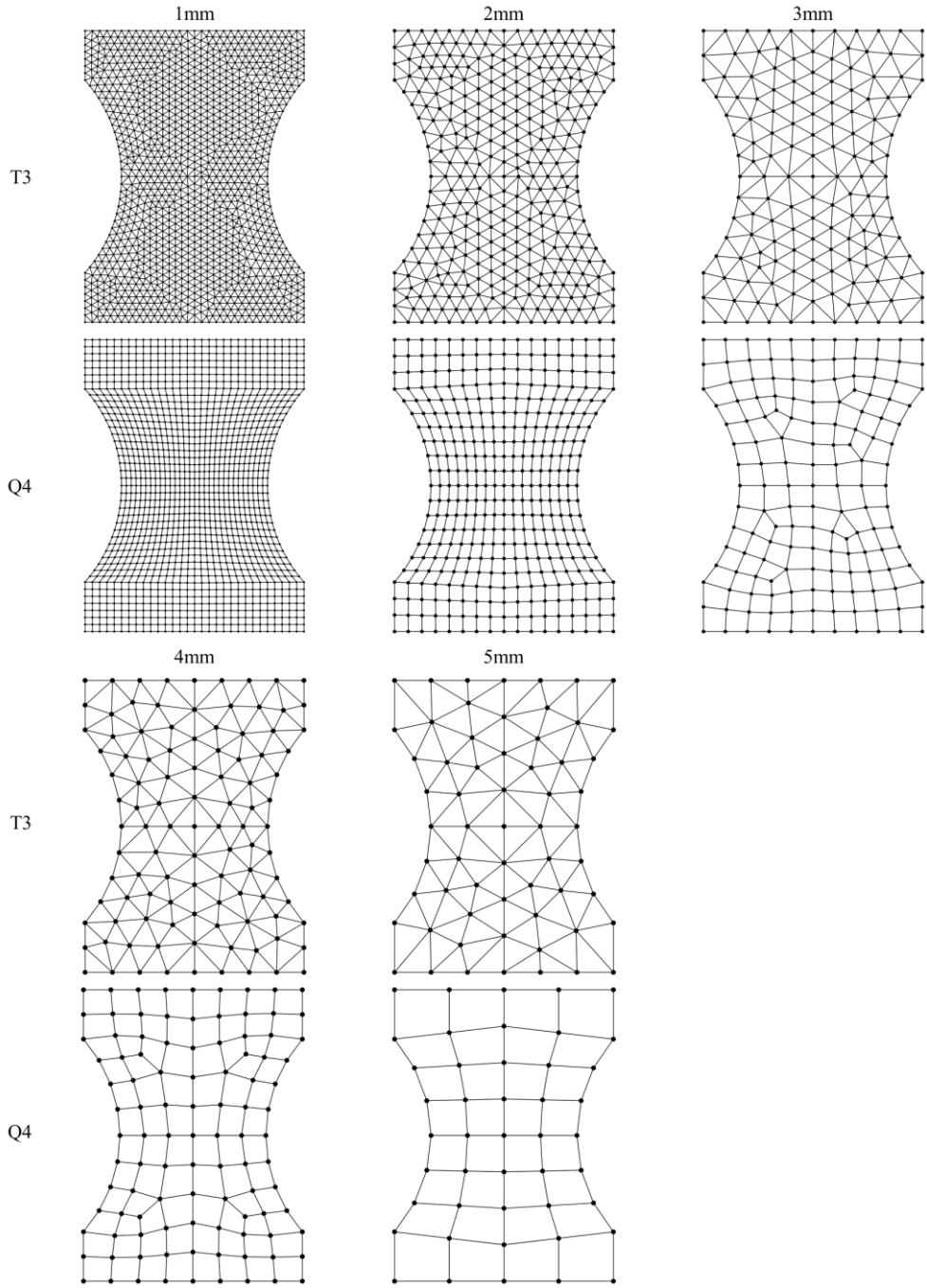

Fig. 3-6. Finite element meshes used for the sensitivity test of the plastic problem. Meshes in the figure are linear element meshes generated by Abaqus/CAE with element sizes of 1mm to 5mm.

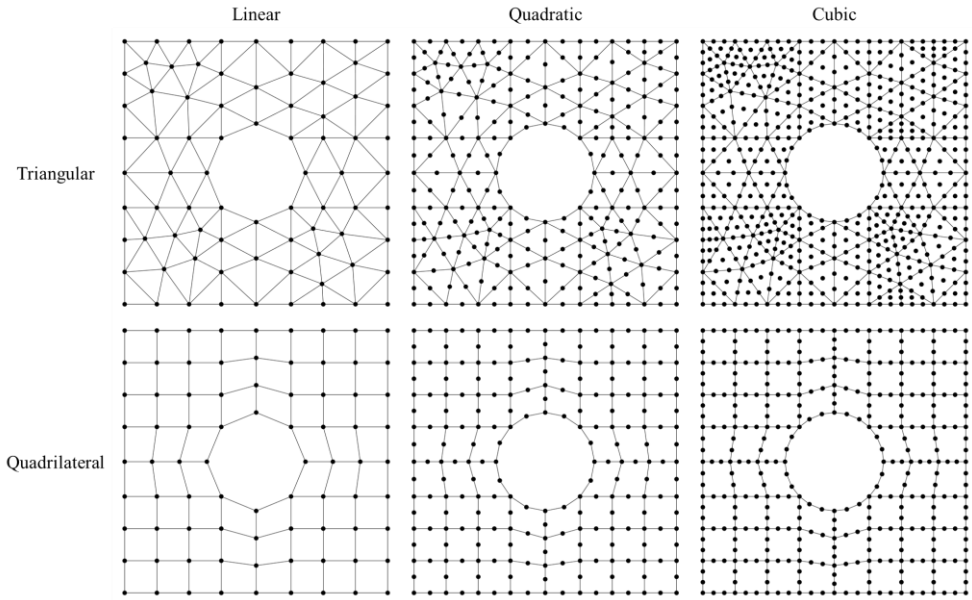

Fig. 3-7. Example of higher-order element meshes generated by in-house Matlab code for the orthotropic linear elastic problem

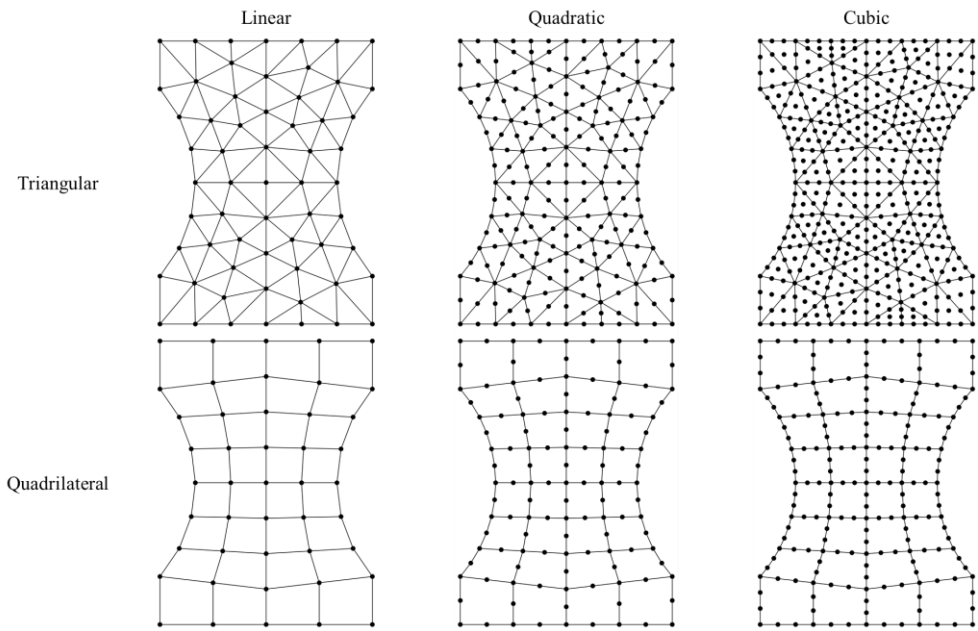

Fig. 3-8. Example of higher order element meshes generated by in-house Matlab code for the plastic problem.

3.1. Results: orthotropic linear elastic properties

In Fig. 3-9, the displacement (U_i) and logarithmic strain (E_{ij}) fields are presented for the orthotropic linear elastic material. Fig. 3-9(a) shows the results of the FE simulation, and Fig 3-9(b) shows the reconstructed results obtained using the proposed mapping algorithm. The element type shown in the figure and its average size are Q12 and 5 mm, respectively. As validated in the figures, the reconstructed fields are in good agreement with the FE-simulated fields, even with coarse meshes, when higher order elements are used.

Two different sets of polynomial virtual fields were used for the sensitivity tests of linear elasticity, which are shown below.

$$\begin{cases} \delta x_1 = \left(X_1 / 20\right) \\ \delta x_2 = 0 \end{cases} \tag{3.6}$$

$$\begin{cases} \delta x_1 = \left(X_1 / 20\right)^3 \\ \delta x_2 = \left(\left(X_1 / 20\right)^2 - 1\right)\left(X_2 / 20\right) \end{cases} \tag{3.7}$$

The above virtual fields are functions of the undeformed global coordinates normalized by a half-length of the virtual specimen. The virtual fields in Eq. (3.6) and (3.7) represent the linear and nonlinear polynomials, respectively.

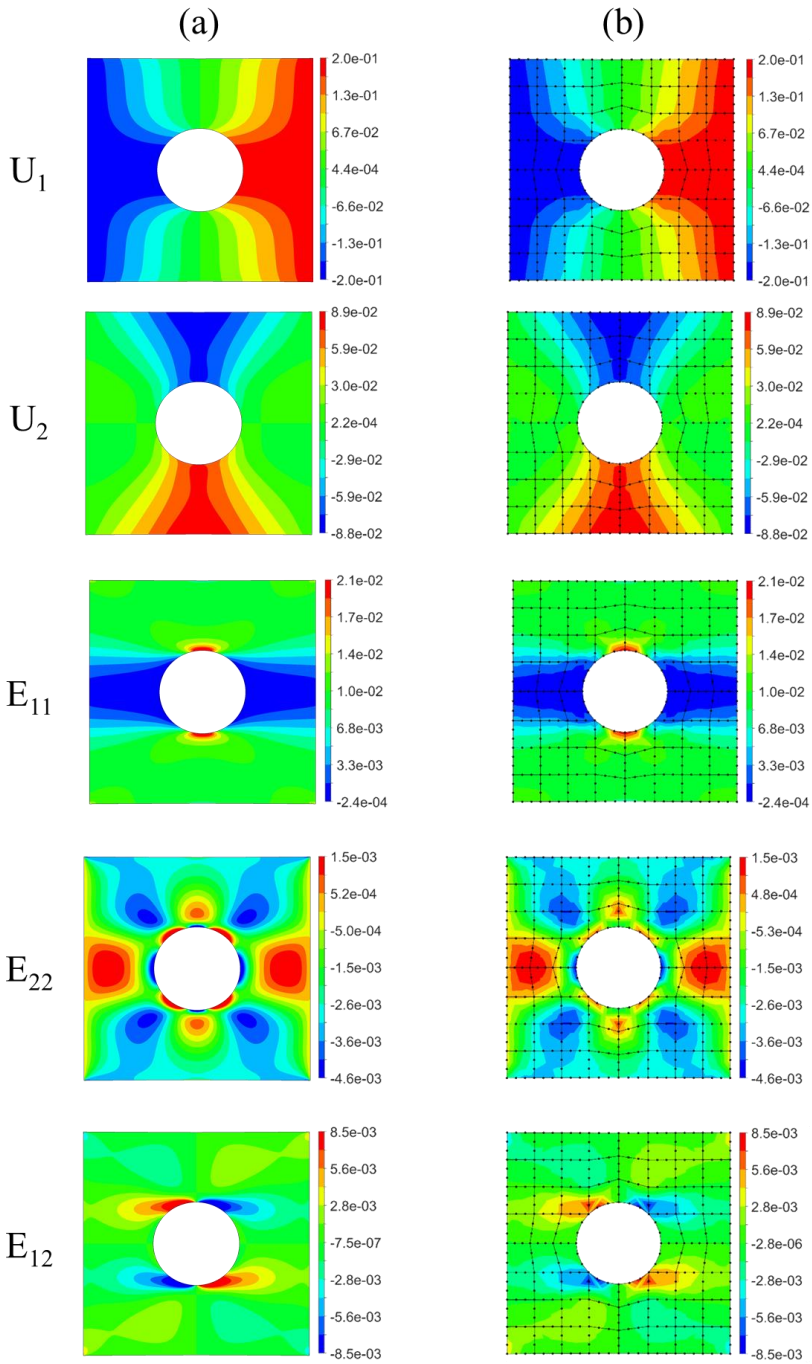

Fig. 3-9. Comparison of displacement and strain fields for the linear elastic material. (a) FE simulated deformation fields before mapping and (b) reconstructed fields with Q12 finite elements with an average size of 5 mm

For the given virtual fields, the accuracy of the FE-VFM results is estimated based on the difference between the IVW and EVW. The residual (R) was defined as follows:

$$\mathrm{R}_{\delta W}^{e}=\left|\frac{\delta W_{\mathrm{int}}-\delta W_{\mathrm{ext}}}{\delta W_{\mathrm{ext}}}\right|\times 100(\%) \tag{3.8}$$

Fig. 3-10 shows the sensitivity test results for linear polynomial virtual fields calculated by Eq. (3.6). As the element size increases, larger residuals are calculated for both linear elements in Fig. 3-10(a). For quadratic and cubic elements, a considerably low level of residuals is indicated for all investigated element sizes. Fig. 3-10(b) shows the effect of the order of integration on the accuracy. It is evident that the residuals for linear elements are not influenced significantly by the order of the Gauss quadrature. For the quadratic elements, the first-order integration resulted in the best accuracy. For the cubic elements, the residuals are lowered if the order of integration is higher than three. The results in Fig. 3-10 show that none of the residuals in any of the investigated cases are very large, even for rather coarse linear elements (only 3% at a maximum).

In Fig. 3-11, the sensitivity test results for more complex polynomial virtual fields calculated by Eq. (3.7) are presented. It is evident that smaller residuals are calculated with nonlinear polynomial virtual fields than with linear virtual fields by Eq. (3.6). In terms of the order of Gauss quadrature, all elements show very small residuals if the order is higher than three.

In summary, the effect of element type and size on the accuracy of FE-VFM was not noticeable, because small enough residuals were calculated even for linear elements and virtual fields. This low impact of FE parameters on the residual (or accuracy) may be because the spatial non-linearity of deformation is not significant for the case of linear elastic materials. In this case, the selection of virtual fields seems to be more critical than other factors, as shown by the differences in the residuals between the two virtual fields. Only a higher order of Gauss quadrature could improve the quality of IVW integration in cases when a nonlinear virtual field was used, as shown in Fig. 3-11(b).

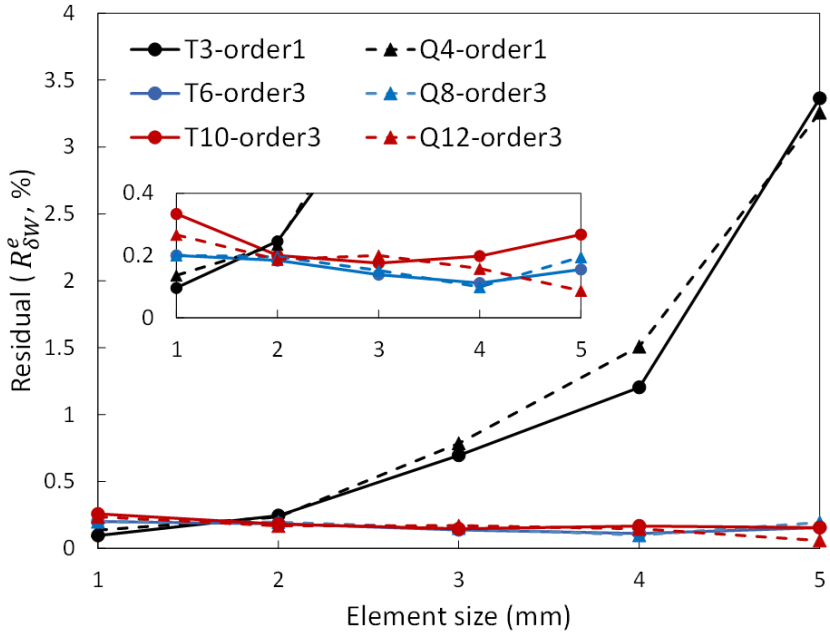

(a)

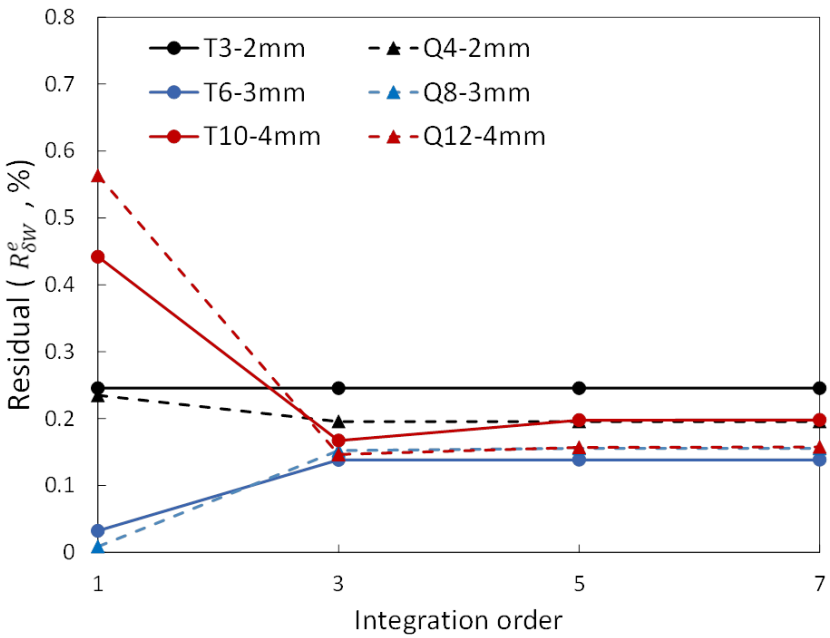

(b)

Fig. 3-10. Residuals of virtual work difference with linear virtual works for orthotropic linear elastic material with respect to (a) finite element size and (b) order of Gauss quadrature.

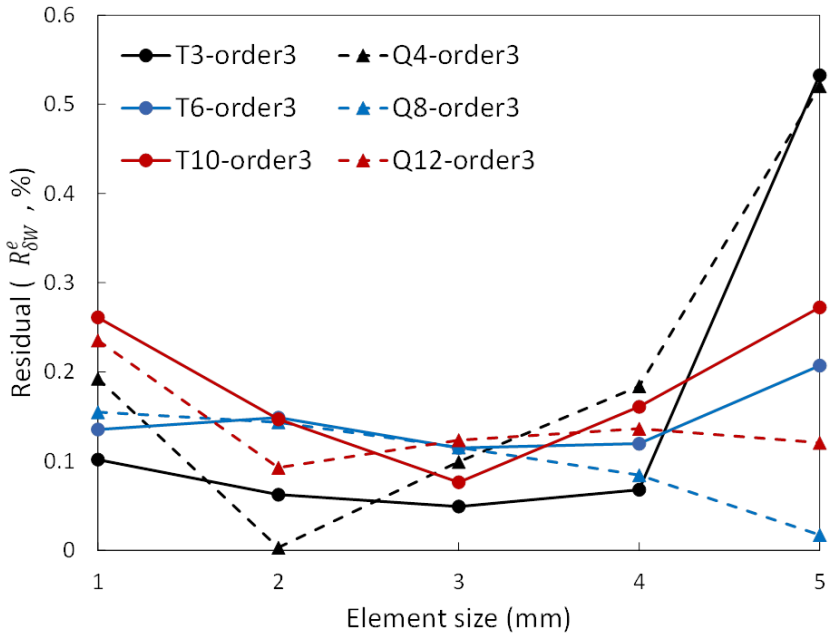

(a)

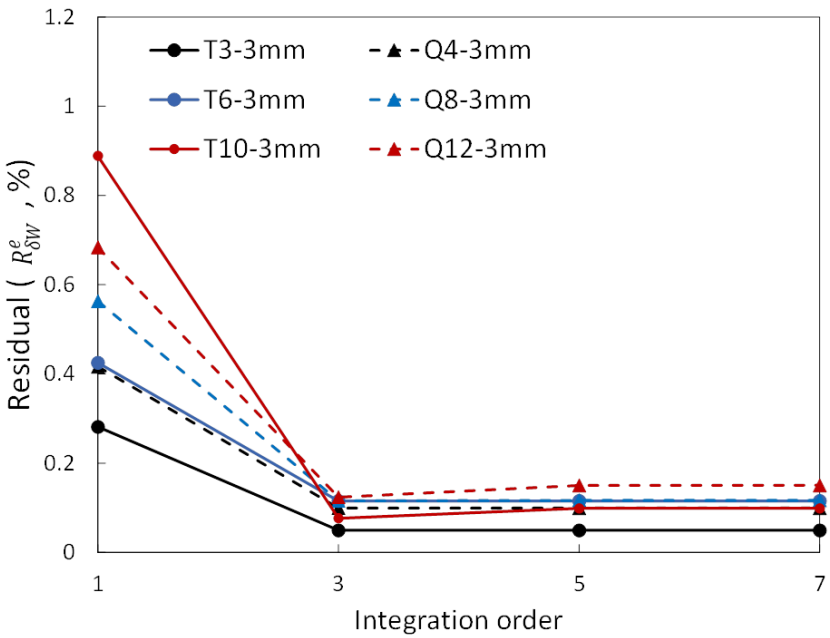

(b)

Fig. 3-11. Residuals of virtual work difference with non-linear virtual works for orthotropic linear elastic material with respect to (a) finite element size and (b) order of Gauss quadrature.

3.2. Results: plastic strain hardening law

In Fig. 3-12, the displacement and strain fields of the notched tension are presented for the elastic-plastic material. As in Fig. 3-10, Fig 3-12(a) and (b) show the FE-simulated and reconstructed deformation fields, respectively. The size and element type of the FE mesh are the same as in the elastic case. Again, the fields reconstructed by the proposed mapping algorithm show good agreement with the FE-calculated results, which validates the reliability of the FE-based mapping for large deformations.

In the sensitivity study, the following virtual fields are applied for the elastic-plastic material.

$$\begin{cases} \delta x_1 = \left(\left(X_2 / 20 \right)^2 - 1 \right) \left(X_1 / 15 \right) \\ \delta x_2 = \left(X_2 / 20 \right)^3 \end{cases} \tag{3.9}$$

As in the elastic case, the two virtual fields are considered undeformed coordinates normalized by half of the specimen width and height, respectively.

Similar to the elastic case, the residuals between the IVW and EVW are calculated with known target material constants. The residual for the error analysis is averaged over the time step and is defined as follows:

$$\mathrm{R}_{\delta W}^{p} = \frac{1}{n_{step}} \sum_{\tau=1}^{n_{step}} \left| \frac{\delta W_{\mathrm{int}} - \delta W_{\mathrm{ext}}}{\delta W_{\mathrm{ext}}} \right| \times 100(\%) \tag{3.10}$$

where τ is the time step number, and n_{step} (equal to 100 in this study) is the

total number of time steps.

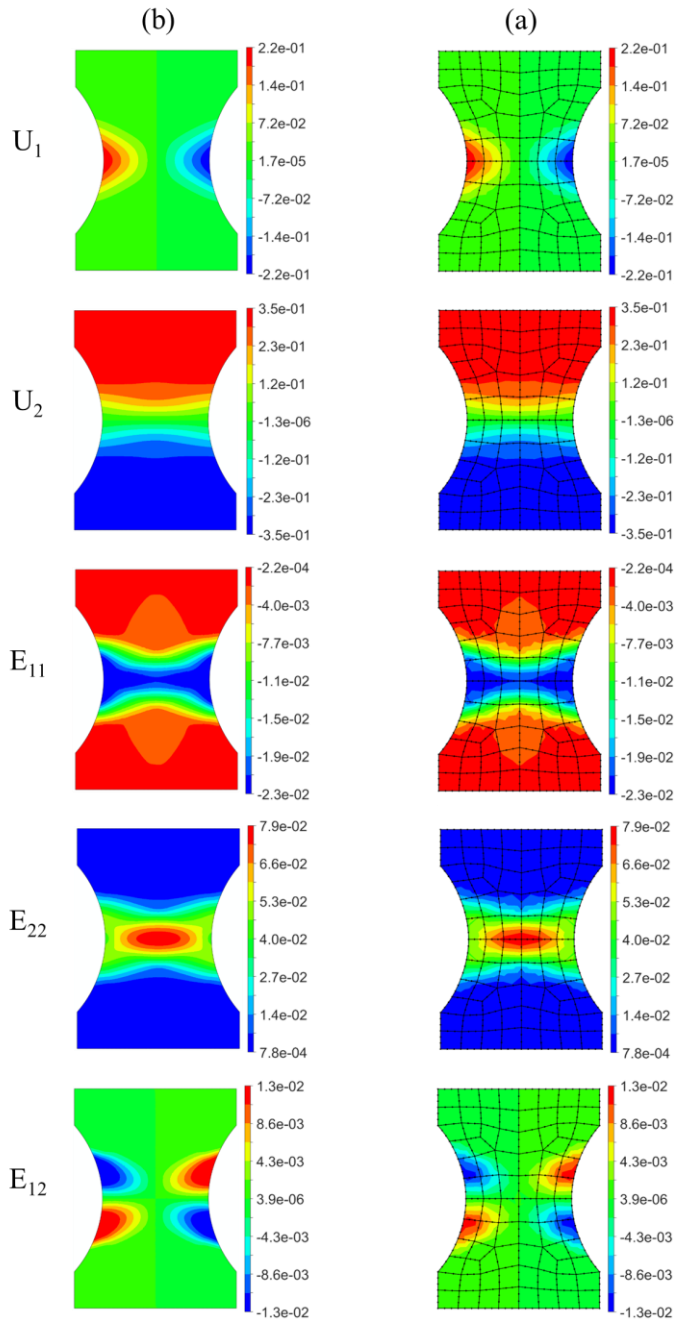

Fig. 3-12. Comparison of displacement and strain fields for isotropic elastic-plastic material. (a) FE simulated deformation fields before mapping and (b) Reconstructed fields with Q12 finite elements with an average size of 5 mm

In Fig. 3-13, the residuals of virtual work are presented with respect to the element size and order of the Gauss quadrature. As shown in Fig. 3-13(a), the residual is highly dependent on element size when a linear element is used. However, the residual is almost independent of the mesh size for higher-order elements. This is quite different from the elastic material, which showed negligible sensitivity to the element size. This indicates that finer meshes are necessary for the linear element under large plastic deformation. In other words, moderate or large element sizes can be employed for accurate mapping when higher-order elements are used.

In Fig.3-13(b), it is evident that the residuals of the virtual work are also significantly dependent on both element type and integration order. For the linear triangular element (T3), no noticeable change in the residual was observed with different integration orders. Moreover, even higher-order integration resulted in a larger residual than first-order integration with the linear quadrilateral element (Q4). However, integration with a higher-order improved accuracy for quadratic and cubic elements. The figure also shows that third-order or higher integrations are appropriate for the quadratic element, and fifth-order integration shows the best accuracy for the cubic element.

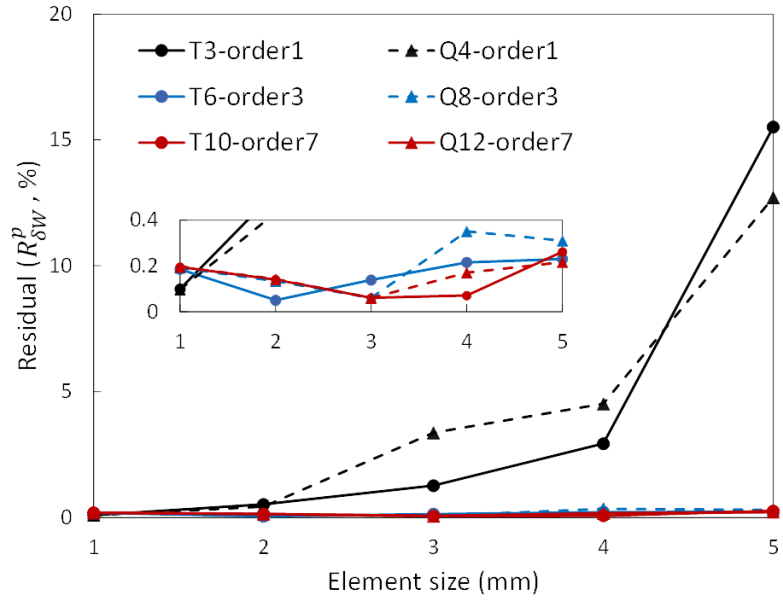

(a)

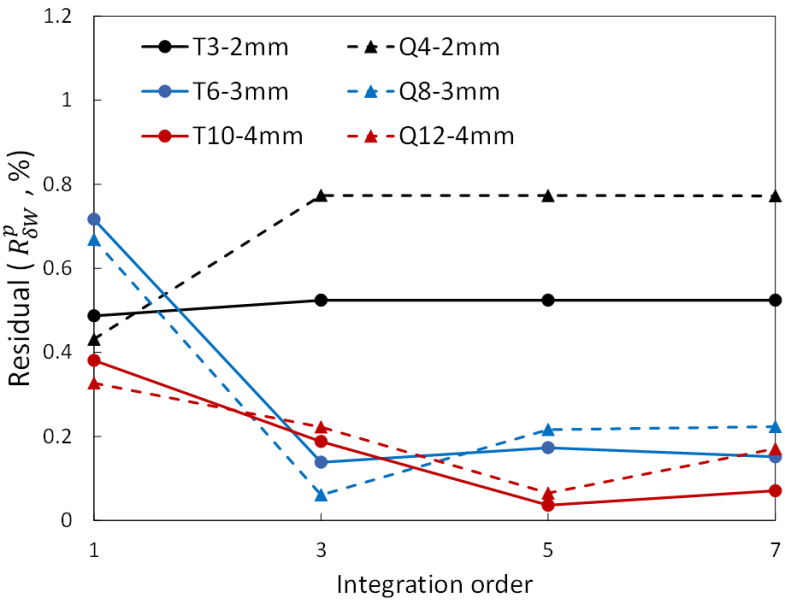

(b)

Fig. 3-13. Residuals of FE-VFM virtual work for elastic-plastic material with respect to (a) element size and (b) order of integration

Fig. 3-14 shows the results of parameter identification for the plastic strain hardening law using the FE-VFM. The non-linear optimization of the cost function was conducted using the MATLAB® built-in non-linear least-squares optimization function *lsqnonlin*.

For the quantitative analysis, the average error of the equivalent stress is defined as follows:

$$\mathrm{R}_{\sigma}^{P}=\frac{1}{\bar{\varepsilon}_{a}}\int_{0}^{\bar{\varepsilon}_{a}}\left|\frac{\bar{\sigma}_{\mathrm{VFM}}-\bar{\sigma}_{\mathrm{target}}}{\bar{\sigma}_{\mathrm{target}}}\right|d\bar{\varepsilon}\times 100(\%) \tag{3.11}$$

where $\bar{\sigma}_{\mathrm{VFM}}$ is the equivalent stress obtained from the FE-VFM, $\bar{\sigma}_{\mathrm{target}}$ is the corresponding input equivalent stress (or exact target value), and $\bar{\varepsilon}_{a}$ (=0.3 in this study) is the limit of the equivalent plastic strain range for the average error calculation.

Fig. 3-14(a) shows that the error in the equivalent stress increases as the element size increases when linear elements are used. However, the error becomes significantly lower regardless of the element size in the case of higher-order elements. This indicates that the deformation fields can be reconstructed well for the higher order elements even with quite large element sizes. In contrast, linear elements do not describe highly deformed fields properly owing to the linearity of the shape functions. Fig. 3-14(b) shows that the quality of the FE-VFM is not improved for a linear triangular element, even with higher-order integration. Additionally, it is not clear if the increased

order of integration reduces the error in equivalent stress for the quadratic triangular element. However, for quadrilateral elements, higher-order integration showed better accuracy in identifying the hardening parameter.

The sensitivity tests described above clarified that the proposed FE-VFM could be an effective inverse identification method for elastic-plastic materials. This was attributed to the robust reconstruction of the full-field displacements. In particular, the present sensitivity study verified that the deformation field reconstructions were accurate for even coarse meshes if elements of higher order were used. In addition, the newly implemented Gauss quadrature for integrating the IVW could improve the VFM quality in combination with element types that are selected properly.

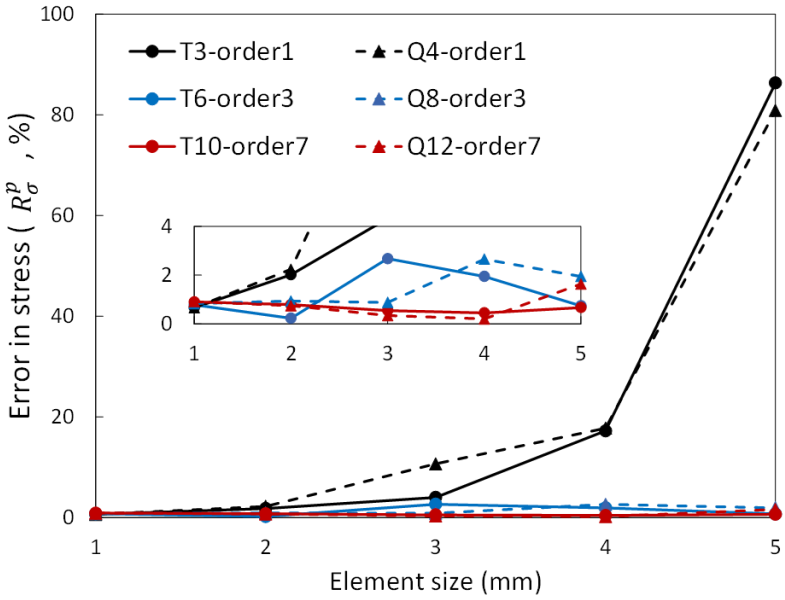

(a)

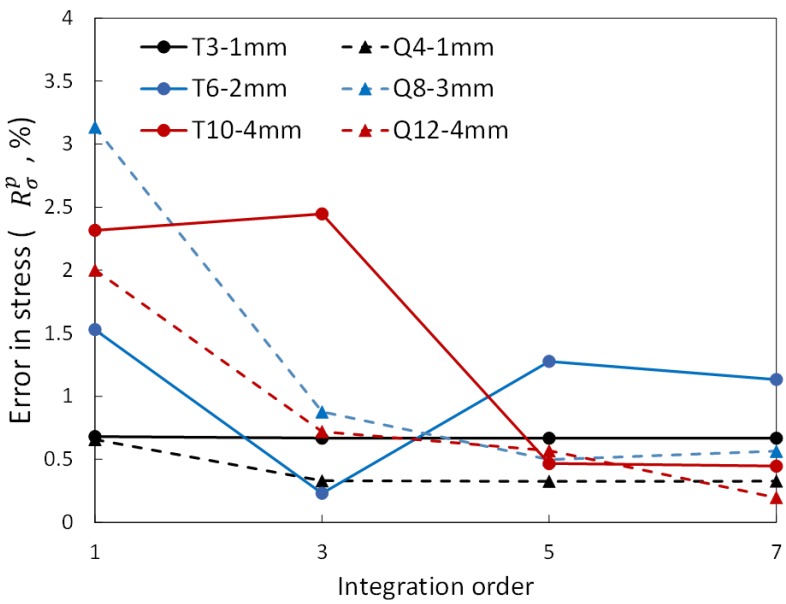

(b)

Fig. 3-14. Mean equivalent stress error of FE-VFM for elastic-plastic material with respect to (a) element size and (b) order of integration

3.3. Summary

Extensive sensitivity tests for the validation of the proposed FE-VFM were performed with ideal deformation fields generated by finite element simulations for both orthotropic linear elastic and isotropic elastic-plastic cases. FE-VFM conditions tested in this study were (1) FE mesh size from 1 mm to 5mm, (2) FE order from linear to cubic elements, and (3) Gauss quadrature order from 1 to 3.

The sensitivity study showed that the element size and order of the shape function had a minor effect on the quality of the VFM for the elastic material. The virtual fields selection, rather than the FE meshes, critically affects the quality of the results. Moreover, a higher-order Gauss quadrature improves the accuracy of IVW calculation when complex virtual fields are used.

In the case of elastic-plastic material, the element size and the order of an element, and the order of the Gauss quadrature had a considerable effect on the accuracy of the identified material parameters, which resulted from the spatial non-linearity of the large plastic deformation. It was also shown by validation that even coarse FE meshes could give satisfactory accuracy in the FE-VFM when higher order elements and Gauss quadrature were adopted.

4. Application I: homogeneous strain hardening of AHSS sheets

4.1. Introduction

The limitation of the sensitivity study presented in Chapter 3 is that the inputs are generated by FE simulations; thus, the full-field quality is almost ideal. On the other hand, experimental data often involve numerous experimental artifacts or uncertainties. Therefore, identification of the plastic strain hardening parameters for the metal sheets is presented as a real application in this chapter.

Before applying FE-VFM to the experimental data, new types of virtual fields namely pseudo-real deformation field (PDF) is proposed. As mentioned in the introduction, the virtual fields act as an amplifier or a filter, consequently, it affected the VFM results. However, conventional polynomial virtual fields are stationary in a time frame, hence it cannot properly utilize the information at the highly deformed region for the elastic-plastic case. In this work, virtual fields constructed with nodal displacements of the FE-VFM are tested as a potential candidate of the virtual fields based on ideal deformation data that are already used in Chapter 3. Then, further modification was made to apply PDF to the experimental data that include unavoidable experimental flaws, especially in the elastic early deformation stage. Detailed information on the new virtual fields, is shown in Section 4.2.

Conventionally, plastic strain hardening of the metal sheets is measured using uniaxial tensile tests. However, experimental data of the uniaxial tensile tests can only be used up to UTS, since stress and strain in the gauge section are no more uniform and uniaxial after the UTS due to the necking [94–96]. Usually, strain hardening in the post-necking is extrapolated using tensile test data before the necking based on strain hardening law equations such as Swift and Voce equation [3,4,97], which is essentially just a fitting equation. The difficulty to apply such a method in advanced high strength steels is that the uniform elongation (that corresponds to the UTS) is often very short [98–100], yet accurate strain hardening in the post-necking is required for the accurate simulations.

Various characterization methods for strain hardening in the post-necking are proposed in the literature. One simple method is inversely optimizing parameters of the strain hardening law through iterations of finite element simulations that can match the measured global behavior such as displacement-load curves. Chung et al. inversely calibrated the hardening behavior of the spot-welded steel sheets [101]. Mohr and Marcadet also optimized a post-necking strain hardening using iterative finite element simulations [102]. In their work, Swift and Voce fit based on tensile tests were assumed as a lower and upper limit of the true stress-strain behavior, and the linear combination ratio of those two laws was inversely characterized.

Meanwhile, DIC data was utilized for the characterization of the post-

necking hardening. Paul et al. used DIC strain values to correct the local stress-strain behavior in the necked region [103,104]. Marth et al. also used DIC data to inversely calibrate the post-necking stress-strain behavior. Hao et al. performed the finite element model update in conjunction with DIC data [105]. The VFM is also used for the optimization of the metal's strain hardening law. Grédiac and Pierron applied VFM to the identification of the elastic-plastic constitutive parameters based on double notched shearing tests [106], Kim et al. characterized a post-necking behavior of the metal sheets using VFM with tensile tests [81].

The target materials in this study were 1470 MPa grade press-hardened steel (1470 MPa PHS) sheets. Notched tensile tests were employed to apply the FE-VFM, and new virtual fields introduced in Section 4.2 were used simultaneously. Detailed conditions of the experiments and FE-VFM are presented in Section 4.3. In addition, the results of the FE-VFM and the validity of the results are shown in Section 4.4.

4.2. New virtual fields: Pseudo-real deformation fields

4.2.1. Concept of the PDF

In this section, a new type of virtual field, namely the PDF, is introduced. In the context of VFM, virtual fields are not only test functions for establishing equilibrium equations in weak form but are also filters or amplifiers for obtaining better accuracy for the identified parameters. For elastic materials, virtual fields play a more dominant role as filters of experimental noise because of the small strains in elastic specimens. In contrast, for plastic materials, the signals from large plastic deformation overwhelm the effect of noise. In other words, the virtual fields should be selected properly to amplify meaningful information from the measured full-field data. In common metallic materials, deformation is accompanied by strain (or work) hardening. Before metal yields, the strain distribution of the metal is nearly uniform in the specimen gauge, but it becomes significantly inhomogeneous at a large strain owing to the plastic hardening. Therefore, conventional virtual fields that are represented as constant polynomials over time steps may lead to inaccurate identification of plastic properties.

In this study, a new strategy for generating virtual fields directly from a real (experimental) deformation field is proposed. The advantage of real deformation as a candidate for virtual fields is that it readily satisfies the boundary conditions and symmetry under given test conditions, and strains

are large at the region where the large plastic deformation occurs. An additional constraint of the new virtual fields is that they should be constant at the force boundary, as in the conventional method in Eq. (2.7). Under the FE-VFM, this constraint can easily be satisfied by simply substituting real nodal displacement values along the force boundary with certain constant values. Then, the virtual fields can be given as interpolated fields of the modified real nodal displacements. Owing to the characteristics informed by real deformation and the post-numerical modification process, the new virtual fields are defined as *pseudo-real deformation fields*.

The following equations, Eqs. (4.1)–(4.2), are sets of virtual fields for testing the newly proposed PDF.

$$\text{P-VF1} \quad \begin{cases} \delta x_1 = 0 \\ \delta x_2 = \dfrac{2X_2}{L_2} \end{cases} \tag{4.1}$$

$$\text{P-VF2} \quad \begin{cases} \delta x_1 = \left(\dfrac{2X_1}{L_1}\right)\left(\left(\dfrac{2X_2}{L_2}\right)^2 - 1\right) \\ \delta x_2 = \left(\dfrac{2X_2}{L_2}\right)^3 \end{cases} \tag{4.2}$$

$$\text{N-VF1} \quad \delta u_i^n = \hat{u}_i^n \tag{4.3}$$

$$\text{N-VF2} \quad \delta u_i^n = \frac{\hat{u}_i^n}{\max\left(\hat{u}_i^n\right) - \min\left(\hat{u}_i^n\right)} \tag{4.4}$$

N-VF3 $\delta u_i^n = \dfrac{L_i \hat{u}_i^n}{\max\left(\hat{u}_i^n\right) - \min\left(\hat{u}_i^n\right)}$ (4.5)

N-VF4 $\delta u_i^n = \dfrac{10 L_i \hat{u}_i^n}{\max\left(\hat{u}_i^n\right) - \min\left(\hat{u}_i^n\right)}$ (4.6)

where L_1 and L_2 are the width and height of the specimen, respectively, and $\hat{u}_i^n$ is the modified nodal displacement.

Eqs. (4.1) and (4.2) are polynomial virtual fields (P-VF1 and P-VF2) for comparison with the new virtual fields. In Eq. (4.3), the virtual nodal displacements are defined as real displacements without further modification (N-VF1). The virtual fields in Eq. (4.4) are the modified real displacements normalized by the difference between their maximum and minimum (N-VF2), which have a value that varies from -0.5 to 0.5. The modified nodal displacements are normalized and amplified in Eqs. (4.5) and (4.6): In Eq. (4.5), amplification factors are applied with lengths L_1 and L_2 (N-VF3), and N-VF3 is multiplied by an additional factor of 10 to obtain N-VF4 (Eq. (4.6)).

Then, the virtual position in an element can be calculated by applying the FE shape functions to the nodal virtual displacements. The interpolated virtual fields in each element are written as follows:

$$\delta x_i = \delta u_i + X_i = N_I \delta u_{Ii}^n + X_i \quad (4.7)$$

Finally, the virtual deformation gradient can be calculated as follows:

$$\delta F_{ij} = \frac{\partial \delta x_i}{\partial X_j} = \left(\left(\frac{\partial g_\mu}{\partial r_k} \right)^T b_{\mu I} \delta u_{Ii}^n \right)^T \left(\left(\frac{\partial f_\lambda}{\partial X_j} \right)^T a_{\lambda J} r_{Jk}^n \right)^T + \delta_{ij} . \tag{4.8}$$

Note that Eq. (4.8) is the same as the real deformation gradient in Eq. (2.26), except that the fields are interpolated with virtual nodal displacements. Therefore, all variables in Eq. (4.8) are known for the parameter optimization procedure.

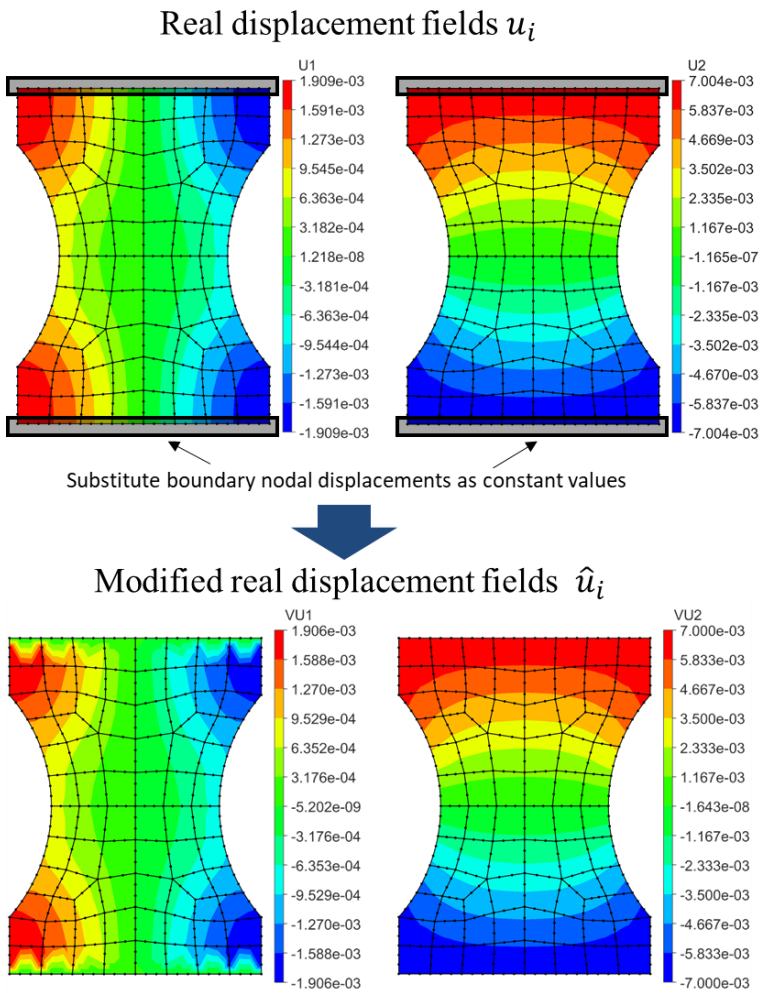

Fig. 4-1. Modification of real displacements for pseudo-real displacement virtual fields. Constant nodal displacement values are substituted to force boundaries

4.2.2. Validation of the PDF

To test the concept of the PDF, the FE simulation data used for the sensitivity study of the elastic-plastic notched tension in Chapter 3 are employed. The type and size of the elements are Q12 and 4 mm, respectively. Fig. 4-1 shows the real displacement fields and their modification for setting up the PDF. Here, the nodal displacements at the force boundaries are replaced with an averaged displacement of each boundary.

The parameters for the plastic hardening law in Eq. (3.2) and Table 3-2 are identified using the virtual fields listed in Eqs. (4.1)–(4.6). For comparison, the errors of the equivalent stress (Eq. (3.11)), and the errors of the material parameters are calculated. The results are shown in Fig. 4-2, and the values are listed in Table 4-1.

Table 4-1. Identified Swift hardening parameters and errors in stress for different virtual fields test results

	Swift law parameters			Error in stress, R_σ^P (%)
	K(MPa)	e_0	n	
Target	350.0	0.0450	0.150	
P-VF1	346.3	0.0410	0.142	0.19
P-VF2	346.5	0.0425	0.143	0.19
N-VF1	355.9	0.0488	0.158	0.70
N-VF2	356.7	0.0488	0.159	0.78
N-VF3	352.3	0.0453	0.152	0.31
N-VF4	350.4	0.0443	0.150	0.05

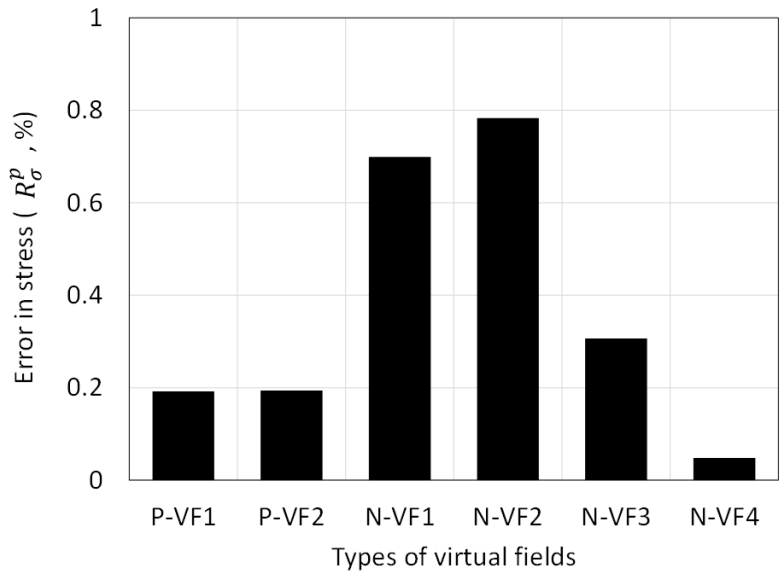

(a)

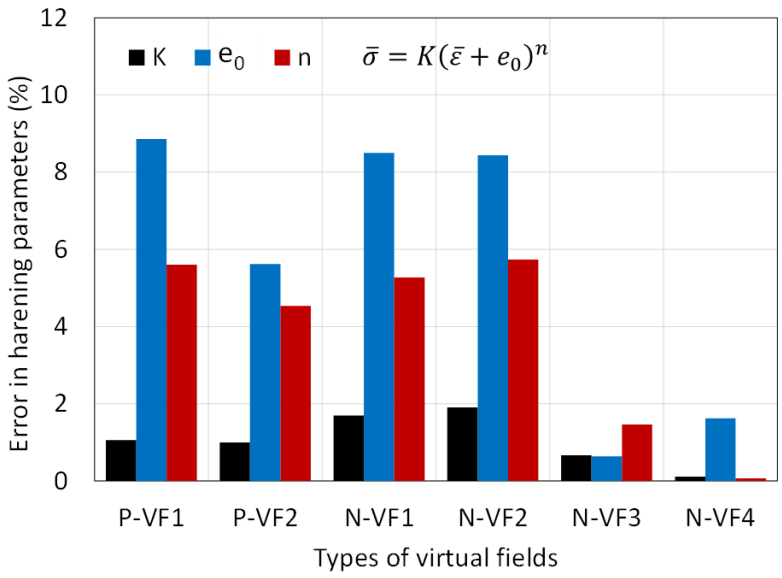

(b)

Fig. 4-2. Evaluation of virtual fields with (a) error in equivalent stress, and (b) error in Swift hardening parameters.

The errors of the equivalent stress with the two polynomial virtual fields P-VF1 and P-VF2 were approximately 0.2%, which is quite low. However, specific material parameters are relatively inaccurate with polynomial virtual fields. The discrepancy in the strain-hardening exponent n is critical because this value determines the prediction of the formability or onset of localization. The figures also show that the errors with the two new virtual fields N-VF1 and N-VF2 were not significantly better than those of P-VF1 and P-VF2. Contrary to the P-VF1/2 and N-VF1/2, the results with N-VF3 and N-VF4 showed significantly better accuracy for the identified hardening parameters when compared with conventional polynomial virtual fields. The best accuracy was obtained with N-VF4 virtual fields for the errors of both the equivalent stress and material parameters. The result indicates that the proposed concept of the PDF can accurately identify plastic parameters if amplification is properly applied.

The above results are explained in Fig. 4-3. The figure shows comparisons of the distribution of IVW density with respect to the major strain (Fig. 4-3(a)). Here, τ denotes a time step, and τ = 10, 50, 100 corresponds to an initial yielding, an intermediate step, and a final time step, respectively. For comparison, the cases of N-VF4 (Fig. 4-3(b)) and P-VF2 (Fig. 4-3(c)) are used. It can be noted that the distribution of the IVW density of the P-VF2 case does not change considerably as the deformation proceeds. In contrast, the density of IVW calculated with N-VF4 shows similar distributions of the

major strain of each deformation stage. In particular, the new virtual fields N-VF4 account for the localized deformation at the center of the specimen.

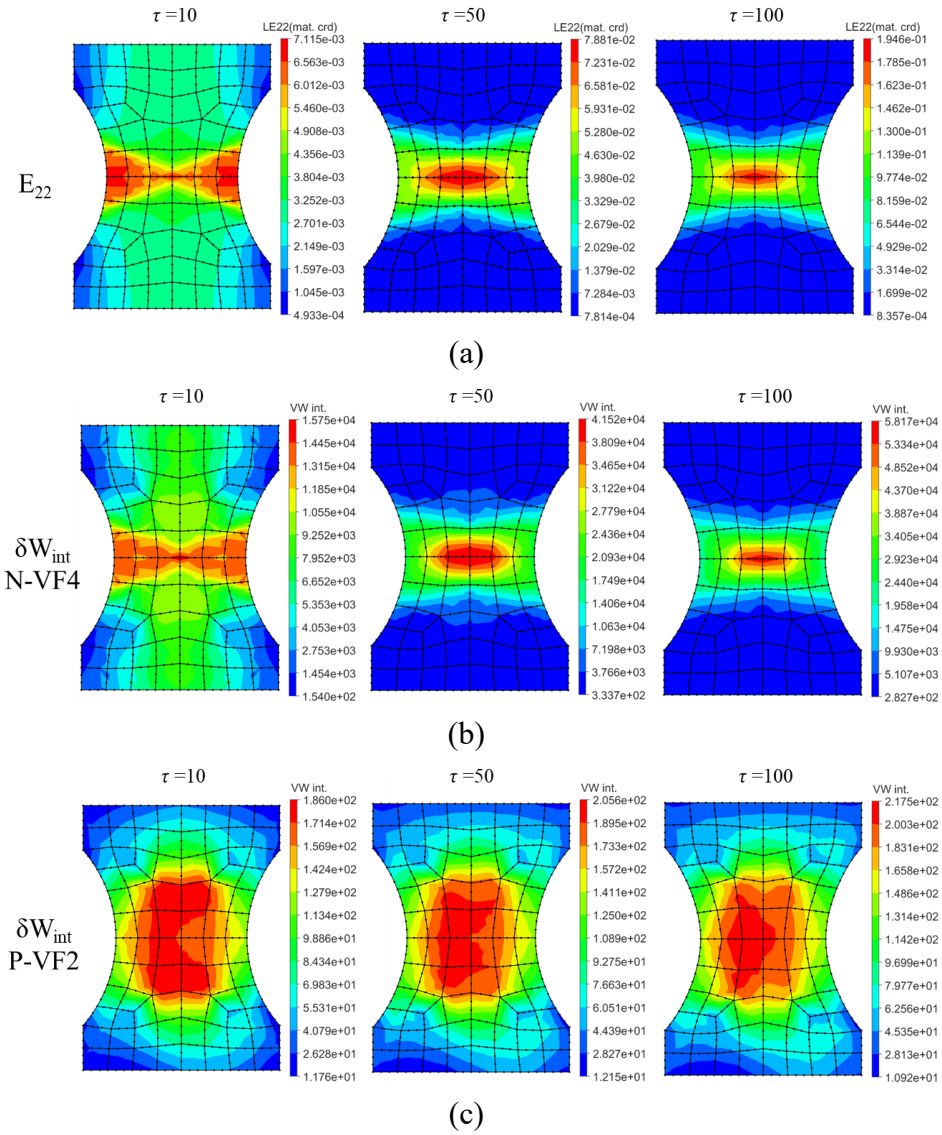

Fig. 4-3. Evaluation of density of IVW with respect to the strain along loading direction (E_{22}) at three different loading steps (τ =10, 50, 100). (a) Distributions of strain (E_{22}), (b) distribution of IVW density with N-VF4, and (c) with P-VF2.

4.2.3. Combined PDF-polynomial virtual fields for experiments

The proposed PDF virtual fields (N-VF4 in Eq. (4.6)) were proved to be an effective strategy for improving the accuracy of material parameter identification for plastic materials. However, the validations were only done for the ideal case generated by the FE simulations (for the testing of virtual fields).

However, unavoidable and unexpected flaws were contained in the experimental full-field data. The defects of the full-field data originated from the noise of non-contact measurements and experimental imperfections such as non-ideal grip conditions, small out-of-plane motions of the specimen, and imperfect alignment of the specimen. Fig. 4-4 shows an example of the effect of these flaws at an early stage of the test. The major strain distributions in Fig. 4-4(a) show a highly concentrated compressive strain at the top-left side of the specimen, which might have been caused by the experimental flaws. In Fig. 4-4(b), the IVW density distribution calculated using the PDF in Eq. (4.6) also shows an area of higher intensity at the same location. Such an effect is also found in the IVW curve in Fig. 4-4(c). In the figure, highly oscillating sharp peaks (red marks in Fig. 4-4(c)) are shown. This is caused by the PDF because the defects in the full-field data are amplified together with a true test signal. Note that the effect of these experimental defects appeared in the early elastic deformation stage and gradually disappeared with an increment in the true signal accompanied by an increment in strain magnitude.

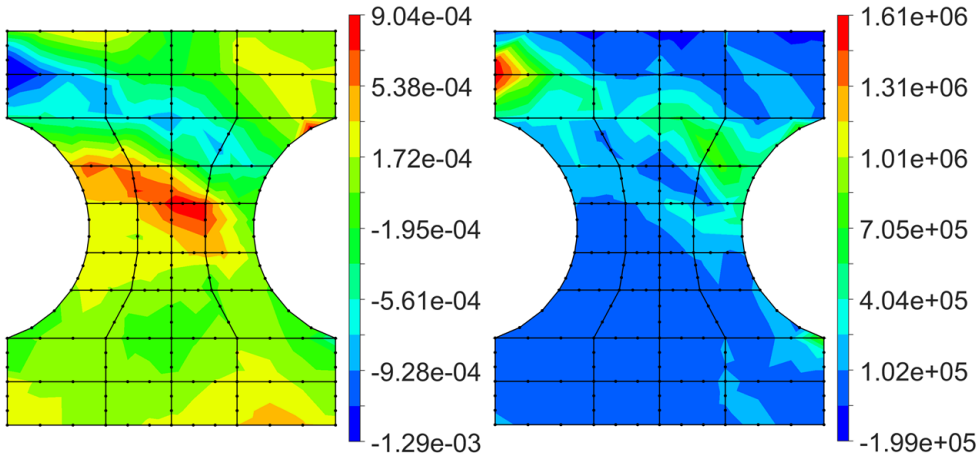

(a) (b)

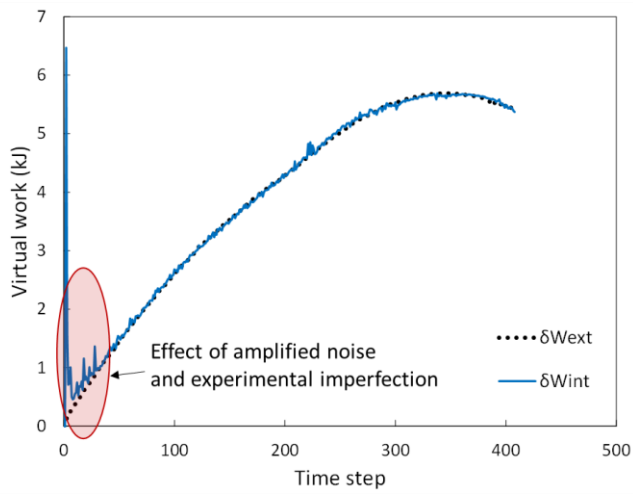

(c)

Fig. 4-4. Effect of experimental artifacts contained in the full-field measurement. (a) Major strain distribution (E_{22}), (b) IVW density distribution calculated with PDF in Eq. (4.4), and (c) IVW and EVW curves calculated with the PDF

To overcome the effect of the experimental defects at an early stage of testing, additional modifications of the newly proposed virtual fields were made. In Eq. (4.9), a linear combination of the new PDF and polynomial virtual fields is used to take advantage of both types.

$$\delta x_i = \delta u_i + X_i = ra \cdot \tilde{u}_i + (1-r)a \cdot \tilde{x}_i + X_i \tag{4.9}$$

where r is a linear combination ratio between 0 and 1, a is an amplifying factor, $\tilde{x}_i$ represents the user-defined polynomial virtual fields, X_i represents the undeformed coordinates, and $\tilde{u}_i$ represents the PDF proposed in this study. The PDF $\tilde{u}_i$ is defined as follows:

$$\tilde{u}_i = \frac{L_i}{\max\left(\hat{u}_i^n\right) - \min\left(\hat{u}_i^n\right)} \hat{u}_i \tag{4.10}$$

where $\hat{u}_i$ denotes the interpolated fields from $\hat{u}_i^n$, and L_1 and L_2 are the width and height of the AOI, respectively. Note that the PDF in Eq. (4.10) are normalized and amplified with geometrical units (the same as in Eq. (4.5)).

The linear combination ratio r is defined as an Avrami-type function as follows.

$$r = 1 - \exp\left(-\left(\frac{\tau}{\tau_p + c_{av}} \right)^{n_{av}} \right) \tag{4.11}$$

where τ is a time step number, τ_p is the time step number at which plastic

deformation is initiated, and c_{av} and n_{av} are function constants. Then, Eq. (58) shows that r is initially 0, which exponentially increases to 1 as the time step increases. In the function, the values of $\tau_p + c_{av}$ and n_{av} determine the position and slope of the transition, respectively. Then, the new virtual fields in Eq. (4.9) gradually change from the polynomial virtual fields to the PDF, which gives a better result as plastic deformation proceeds. In this study, the real undeformed position is directly used as a polynomial virtual field.

$$\tilde{x}_i = X_i \,. \tag{4.12}$$

The parameters c_{av} and n_{av} are optimized along with other material parameters in the following sections, 4.3 and 4.4. The amplifying factor a was set to 10 in this study. Additionally, the EVW is calculated using Eq. (4.13) using a constant magnitude of the virtual field δx_1 at the boundaries.

$$\delta W_{ext} = \int_{\partial s} f_i^s \cdot \delta x_i ds = \left(a+1\right) L_2 \cdot F \tag{4.13}$$

4.3. Experiment and FE-VFM conditions

In this section, the FE-VFM is validated with real experimental data. In the tests, 1470 MPa grade press-hardened steel (PHS) sheets were used. The thickness of the sheets was 1.25 mm. Owing to the low strain before the onset of diffuse necking (or before ultimate tensile strength (UTS)) in PHS steel,

the common method for obtaining true stress–strain data based on the extrapolation of flow stress often leads to less accuracy at large strains. The VFM has the potential to overcome this limitation because it can obtain reliable flow stress even after localization (or beyond uniform elongation).

In this study, an Instron 8801™ servo-hydraulic machine was used for the experiments. For comparison with the VFM, conventional tensile tests were conducted with standard ASTM E8 specimens under quasi-static conditions (strain rate of 0.001/s). Tensile tests were performed in the rolling direction (RD) of the sheets. For simplicity, isotropic linear elasticity and plasticity were assumed, and Young's modulus and Poisson's ratio were 200 GPa and 0.3, respectively.

The flow stress curves were described using the combined Swift–Voce (S–V) hardening law shown in Eq. (4.14).

$$\bar{\sigma} = K\left(\bar{\varepsilon} + e_0\right)^n + \sigma_0 + R\left(1 - \exp\left(-b\bar{\varepsilon}\right)\right) \tag{4.14}$$

where K, e_0, n, σ_0, R, and b are material constants. Note that the S–V hardening model was introduced to fit the stress–strain data more accurately than the classical Swift or Voce hardening laws.

Notch tensile tests were also adopted in applying the FE-VFM, and the dimensions of the specimen are illustrated in Fig. 4-5(a). The test speed was 1 mm/min. For the full-field measurement, the commercial stereo DIC

package VIC-3D was used. In the test, the frame rate was 6.67 fps, the total number of time steps was 408, and two different subset sizes of 31 and 63 pixels were used in post-processing.

In the post-processing for DIC, the optimal subset size varies with the quality of the test conditions. Usually, as the quality of the speckle pattern increases, the required subset size decreases. Additionally, the increased subset size reduces noise and spatial resolution [28]. Moreover, the portion of the non-measurable region at the edge of the AOI increases as the subset size increases. In Fig. 4-5(c), the areas measured by DIC are compared for two different subset sizes. In this study, DIC analyses with the two subset sizes were conducted to investigate the capability of the proposed FE-VFM with relatively low-quality full-field measurements. The detailed conditions of the DIC analysis are listed in Table 4-2.

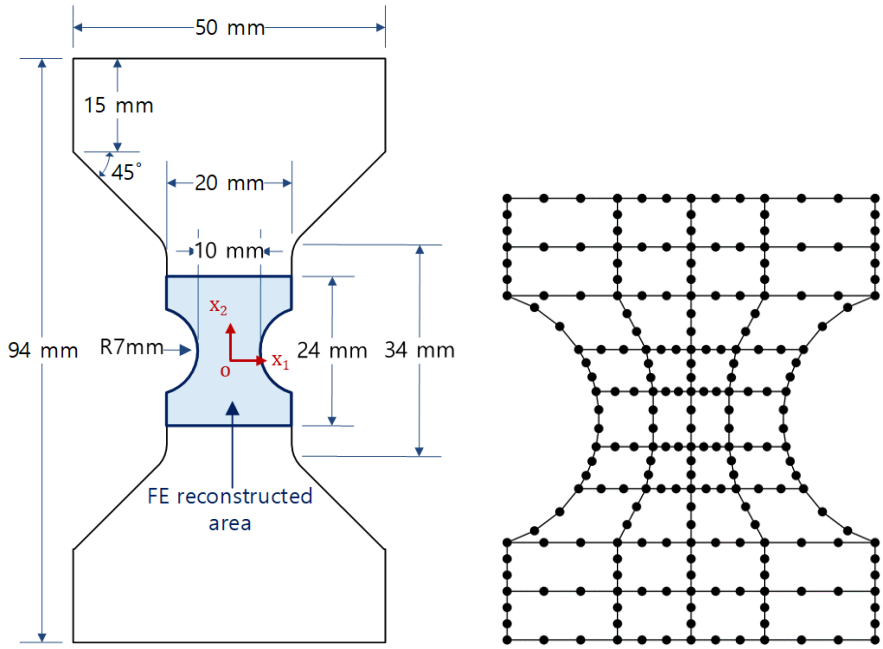

(a) (b)

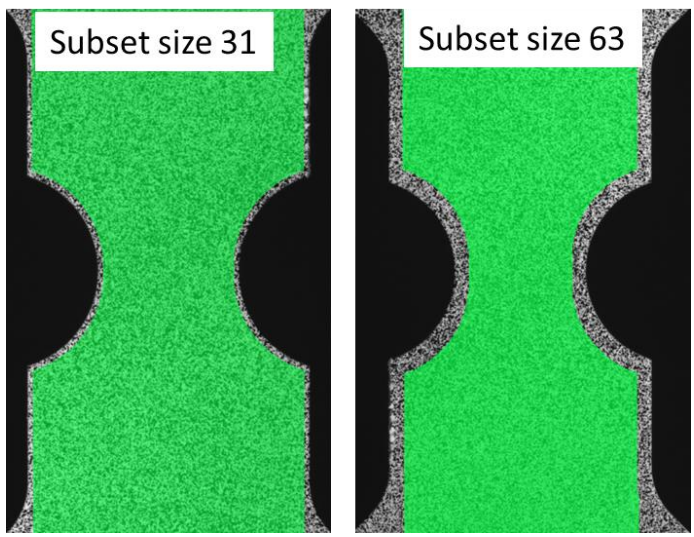

(c)

Fig. 4-5. Notch tensile test conditions for applying the FE-VFM. (a) Specimen geometry, (b) FE meshes for reconstructing displacement fields, and (c) DIC measurement areas with two different subset sizes.

Table 4-2. Conditions of DIC analysis

Software	VIC-3D 7
Resolution of CCD camera (pixels)	2448 x 2048
Frame rate (fps)	6.67
AOI area (pixels)	2192 x 914
AOI area (mm x mm)	46x20
Average speckle size (pixels)	6
Interpolation	Optimized 8-tap
Criterion	Normalized square difference
Subset size 1 (pixels)	31
Subset size 2 (pixels)	63
Step size (pixels)	3

The U-notch tensile test shown in Fig. 4-6 was also conducted for the validation of the measured flow stress curves. The test speed was 1 mm/min, and displacement was measured with a gauge length of 12.5 mm using the DIC. The experimental load–displacement curve of the U-notch test was compared with the FE simulation results predicted with the measured plastic hardening parameters.

In the FE-VFM, the cubic quadrilateral FE (Q12) meshes illustrated in Fig. 4-5(b) were used for the reconstruction of the displacement fields. The measurement of the DIC in the blue region in Fig. 4-5(a) was reconstructed. Additionally, a seventh-order integration was used in the Gauss quadrature. For the non-linear optimization of the cost function, the MATLAB® built-in

non-linear least-squares optimization function *lsqnonlin* was used. A linear combination of PDF and polynomial virtual fields in Eq. (4.9) was used due to the unexpected experimental flaws, as discussed in Section 4.2.3.

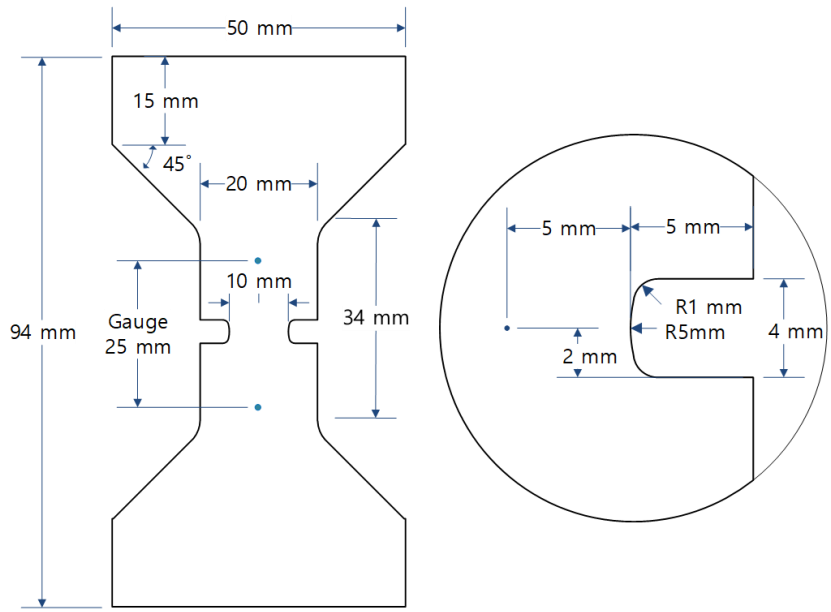

Fig. 4-6. U-notched specimen for validation of obtained material properties

4.4. Results and validations

In Fig. 4-7 and 4-8, the displacement fields measured by the DIC and their reconstructed fields on the FE mesh are presented at a time step of 300. Figs. 4-7(a) and (b) correspond to a subset size of 31 pixels, and Figs 4-8(a) and (b) correspond to a size of 63 pixels. The figures confirm that the proposed FE-based full-field reconstruction was performed well for the real experimental data. In particular, the wide edge regions with missing measurements in the AOI in Fig. 4-8(b) were successfully reconstructed with higher order FE meshes. The reconstructed displacement fields were consistent for the two different subset sizes.

Using the reconstructed displacement fields, the FE-VFM was performed by applying the new PDF-based virtual fields in Eqs. (4.9)–(4.13). Fig. 4-9 shows that the IVW and EVW are virtually identical, which proves that the non-linear cost function was well-optimized. Fig. 4-10(a) presents the strains in the loading direction(E_{22}), and Fig. 4-10(b) shows the densities of the IVW at two different time steps. The figures clearly show that the change in the IVW density during deformation is comparable to that of the strain. This indicates that the PDF effectively amplifies the effect of plastic deformation in the localized area.

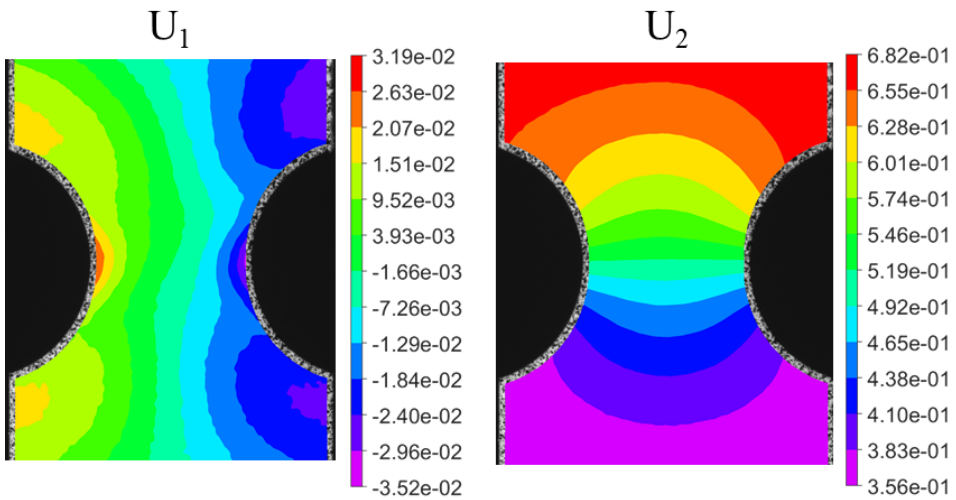

(a)

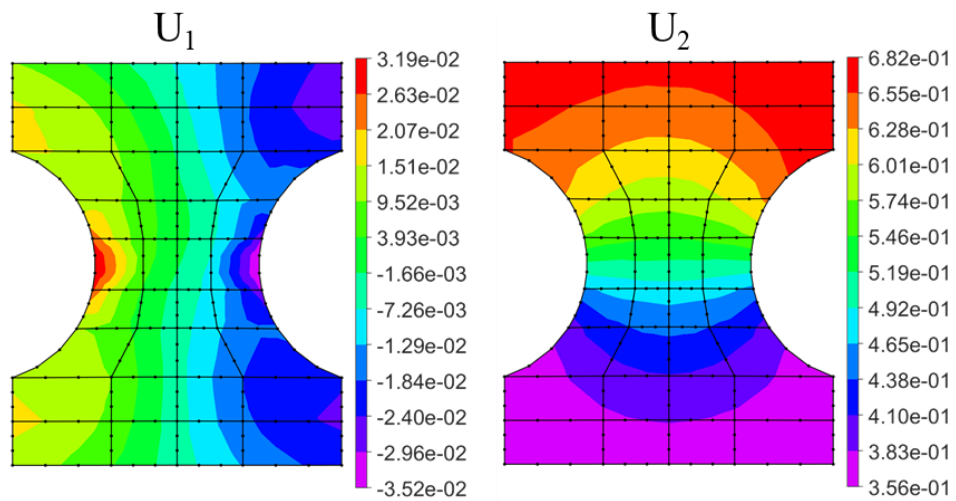

(b)

Fig. 4-7. Comparison of displacement fields. (a) DIC measurements with subset size 31 pixels, and (b) FE mesh-based reconstructed displacement fields.

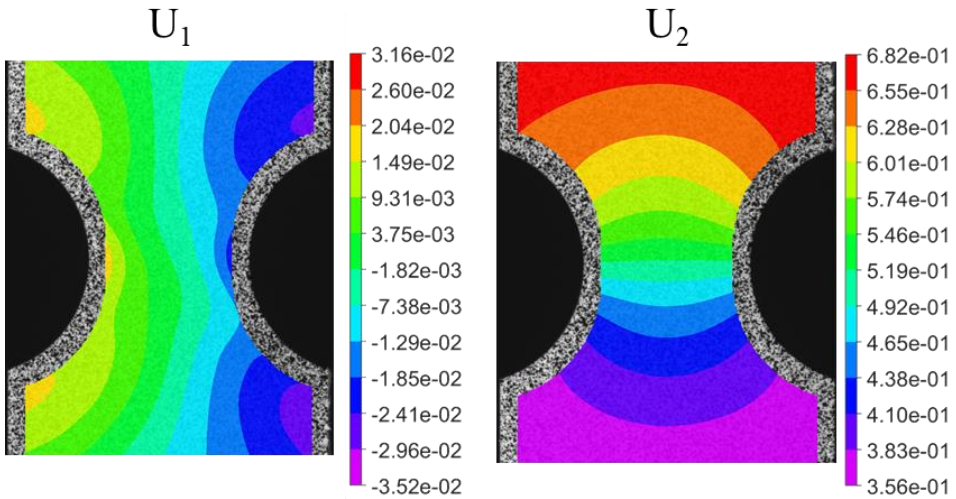

(a)

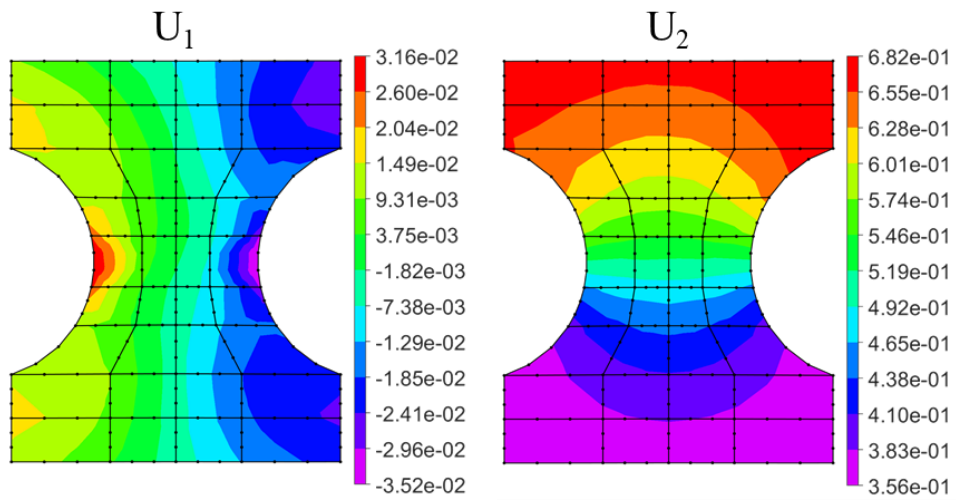

(b)

Fig. 4-8. Comparison of displacement fields. (a) DIC measurements with subset size 63 pixels, and (b) FE mesh-based reconstructed displacement fields.

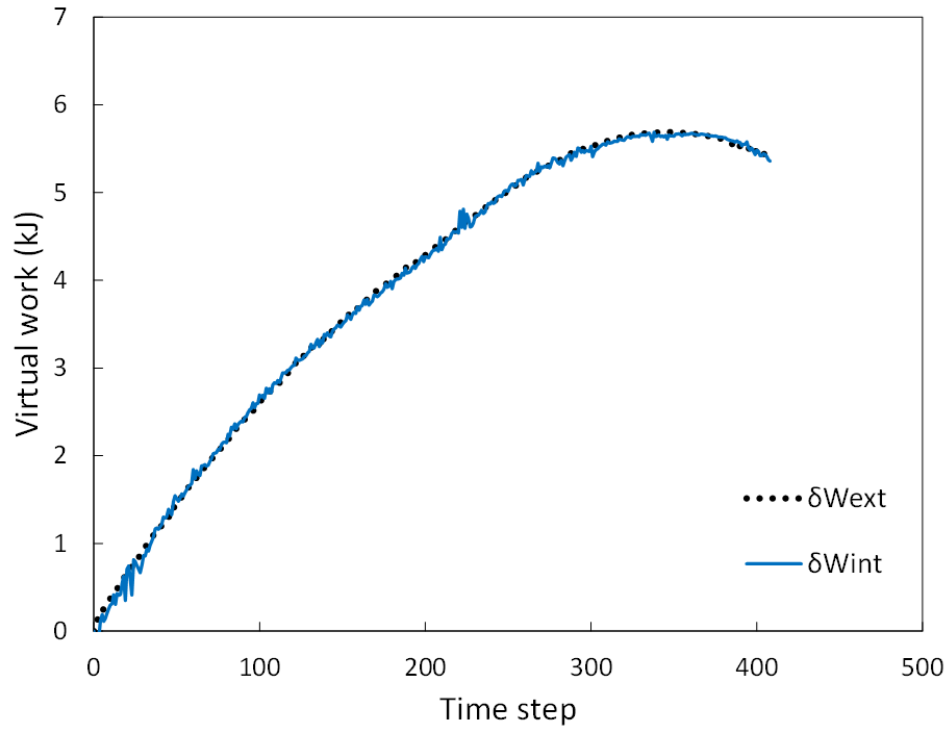

Fig. 4-9. IVW and EVW curves. The results are calculated from FE-based VFM with modified PDF virtual fields in Eq. (4.9).

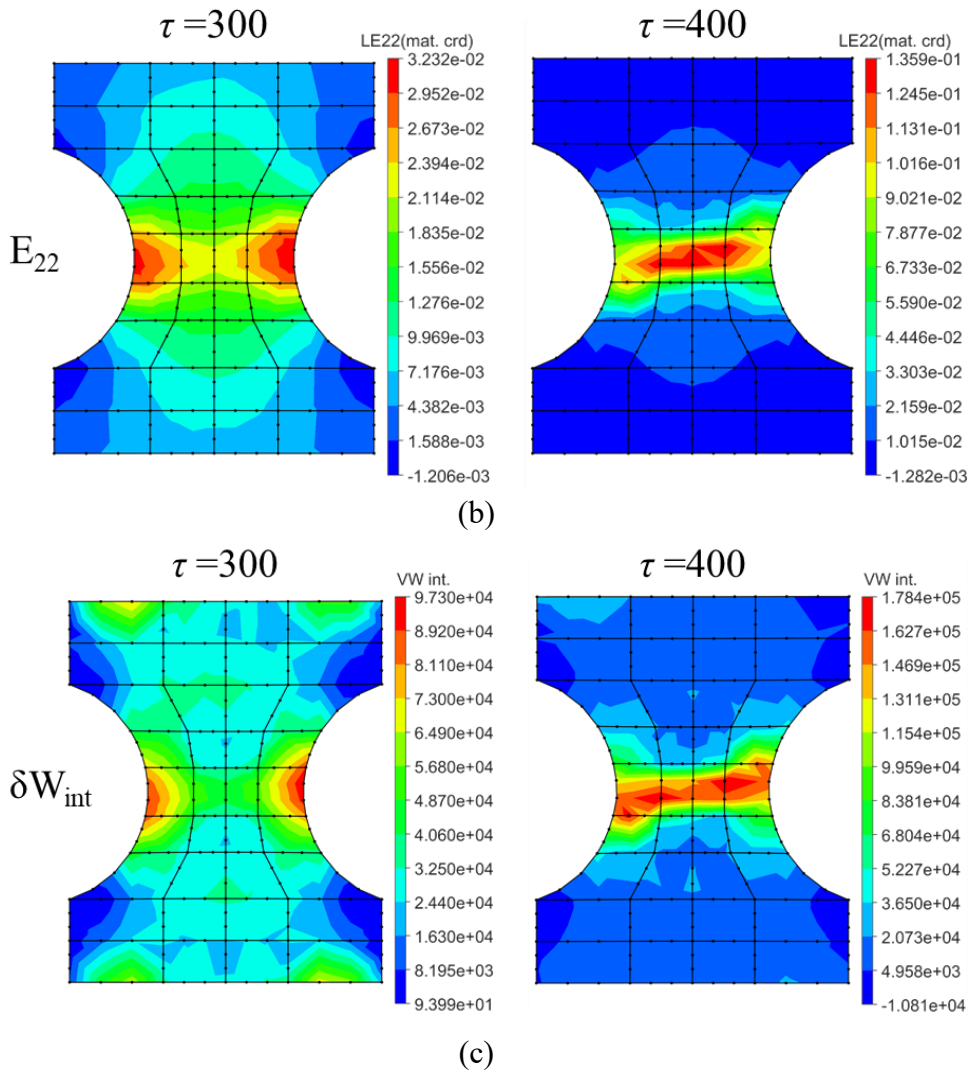

Fig. 4-10. (a) Strains in loading direction (E_{22}) and (b) distributions of IVW density at two different time steps τ=300 and 400. The results are calculated from FE-based VFM with modified PDF virtual fields in Eq. (4.9).

In Fig. 4-11(a), the equivalent stress–strain curves identified with the FE-VFM and standard tensile test are presented. It can be noted that the flow stress curves identified by the FE-VFM match very well with those obtained from the standard tensile test after moderate strain. However, the two curves show a significant difference in the yield stresses and a slight difference in the hardening slope after the point of UTS. Fig. 4-11(b) compares the load–displacement curves in the U-notch tests for the validation of the FE-VFM. For this, FE simulations were conducted with hardening parameters both for the S-V model parameters from the FE-VFM and for fitting to the standard tension. The detailed hardening parameters are listed in **Table 4-3.** The figure shows that the predicted load–displacement curve using FE-VFM results in is a better agreement with the experimental values than that of the standard tension results. In particular, the load–displacement curve predicted by the FE-VFM improved the accuracy for the early plastic region and the region after the maximum load.

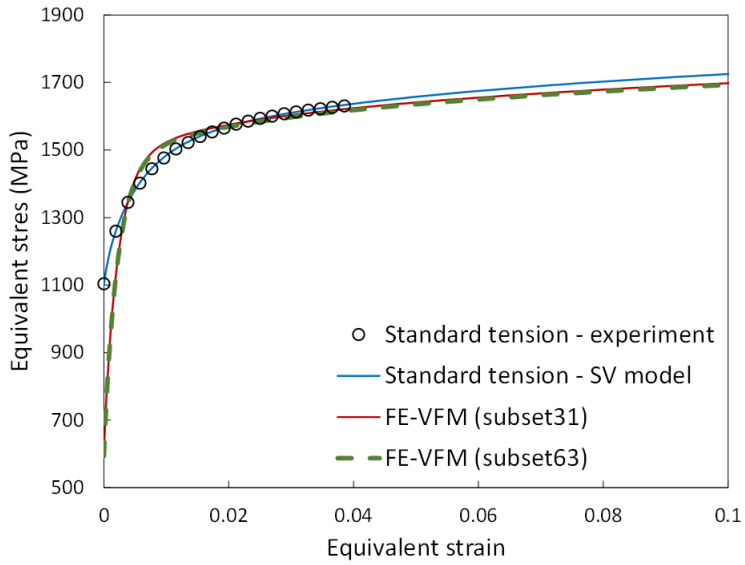

(a)

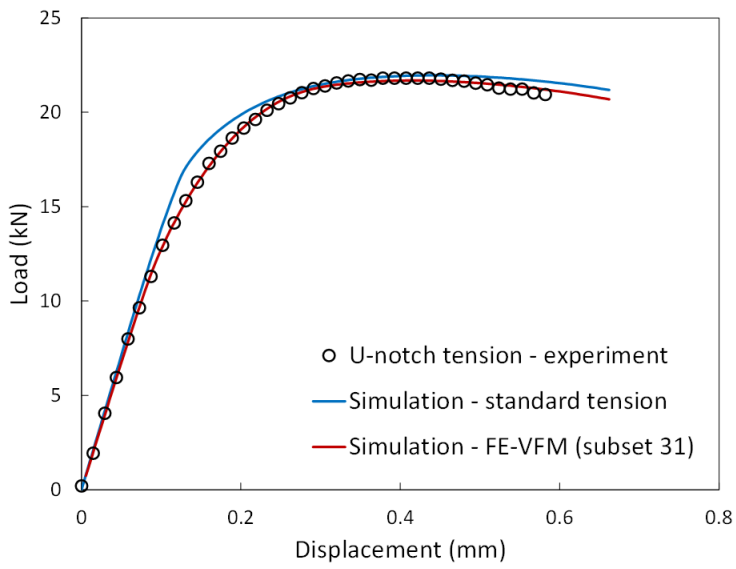

(b)

Fig. 4-11. (a) Flow stress curves identified by simple tension and FE-VFM. (b) Load-displacement curves of the U-notch tension test predicted by finite element simulations with hardening identified from either standard tension or FE-VFM.

Table 4-3. Plastic strain-hardening law parameters of combined S-V law and modified PDF parameters

	Combined Swift-Voce law parameters					
	K (MPa)	e_0	n	σ_0 (MPa)	R (MPa)	b
Standard tension	1161	0.000473	0.1141	615.4	216.4	174.8
FE-VFM (subset31)	781.7	0.000214	0.1615	406.4	752.3	447.4
FE-VFM (subset63)	785.2	0.000204	0.1628	397.0	755.9	452.4
	Virtual fields parameters					
	τ_p	C_{av}	n_{av}			
FE-VFM (subset31)	60	-20	6			
FE-VFM (subset63)	60	-20	6			

The lower accuracy in the predicted load–displacement curve of the U-notch test with the standard tension was mainly due to the commonly recommended 0.2% offset method for determining yield stress. The engineering stress–strain curve of the investigated steel sheet in Fig. 4-12 exhibits a smooth and continuous transition from elastic to plastic. Thus, the 0.2% offset method may overestimate the yield stress by ignoring the non-linear transition near the yield point. On the contrary, the VFM approach inversely identifies the yield stress based on the optimization of IVW, and thus the yield point corresponds to the elastic limit.

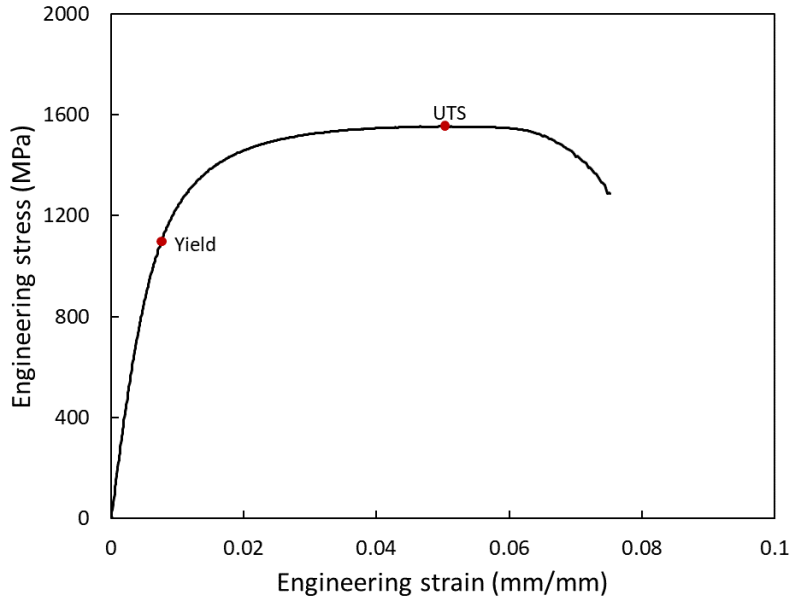

Fig. 4-12. Engineering stress-strain curve of 1470 MPa grade press-hardened steel.

Another advantage of the VFM approach is that it utilizes deformation beyond the uniform elongation (or post-UTS). Moreover, the FE-VFM with PDF enabled the amplification of information in the localized region. Therefore, the enhanced capability for acquiring large deformation data during the optimization process improves the identification quality of stress-strain behavior for high strength steel.

Fig. 4-11(a) shows that the flow stress curves identified using the FE-VFM are almost identical for the two different subset size conditions. A large subset size is beneficial in terms of the quality of DIC because it provides better correlation even with lower quality speckle patterns. Additionally, it reduces noise in the data. However, a large subset size yields lower spatial resolution

and increases the area of the edge region where the full-field data are not available. The results clarify that the proposed FE-VFM utilizes DIC data analyzed with large subsets by successfully reconstructing displacements at the edge of the AOI.

4.5. Summary

New virtual fields based on real nodal displacements were proposed to improve the accuracy of VFM at large plastic deformation, and FE-VFM was applied for the identification of the strain hardening law of the advanced high strength steels. The new type of virtual field was named *pseudo-real deformation fields* in this study to highlight the use of varying real deformation fields. The PDF proposed in this study efficiently amplified the deformation fields at a highly localized region, which significantly improved the accuracy of the identified plastic hardening parameters in comparison with the conventional (constant) polynomial-based virtual fields.

Also, FE-VFM proposed in Chapter 2 with the PDF is applied for the identification of plastic hardening in 1470 MPa PHS sheets. In the FE-VFM, notched tensile test data was used, and obtained strain hardening is validated using U-notch tensile tests. The U-notch tension load–displacement curve predicted using the FE-VFM hardening parameters showed better agreement with the experimental results than did the conventional fitting-based

hardening parameters. The improved accuracy relative to the conventional method is explained as follows. First, the commonly adopted 0.2% offset method for determining yield stress ignores the transition from elastic to plastic yielding. In this case, the conventionally determined yield stress may be overestimated, while the FE-VFM reflects the transition behavior near the yield. Second, the simple tension-based fitting to a prescribed hardening law is only valid before uniform elongation because the deformation becomes non-uniform beyond this point. The investigated PHS had a low uniform elongation (only 5%), which led to a discrepancy in the predicted deformation at large strain for the U-notched tension. However, in the case of the FE-VFM, the deformation fields in the large, localized deformation range could be utilized for identification, which resulted in better identification accuracy for plastic hardening. Note that the proposed pseudo-real deformation fields improved the quality of the VFM by capturing stress-strain data in a large deformation range.

5. Application II:non-homogeneous strain hardening of friction stir welded aluminum alloy sheets

5.1. Introduction

It is theoretically and experimentally validated that the FE-VFM can be effective and accurate for identifying homogeneous plastic strain hardening of the metal sheets in Chapters 3 and 4. In this chapter, Identification of the non-homogeneous strain hardening (or local flow stresses) of the friction stir welded aluminum alloy sheets is presented as an advanced application of the FE-VFM.

Friction stir welding is a solid-state welding process invented by The Welding Institute (TWI) in the early ’90s [107,108]. The FSW can be used for joining materials that are hard to weld with a conventional welding technique such as similar and dissimilar aluminum alloys [109–111], magnesium alloys [112–114], and titanium alloys [115,116]. Fig. 5-1 illustrates the schematics of the friction stir welding (FSW) process. FSW tool is composed of pin and shoulder, and it rotates at high speed between two workpieces. The pin of the FSW tool is penetrated through depth in between of workpieces, and the shoulder only contacted at the top surface of the workpieces. Due to the rotation of the FSW tool, frictional heat is generated, and metal workpieces are softened due to the heat. Also, softened materials are mechanically stirred, and workpieces are joined in solid-state thermo-

mechanically. As the tool moves with a rotation in a welding direction, solid-state joining progress.

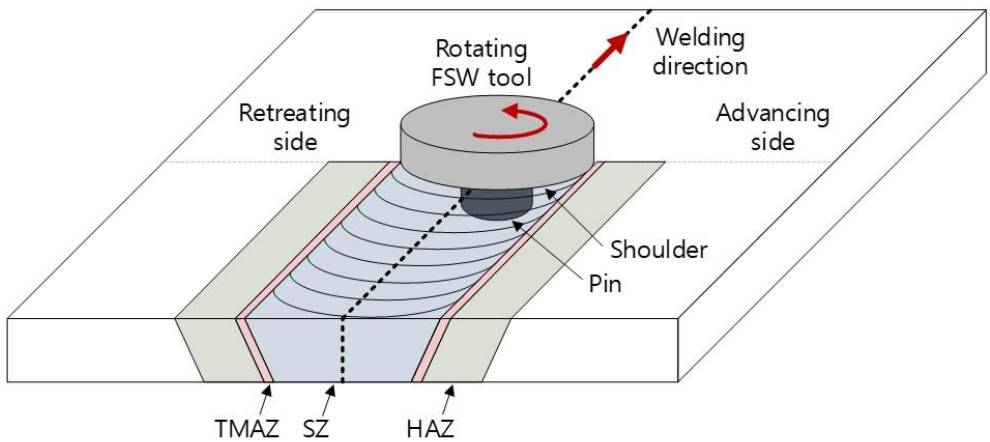

Fig. 5-1. Schematics of friction stir welding process

As with all the other welding processes, the microstructure of the workpiece changes from an as-received state due to the thermo-mechanical histories during the FSW [108,116–119]. In the friction stir welded (FSWed) materials, the weld affected zone (WAZ) can be divided into three distinctive zones. [118,120] Mechanically stirred area near the weld line is called the stir zone (SZ). The region near the tool is only affected by the frictional heat, hence it is called the heat-affected zone (HAZ). A transient region between SZ and HAZ is called the thermo-mechanically affected zone (TMAZ). The materials far enough away from the weld center remain as base materials, and it is called the base zone (BZ).

Meanwhile, a side that welding direction is the same as the tool's rotating direction is called the advancing side (AS), and a side that the two directions are opposite is called the retreating side (RS). Usually, the temperature in the AS is a little higher than the RS since more frictional heat is generated due to the higher relative speed compared to the RS, and HAZ in the AS can be larger than the RS [117,118]. For aluminum alloys, strength in the WAZ can be decreased compared to base materials strength, since it is away from the original optimum precipitation hardening conditions [108,117,118].

Accurate evaluation of such a change in mechanical properties of the weld affected zone is important for accurately predicting the post-FSW forming in the simulation. Measuring the distribution of local (micro) hardness is the most widely used technique to assess the influence of the FSW [121–123]. However, it only gives information of the relative changes of the strength compared to the base materials, since it is not material property in the strict sense. The most direct and reliable method to measure the local distribution of the "full stress-strain behavior" in WAZ is performing multiple micro or mesoscale tensile tests, with specimens fabricated in different locations in WAZ [124]. However, it requires a specially designed miniature tensile test machine, and fabrication of the small-scale specimen is also difficult.

Aside from the direct tensile tests, several inverse methods have been used to evaluate non-homogeneous mechanical properties in the WAZ in the literature. Instrumented indentation technique (IIT) is a method that retrieves

the information of the mechanical behavior inversely in the cyclic indentation test. Rao et al. used ITT for the characterization of the local stress-strain properties of the AA5083 sheets [124]. Cho et al. investigate the effect of the FSW on the ballistic limit velocity using ITT for 7xxx aluminum alloys [125]. The main weakness of the IIT is that it is an empirical approach that requires a priori knowledge about the relation between measured indentation force-depth curves and material properties, and thus the accuracy may vary from material to material. Though it can measure the local flow stresses of the friction stir welded (FSWed) materials,

The uniform stress method (USM) was also frequently used in the literature [126,127]. In the USM, stresses at every section perpendicular to the applied load are assumed as constant, and the local strains are measured by DIC in the uniaxial tensile tests. With iso-stress assumption and DIC measurements, local stress-strain curves can be constructed. The non-uniform stress method (nUSM) was also suggested as an advancement of the USM [128,129]. In nUSM, local cross-sectional areas are calculated using DIC measurement, the magnitude of the local stresses in loading direction is calibrated based on these areas. The USM and nUSM are relatively easy compared to the other complex inverse methods, however, it neglects the heterogeneous distribution of the stresses and/or complex stress components other than loading direction.

The VFM is also applied to measure the local flow stresses of the FSWed metals [130–132]. Louëdec et al. identified local static/dynamic mechanical

behavior of the FSWed AA5456 [131,132]. Shahmirzaloo et al. applied VFM for FSWed Al2024 [133]. Sutton et al. compare identification results of VFM and USM [127]. In these previous studies, AOI is divided into local subdomains, and VFM is applied independently by applying virtual fields that have non-zero values only in each subdomain, and constitutive parameters are assumed as constant in each subdomain. With this subdomain approach, local material properties can be obtained without uniqueness issues that can arise due to a large number of constitutive parameters in the global domain.

In this study, FE-VFM is applied with a subdomain approach for identifying nonhomogenous strain hardening of FSWed AA6061-T6 sheets. In addition, quadratic interpolation was used within each subdomain, so the piecewise continuous distribution of the constitutive parameters was obtained within the WAZ. Detailed information on the numerical methodology in FE-VFM is presented in Section 5.2. Before applying FE-VFM experimentally, feasibility tests were performed with finite element simulation data. As an input of the simulation, virtual nonhomogeneous strain hardening is generated using hardness distributions of the FSWed aluminum alloys in the reference. Then, a numerical sensitivity study was conducted regards the effect of the types of the virtual fields and Gauss quadrature order in the feasibility tests. Details of the feasibility tests are shown in Section 5.3. Finally, the method that was validated through feasibility tests was applied to real experiments. Information of the materials and experiments are given in Section 5.4, and the

results of the FE-VFM are shown in Section 5.5.

5.2. Methodology

In this section, it is introduced that how the nonhomogeneous strain hardening of the FSWed sheets can be extracted using FE-VFM. As discussed in the introduction, FE-VFM is applied independently to the individual subdomains to uniquely determine the local constitutive parameters. In addition, constitutive parameters are interpolated with a quadratic shape function within each subdomain, as a result, the distribution of the constitutive parameters is obtained as piecewise polynomials in the WAZ.

It should be pointed out that the majority of the workpiece has remained as as-received base materials, only the materials in the limited range vary from the original material properties affected by the welding. Also, base material properties can be easily measured using conventional tensile tests. Considering the above, it is numerically inefficient and may be inaccurate to identify all the local constitutive parameters in the entire AOI. Rather than that, it is more efficient to find the boundaries of the WAZ and obtain the local parameters only in the WAZ.

With this idea, a two-step identification procedure is used in this study. Fig. 5-2 shows the identification procedure. As a first step, WAZ boundaries are identified based on internal-external virtual work (VW) residuals calculated

with priorly known base material constants. Base material constants are measured by standard tensile tests before applying FE-VFM. The average VW residual in Eq. (5.1.) is calculated for each subdomain.

$$R_{\delta W} = \frac{1}{n_{\text{step}}} \sum_{\tau=1}^{n_{step}} \left| \frac{\delta W_{\text{int}}\left(k_{\text{base}}\right) - \delta W_{\text{ext}}}{\delta W_{\text{ext}}} \right|_{\text{at } \tau} \times 100 \ (\%) \tag{5.1}$$

where $\delta W_{\text{int}}\left(k_{\text{base}}\right)$ is internal virtual work calculated with base material parameters k_{base}, δW_{ext} is external virtual work, and n_{step} is a total number of the time step. In theory, VW residual should be zero if the materials in the subdomain are unaffected by the welding. In other words, subdomains that present high VW residuals are affected by the welding, hence boundaries of the WAZ can be easily obtained. After the first step, constitutive parameters are obtained in the identified WAZ. In this step, FE-VFM is applied for each subdomain separately.

For applying FE-VFM, a tensile specimen illustrated in Fig. 5-3(a) was used. The weld line is located at the center of the specimen, and the loading direction was perpendicular to the weld line. The origin of the global coordinates used in the FE-VFM is located at the center of the specimen. Within 70 mm length uniform region of the tensile specimen, 60 mm length area (marked with blue color in Fig. 5-3(a)) are used in the FE-VFM. The FE meshes for the reconstruction of the displacements are shown in Fig 5-3(b). The element size was 5 mm and 3 mm in width and height, respectively, and

cubic quadrilateral elements (Q12) were used. Each row of elements is treated as a subdomain, as marked with blue color in Fig 5-3(b).

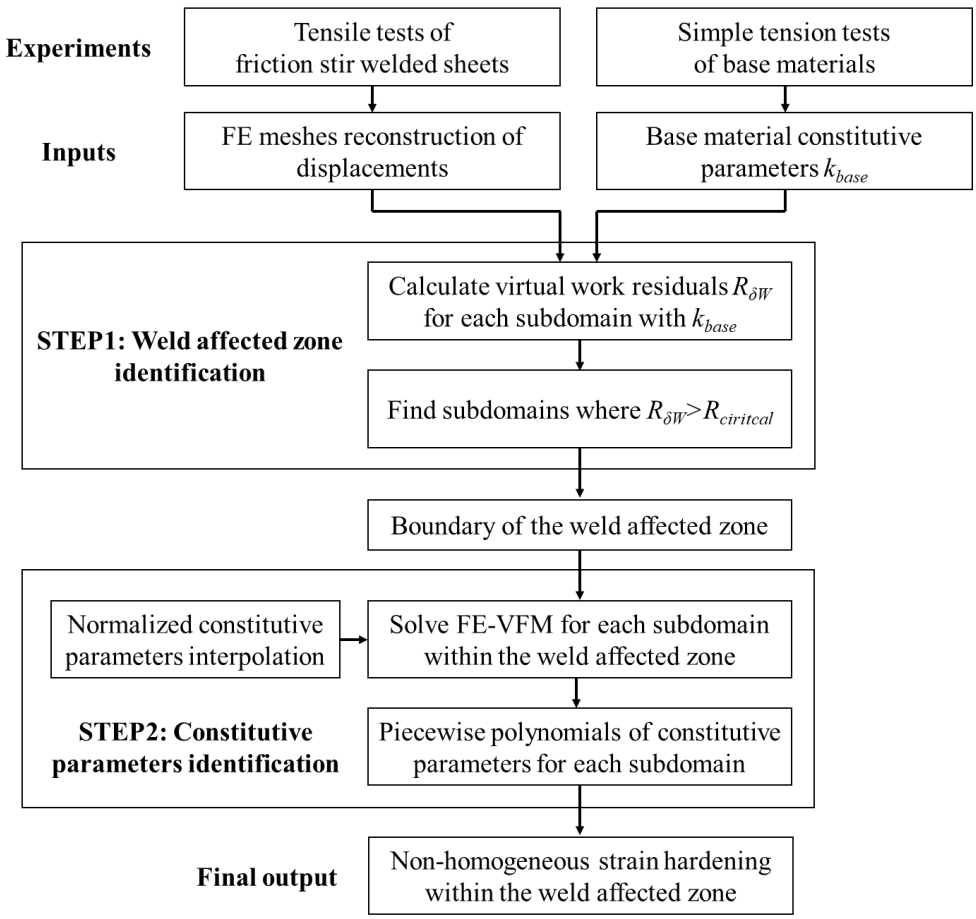

Fig. 5-2. Flow chart of two-step identification approach.

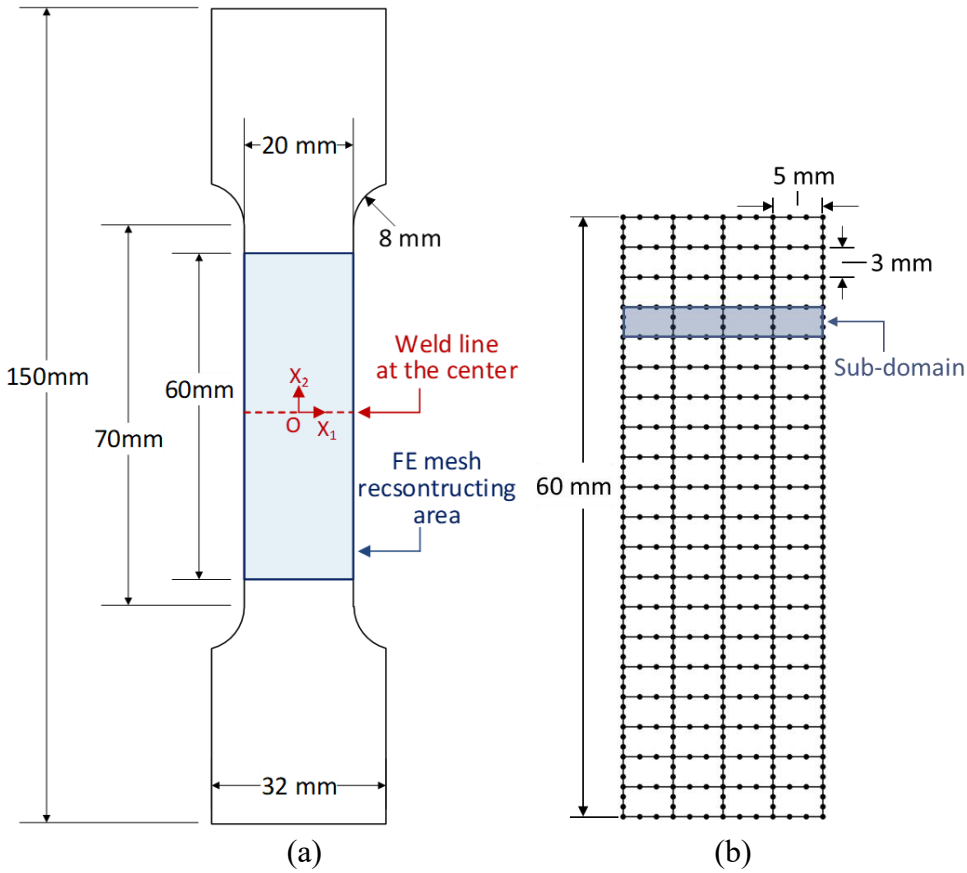

Fig. 5-3. (a) Tensile test specimen for applying FE-VFM, and (b) FE meshes for FE-VFM

Fig. 5-4 shows quadratic interpolation of the constitutive parameters in each subdomain. Constitutive parameters normalized (hereafter, normalized parameters) with known base material parameters are interpolated. The normalized parameter is

$$\bar{k} = \frac{k}{k_{\text{base}}} \tag{5.2}$$

where k denotes constitutive parameters in the subdomain, and k_{base} is base material parameters. Then, normalized parameters are interpolated with nodal normalized parameters $\bar{k}_I$ as follows:

$$\bar{k} = M_I(Y)\,\bar{k}_I\,. \tag{5.3}$$

Interpolation functions $M_I(Y)$ are given as

$$M_I(Y) = \begin{bmatrix} 1 & Y & Y^2 \end{bmatrix} \begin{bmatrix} 0 & 1 & 0 \\ 1/3 & 0 & 1/3 \\ 2/9 & -4/9 & 2/9 \end{bmatrix} \tag{5.4}$$

where the Y is coordinate in the specimen height direction, and the origin of it is located at the center of the subdomain, as illustrated in Fig. 5-4. Note that though $M_I(Y)$ is dependent on the global coordinate, the same interpolation functions in Eq. (5.4) are valid for all subdomains since the height of each subdomain is the same value, 3 mm. Virtual fields are also defined with subdomain local coordinates (X_1, Y) to assign that as non-zero values inside of the subdomain, whereas it is defined as zero at the outside of the target

subdomain.

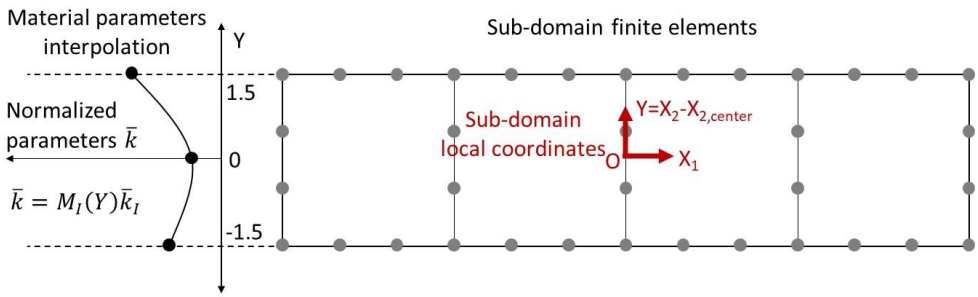

Fig. 5-4. Quadratic interpolation of the normalized constitutive parameters within a subdomain

In the WAZ parameters optimization step, nodal normalized parameters (hereafter, the nodal parameters) are obtained in each subdomain. The optimization starts from the highest subdomain in the WAZ, and one is used as an initial guess of the normalized parameters. (Which means that base material properties are used as an initial guess in the first subdomain optimization) Then, optimization proceeds for lower subdomains, and the lowest nodal parameters of the previously optimized subdomain are used as initial guesses. Average values are treated as a final FE-VFM result for the overlapped nodes between two elements

In this study, isotropic elastic-plastic constitutive laws, including isotropic linear elastic model, von Mises yield function, and isotropic hardening, are used. Usually, elastic constants are not much varied depends on the microstructure of the metals. However, plastic strain hardening or the local flow stresses can show large differences depends on the microstructure.

Considering these facts and for simplicity, elastic constants in the WAZ are assumed as the same as the base materials. And, only parameters of the strain hardening law are optimized in the WAZ, thus it was assumed as a known value. In this study, Voce and Swift hardening laws are used in the feasibility tests and experiments, respectively.

In the WAZ boundaries identification, virtual fields in Eq. (5.5) are used.

$$\begin{cases} \delta x_1 = \left(\left(\dfrac{Y}{1.5} \right)^2 - 1 \right) X_1 \\ \delta x_2 = \left(\dfrac{Y}{1.5} \right)^3 \end{cases} \tag{5.5}$$

It is simple to implement, however, it can cause the uniqueness problem in parameters optimization. Note that each subdomain has nine independent nodal parameters since Voce and Siwft law has three constants, and there are three material interpolation nodes in each subdomain. To avoid such a problem in the optimization step, normal distribution function and cumulative distribution function are used as virtual fields, as illustrated in Fig. 5-5. The virtual position vectors are defined as cumulative distribution function φ, as follows:

$$\begin{cases} \delta x_1 = 0 \\ \delta x_2 = \varphi_{i=1,2,3}(Y) = \dfrac{1}{2} \left\{ 1 + \mathrm{erf} \left(\dfrac{Y - \mu_i}{\sigma_N \sqrt{2}} \right) \right\} \end{cases} \tag{5.6}$$

where σ_N is standard deviation, and μ_i is average in original statistical use. Then, the virtual deformation gradient is given as follows:

$$\begin{cases} \delta F_{11} = \delta F_{12} = \delta F_{21} = 0 \\ \delta F_{22} = \Phi_{i=1,2,3}(Y) = \dfrac{1}{\sigma_N \sqrt{2\pi}} \exp\left\{ -\dfrac{1}{2}\left(\dfrac{Y-\mu_i}{\sigma} \right)^2 \right\} \end{cases} \tag{5.7}$$

where Φ is (statistical) normal distribution function. Three independent virtual fields are defined with three $\mu_i = -1, 0, 1$. Each virtual field amplified the data in a different range in the subdomain. With this approach, nine nodal parameters can be uniquely identified simultaneously. Detailed results and discussions about the effect of the virtual fields are shown in the feasibility tests, Section 5.3.4.

Meanwhile, sufficient order of Gauss quadrature is required for the accurate integration of the IVW. In particular, cubic elements combined with the use of the normal distribution type virtual fields may require even higher order integration, due to the significant non-linearity of the given problem. For this reason, sensitivity tests were performed in the feasibility tests, and integration order 11 was used as an optimum order. Detailed results about the integration order sensitivity are shown in Section 5.3.4.

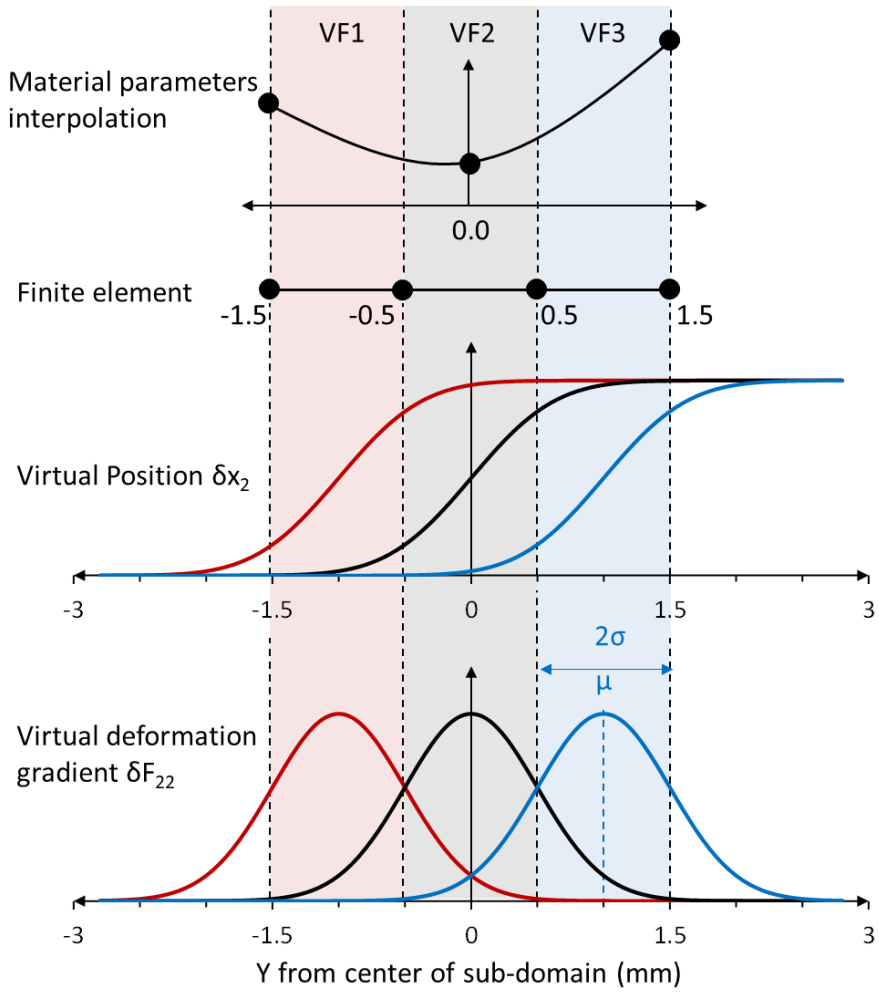

Fig. 5-5. Three independent normal distribution type virtual fields that amplifying deformation data in a different zone in each subdomain

5.3. Feasibility tests with simulation data

5.3.1. Finite element simulation conditions

Methods explained in Section 5.2 are validated using finite element simulation data. Virtual welded material properties were generated. Base material properties of the AA6111-T4 aluminum sheets and hardness distribution normalized with base material hardness were taken from the reference [123]. In the reference, Voce hardening law in Eq. (5.8) was used.

$$\bar{\sigma} = \sigma_0 + R\left(1 - \exp\left(-b\bar{\varepsilon}\right)\right) \tag{5.8}$$

where σ_0, R, and b are constitutive paramters. Values of Voce law parameters and elastic constants from the reference are listed in Table 5-1. Also, normalized hardness distribution in the WAZ in Fig. 5-6(a) was taken from the same reference. Base material hardness in the reference is 85 HV. Using hardness distribution, nonhomogeneous normalized constitutive parameters are generated with Fourier series functions in Eq. (5.9).

$$\bar{k}\left(Y\right) = a_0 + \sum_{i=1}^{8}\left[a_i \sin\left(iwY\right) + b_i \cos\left(iwY\right)\right] \tag{5.9}$$

In other words, each normalized parameter in Voce law is described with the Fourier series in the WAZ. Virtual constitutive parameter distributions are presented in Fig. 5-6(b), and detailed values of the Fourier series constants are listed in Table 5-2.

Table 5-1. Material parameters of AA6111-T4 sheets [123]

Elastic constants		Voce law parameters		
E(GPa)	ν	σ_0 (MPa)	R (MPa)	b
70	0.33	170	210	9.0

Table 5-2. Constants of the Fourier series that describe the virtual nonhomogeneous constitutive parameters

	Voce normalized parameters		
	σ_0	R	b
w	0.2105	0.2138	0.2067
a_0	0.876	1.051	0.9073
a_1	-0.1315	0.05347	-0.1005
a_2	0.02718	-0.0125	0.01605
a_3	-0.006453	0.004532	-0.001319
a_5	0.00611	-0.003496	0.001968
a_6	0.01862	-0.0007257	0.01487
a_7	0.005252	-0.001549	0.006469
a_8	-0.001504	0.006905	-0.01095
b_1	0.0129	-0.005316	0.01006
b_2	0.01346	-0.005556	0.01095
b_3	0.01377	-0.005644	0.01097
b_4	0.01467	-0.006008	0.0119
b_5	0.004259	-0.001181	0.0045
b_6	-0.006093	0.002466	-0.004153
b_7	-0.003746	0.001542	-0.003593
b_8	-0.003403	0.001243	-0.002551

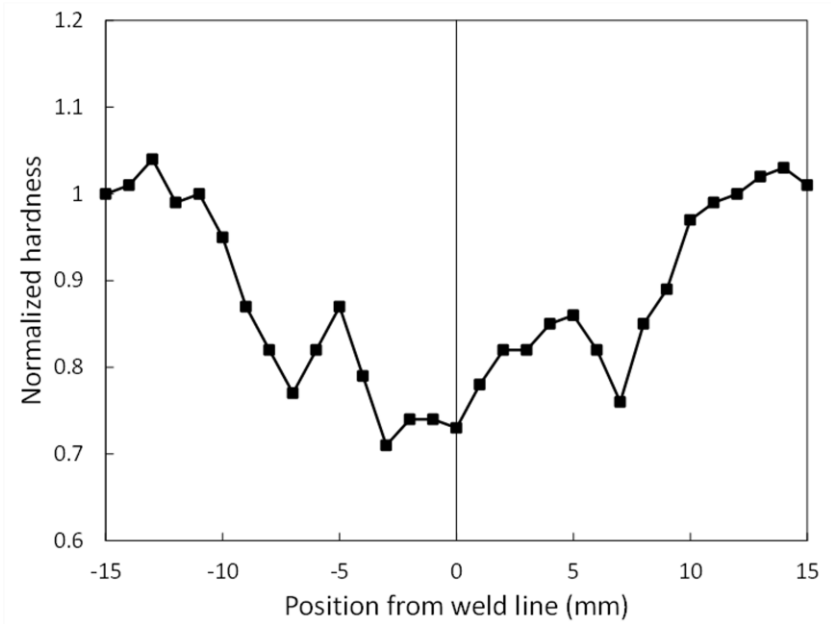

(a)

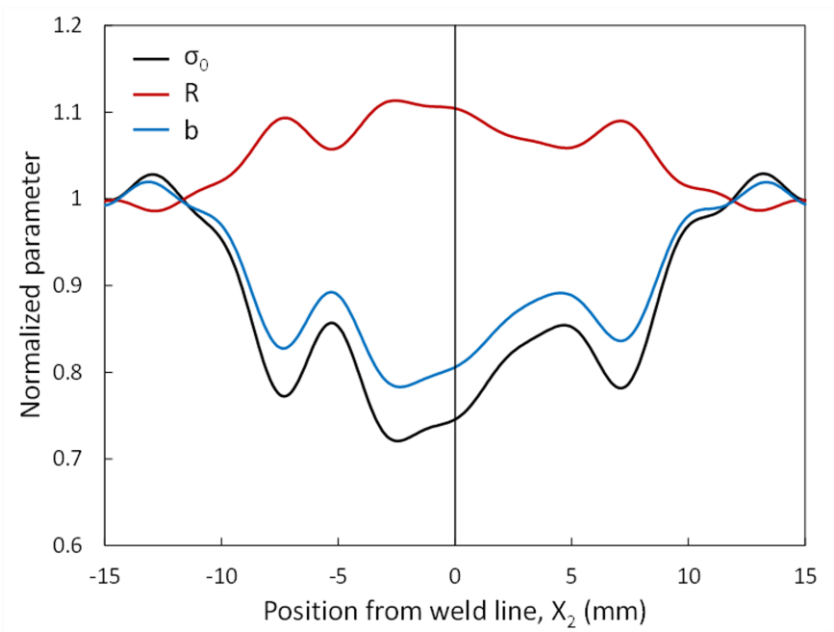

(b)

Fig. 5-6. (a) normalized hardness distribution from reference [123], and (b) Fourier series distributions of the normalized constitutive parameters generated based on reference hardness distribution

In the feasibility tests, the same specimen geometry illustrated in Fig. 5-3(a) was used. FE simulation was performed with Abaqus/standard, and subroutine UHARD and USDFLD were used to implement the nonhomogeneous material properties in Fig. 5-6. <FE model 정보 추가할 것> FE mesh in Fig 5-3(b) was used for FE-VFM. Results of simulation and reconstructed deformation fields with FE-VFM algorithm are compared in Fig. 5-7. It shows that the heterogeneous displacement and strain fields are well-reconstructed owing to the higher-order cubic elements.

In the following sections, results of the feasibility tests are presented including the WAZ boundary identification, the effect of virtual fields, and the effect of the Gauss quadrature order.

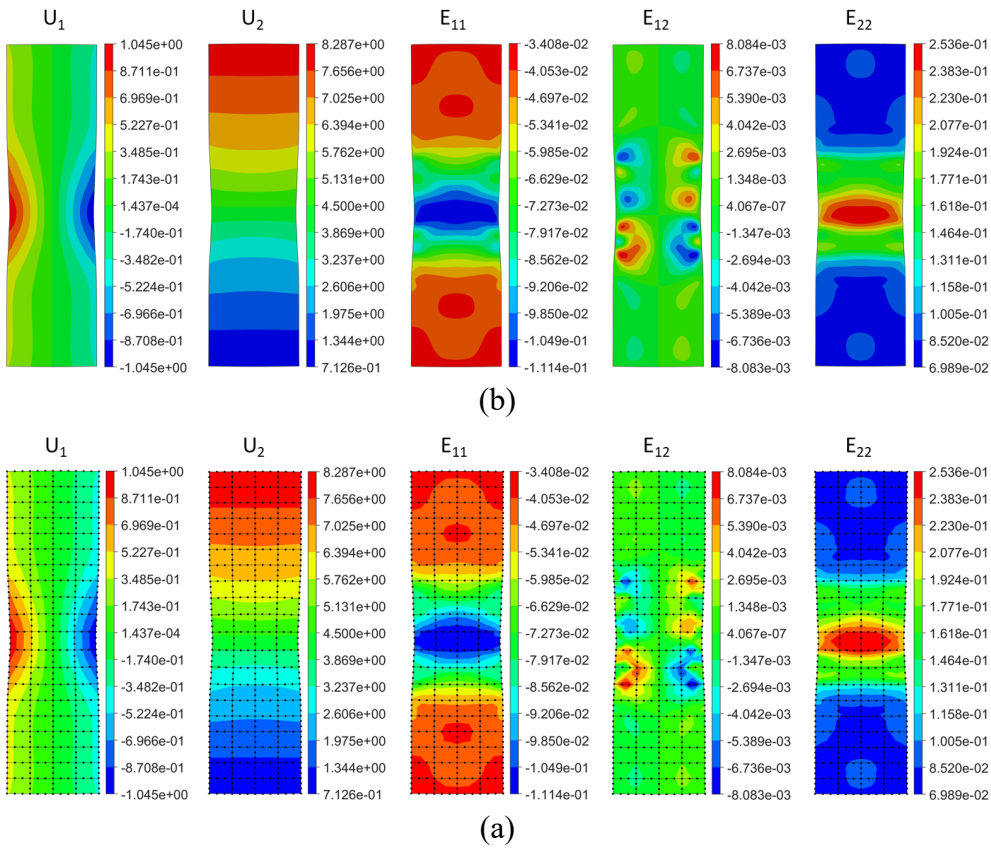

Fig. 5-7. Comparison of displacement and strain fields for the linear elastic material. (a) FE simulated deformation fields before mapping and (b) Reconstructed fields using FE-VFM

5.3.2. Identification of the WAZ boundaries

Fig. 5-8 presents VW residuals for each subdomain. VW residuals in Fig. 5-8 are calculated using base material properties of the feasibility tests, which are listed in Table 5-1. In the VW calculation, polynomial virtual fields in Eq. (5.5) were used. The integration order of the Gauss quadrature was 11. The results show that large VW residuals were calculated in the WAZ (-15 to 15 mm range), and VW residuals showed almost zero outside of the WAZ. These results validate that it is effective to find the boundary of the WAZ based on the VW residuals calculated with base material properties. The same approach is also used in the experimental case in Section 5.5.

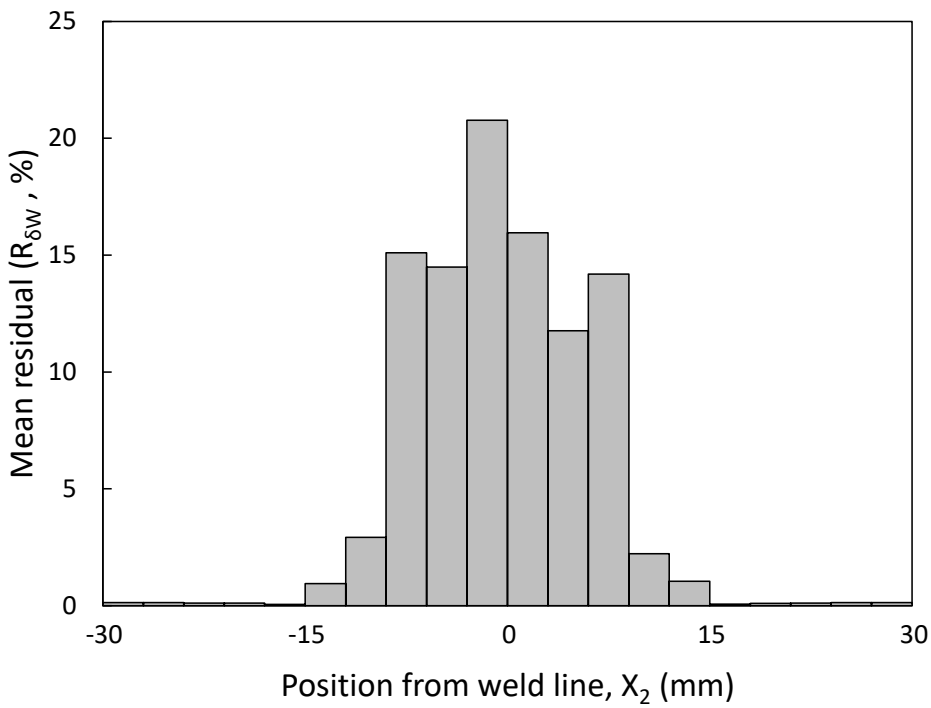

Fig. 5-8. VW residuals for each subdomain

5.3.3. Effect of the virtual fields

Followed by the WAZ boundary identification, optimization of the local flow stresses was conducted using the same polynomial virtual fields (in Eq. (5.5)) used in STEP1. However, the constitutive parameters were badly identified as shown in Fig. 5-9(a). In the 5-9(a) the solid lines are target parameter distributions explained in 5.3.1, and square dots are representing quadratic interpolation nodal values. Also, doted lines represent interpolated normalized parameters. Though the identification results are generally located close to the target lines, however, individual values are not matched with target values.

Despite the bad identification results, VW residuals after the STEP2 procedure showed less than 0.4%, as shown in Fig. 5-9(b). Small VW residuals indicate that the non-linear optimization itself was well-conducted without particular problems. Rather than incomplete non-linear optimization, the problem was made due to the parameter interpolation approach in conjunction with polynomial virtual fields. In the nonlinear VFM, The minimization is performed with the cost function of the virtual works as a scalar quantity. In that process, non-linear parameters distributions within a subdomain cannot be well-described with a single set of polynomial virtual fields, and improper zero-mode of virtual works can be made with faulted combinations of nodal parameters. This uniqueness problem can be avoided by using three independent virtual fields defined with cumulative distribution

and normal distribution functions (Eqs. (5.6) and (5.7)) in STEP2.

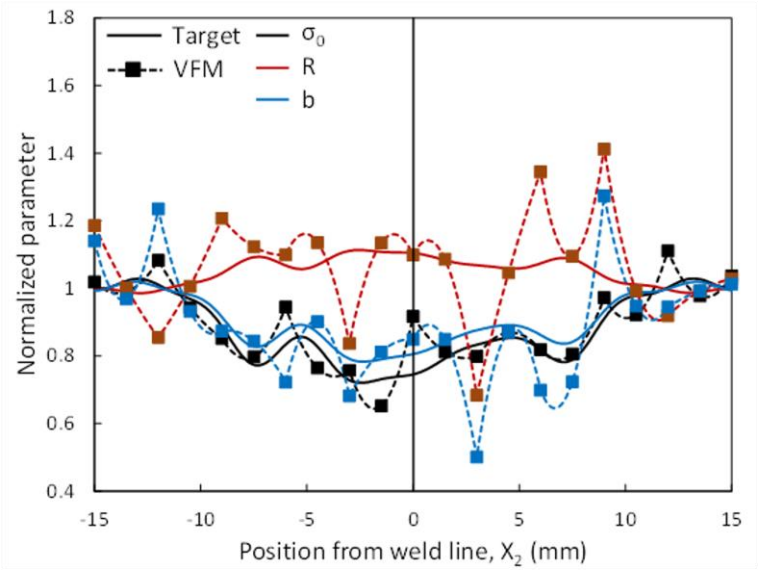

(a)

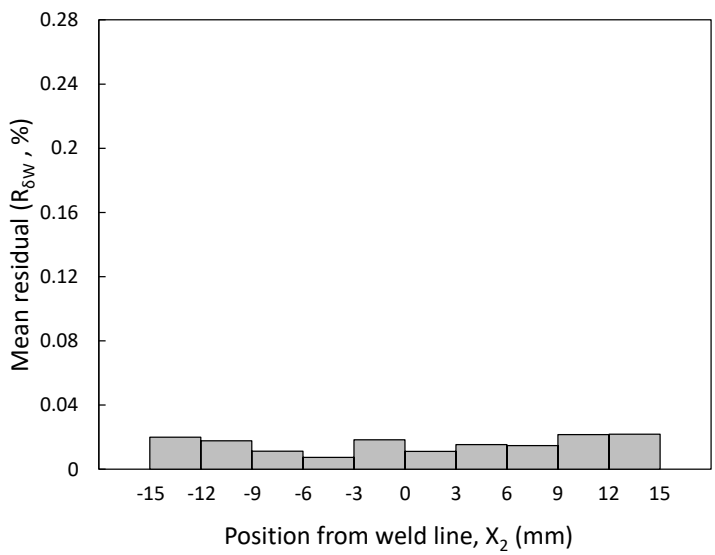

(b)

Fig. 5-9. FE-VFM results with polynomial virtual fields. (a) Badly identified constitutive parameters, and (b) small VW residuals after the parameter optimization

5.3.4. Effect of the Gauss quadrature order

As discussed in Chapter 3, the results of the FE-VFM depend on the integration order (IO) of the Gauss quadrature. In particular, the target problem defined in the methodology (section 5.2.) is highly non-linear in three aspects. First, displacements and subsequent strains are modeled with cubic quadrilateral elements (Fig. 5-3(b)). Second, quadratic interpolation was used to describe the continuous distribution in the subdomain. Third, the virtual fields are defined with highly non-linear normal distribution functions. All these factors make the problem highly non-linear, so it is necessary to use the sufficient IO of Gauss quadrature. Therefore, sensitivity tests were performed regards the IO

Fig. 5-10(a) to (c) shows the FE-VFM results with integration orders 5, 7, and 9, respectively. In Fig. 5-10(a), the results with IO 5 are near the target values, but highly oscillating. As IO increased, the oscillation of the results decreased, and it was rarely observable in Fig. 5-10(c). This is because the spurious zero-mode was calculated with the insufficient IO, similar to the hourglass modes in FEM when reduced integration is used.

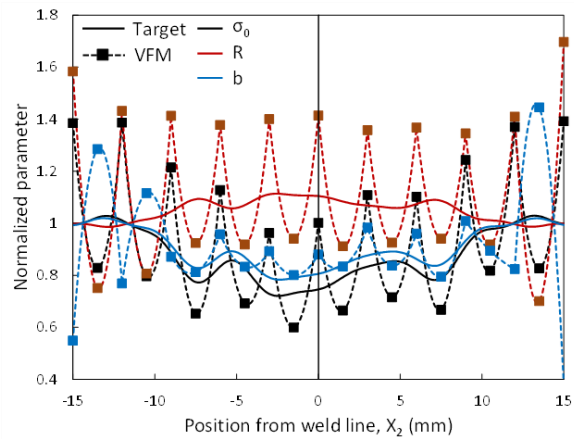

(a)

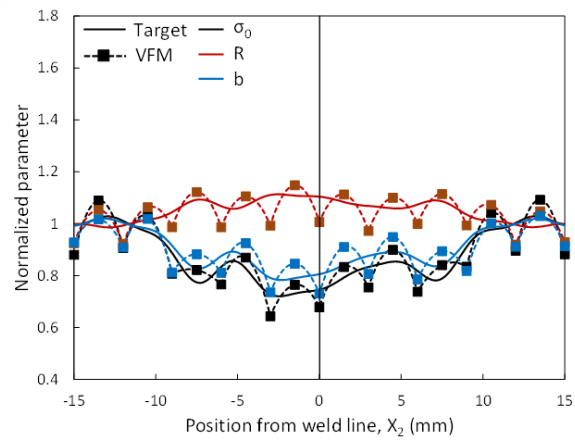

(b)

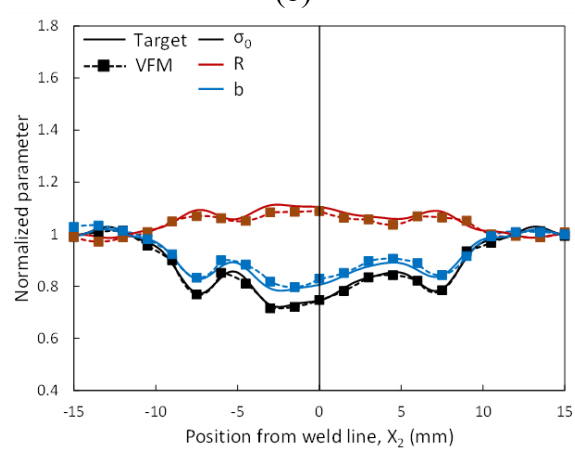

(c)

Fig. 5-10. Oscillating FE-VFM results due to the integration order. (a), (b) and (c) correspond to results of integration order 5, 7, and 9, respectively

Fig. 5-11 shows the mean errors of parameters and flow stress depends on the IO. Mean errors of the parameters in the WAZ are calculated as Eq. (5.10).

$$\bar{R}_k = \frac{1}{30}\int_{Y=-15}^{Y=15} \left| \frac{\bar{k}_{target} - \bar{k}_{VFM}}{\bar{k}_{target}} \right| dY \times 100\,(\%) \tag{5.10}$$

where $\bar{k}_{target}$ denotes input Fourier series distributions of each Voce law parameter, and $\bar{k}_{VFM}$ denotes results of the FE-VFM. Also, the mean error of the flow stresses is calculated as

$$\bar{R}_{\bar{\sigma}} = \frac{1}{30\bar{\varepsilon}_c}\int_{Y=-15}^{Y=15}\int_{\bar{\varepsilon}=0}^{\bar{\varepsilon}=\bar{\varepsilon}_c} \left| \frac{\bar{\sigma}_{target} - \bar{\sigma}_{VFM}}{\bar{\sigma}_{target}} \right| \times 100\,(\%), \tag{5.11}$$

where $\bar{\sigma}_{target}$ is input flow stress, and $\bar{\sigma}_{VFM}$ is flow stress calculated with FE-VFM results, and $\bar{\varepsilon}_c$ is strain limit for the calculation of the flow stress error. Here, the limit strain $\bar{\varepsilon}_c$ was 0.3.

The figure shows that all the errors are decreased when the IO increased. In particular, it is shown that 11 is the optimum IO, hence that value is used in the experimental study in Section 5.5.

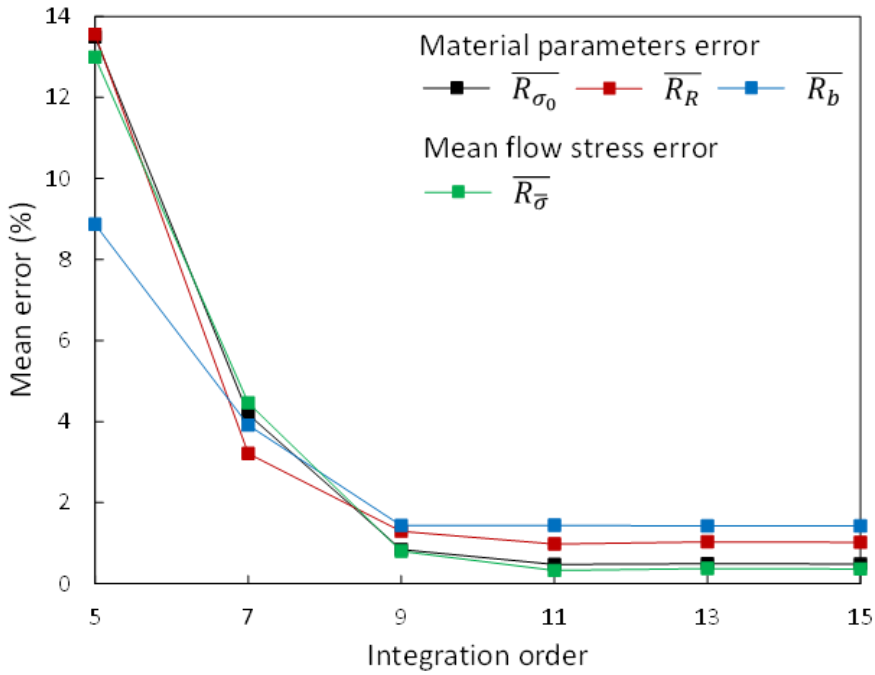

Fig. 5-11. Errors of the constitutive parameters and mean flow stresses errors depends on integration order

5.4. Materials and experiments

In the experimental study, the target material was AA6061-T6 sheets. The thickness of the sheets was 3.0 mm. Before applying FE-VFM to the friction stir welded (FSWed) materials, base material properties are measured using the tensile tests. Fig. 5-12(a) shows the engineering stress-strain curve of the target base materials. ASTM E8 standard specimen was used in the tensile tests, and the tests were performed in quasi-static condition, strain rate of 0.001/s. Strain hardening was described with Swift law in Eq. (5.12).

$$\bar{\sigma} = K\left(\bar{\varepsilon} + e_0\right)^n \tag{5.8}$$

where K, e_0, and n are material parameters. Fig. 5-12(b) shows the fitted strain hardening curves using tensile tests data. Values of the material parameters are listed in Table 5-3.

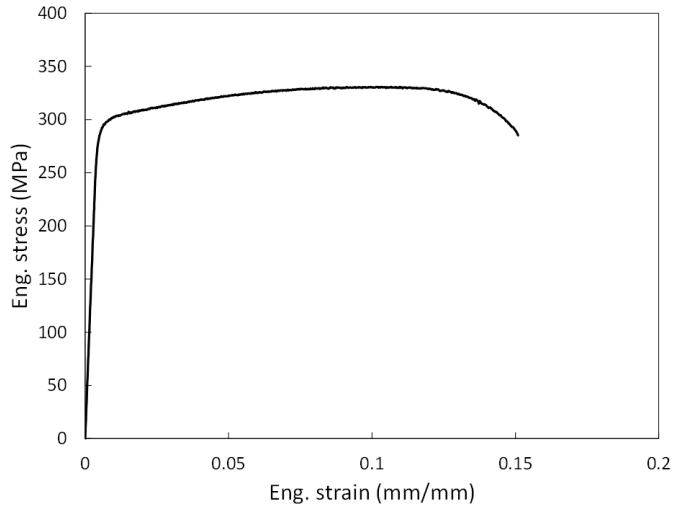

(a)

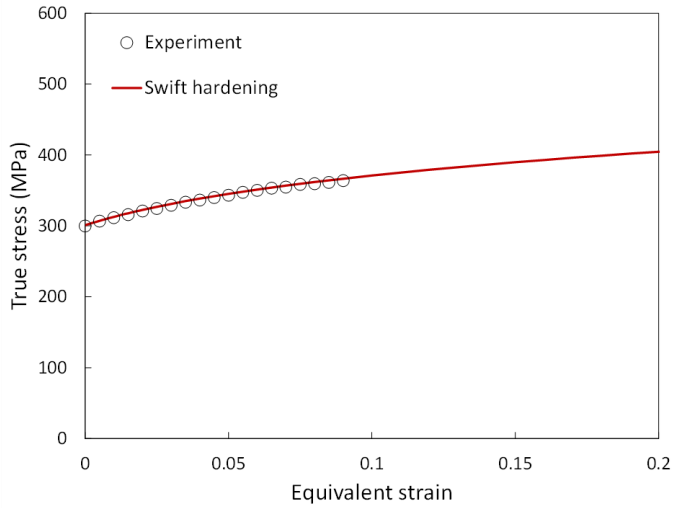

(b)

Fig. 5-12. Material properties of AA6061-T6 base material sheets. (a) Engineering stress-strain curve, and (b) flow stresses curves fitted with Swift hardening law

Table 5-3. Material parameters of AA6061-T6 sheets

Elastic constants		Swift law parameters		
E (GPa)	ν	K (MPa)	e_0 (MPa)	n
70	0.33	508.1	0.03602	0.1577

In the friction stir welding, two rectangular workpieces with the dimensions of 150 x 300 mm were welded, and 300 x 300 mm welded flat sheets were made. FSW tool geometry is schematically shown in Fig. 5-13. FSW conditions were as follows. Welding speed was 500 mm/min, and the FSW tool was tilted towards the welding direction with an angle of 3˚. For comparative study, two tool rotating speeds of 1200 and 1600 RPM were used.

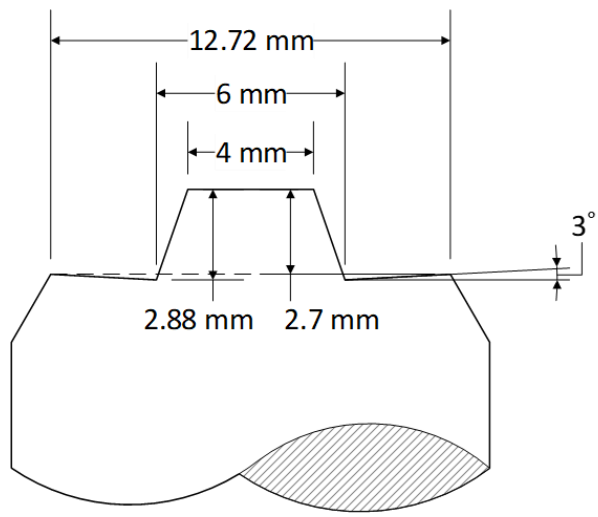

Fig. 5-13. FSW tool geometry

For applying FE-VFM, the specimen in Fig. 5-3(a) was used as the same as the feasibility tests. Meanwhile, a furrow was made in the center of the welded workpiece due to mechanical deformation during the FSW. To remove

this furrow, the top surface of the FSWed specimen is trimmed to a smooth and flat surface as shown in Fig.5-14. The total number of time steps for 1200 RPM and 1600 RPM cases were 258 and 230, respectively. The thickness was reduced owing to the trimming, from the thickness of the original sheet of 3 mm to 2.4 mm. This trimming was done via W-EDM.

An experimental study was conducted with the validated FE-VFM approaches through the feasibility in Section 5.3. Details of the FE-VFM approach for identifying nonhomogeneous strain hardening are explained in Section 5.2.

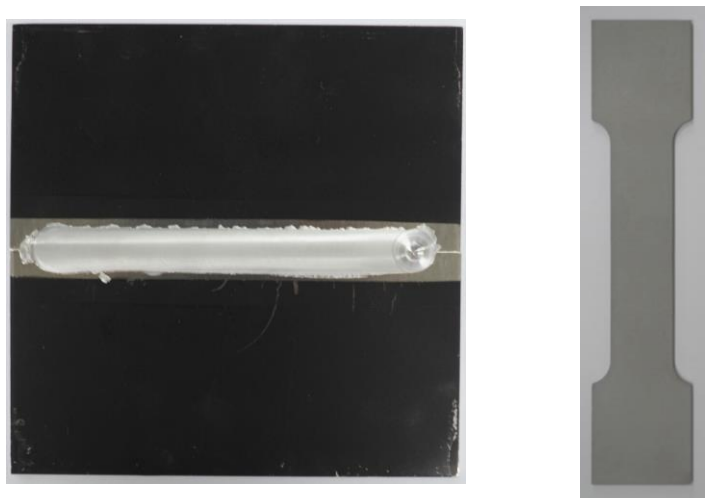

(a) (b)

Fig. 5-14. Trimming of the surface for the friction stir welded sheets in the specimen preparation. (a) Furrow at the center of the welded materials and (b) surface trimmed tensile specimen for FE-VFM

5.5. Results and validations

Figs. 5-15 and 5-16 show the strains and displacements field for the 1200 RPM and 1600 RMP cases, respectively. Both figures were illustrated at the time step of 200. Also, both figures show similar displacements and strains distributions. In particular, larger strains near the center of the specimen are shown in the figures, which are due to the materials softening during the welding.

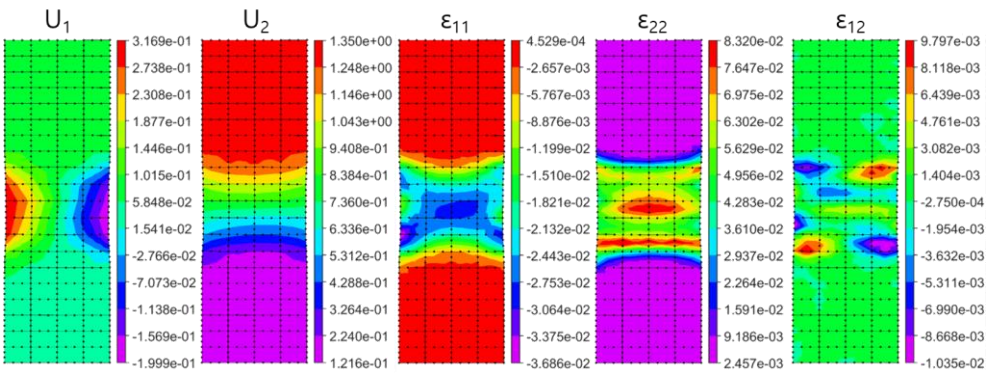

Fig. 5-15. Strains and displacements of the 1200 RPM case at time step 200.

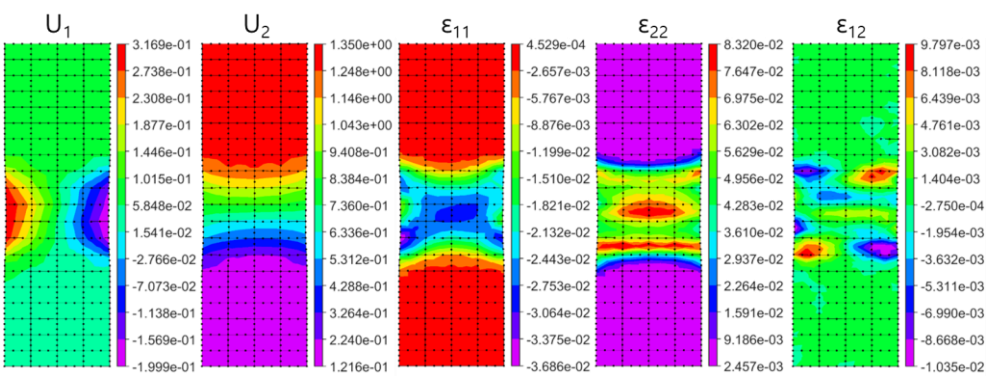

Fig. 5-16. Strains and displacements of the 1600 RPM case at time step 200.

Fig. 5-17 present the VW residuals calculated in STEP1. Fig 5-17(a) and (b) corresponds to the case of 1200 RPM and 1600 RPM, respectively. For 1200 RPM, relatively large VW residuals were calculated from -12 to 9 mm, and that range was assumed as the WAZ. On the other hand, 1600 RPM showed larger WAZ compared to 1200 RPM, from -12 to 12 mm. These results can be explained as follows. Frictional heat generated during the FSW depends on the relative speed of the tool between workpieces. The lower rotation speed generates lower heat. In particular, heat generated in the RS is less than that of AS, since the direction of tool rotation is opposite to the welding direction. Two rotation speeds—1200 and 1600 RPM—were not a huge difference in terms of heat generation in the AS, and a similar area of the HAZ was made in the AS. However, the effect of rotation speed was much larger on the RS, due to the lower relative speed compared to the AS, and the HAZ in the RS was narrower in the 1200 RPM.

Fig. 5-18 shows the normalized parameter distributions in the WAZ identified by FE-VFM, and Fig. 5-19 shows VW residuals after the parameters optimization. Detailed normalized parameters at the interpolation nodes are listed in Tables 5-4 and 5-5 for 1200 and 1600 RPM cases, respectively. Though the VW residuals were larger than that of feasibility tests, the figure indicates that non-linear optimization was well-performed. Similar to Fig. 5-17, Fig. 5-18(a) and (b) are 1200 and 1600 RPM cases, respectively. Both 1200 and 1600 RPM shows a similar pattern except for the width of the

WAZ on the RS. The values of the parameter K for the Swift law were close to 1, and it indicates that the values of the K were overall similar to that of base materials. (Since the values plotted in Fig. 5-18 are normalized parameters by the base material parameters) On the other hand, distributions of the parameter n vary much from the base materials. In the range of -6 to 6 mm, values of n are twice the base materials, and it decreases when the materials are far from the weld line. Also, it is shown that the value of e_0 is significantly smaller near the ±6 mm.

The parameters of the Swift law have a physical meaning. The parameter K indicates the general strength of the materials. The parameter n is related to the uniform elongation (U-EL) in tensile tests. Lastly, the parameter e_0 is related to the yield stress. Hence, the distributions of parameters are closely related to the change of the material properties due to the welding. Therefore, distributions of the Swift law parameters can provide information on the changes in the material properties, especially in terms of yield strength and ductility.

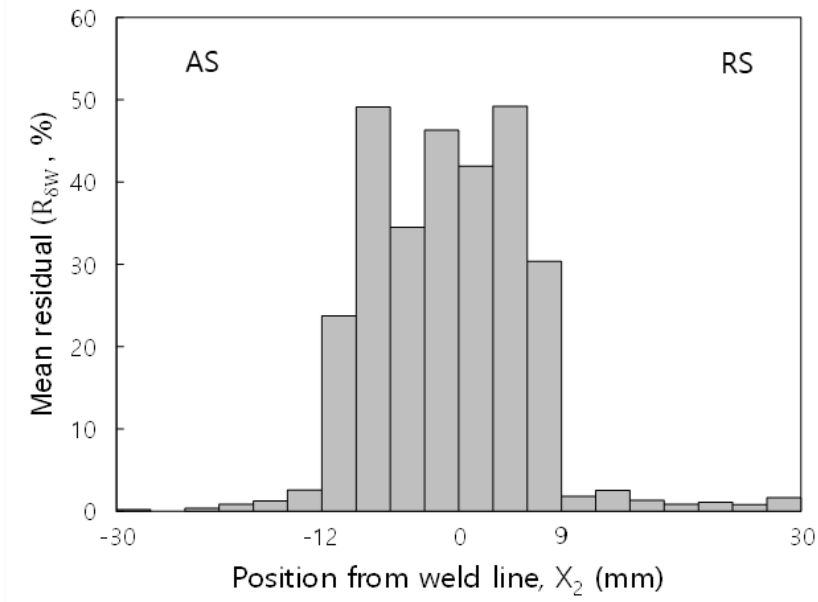

(a)

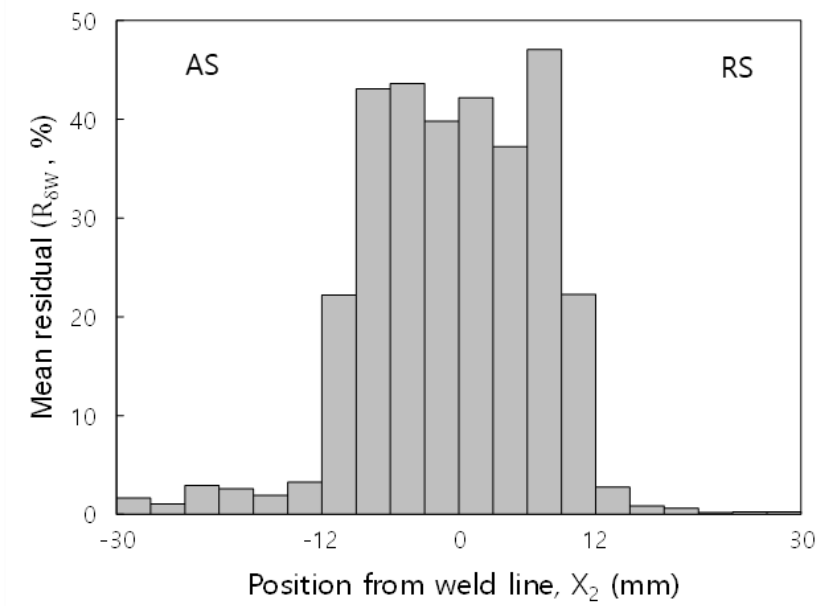

(b)

Fig. 5-17. VW residuals for each subdomain.

(a) 1200 RPM, and (b) 1600RPM

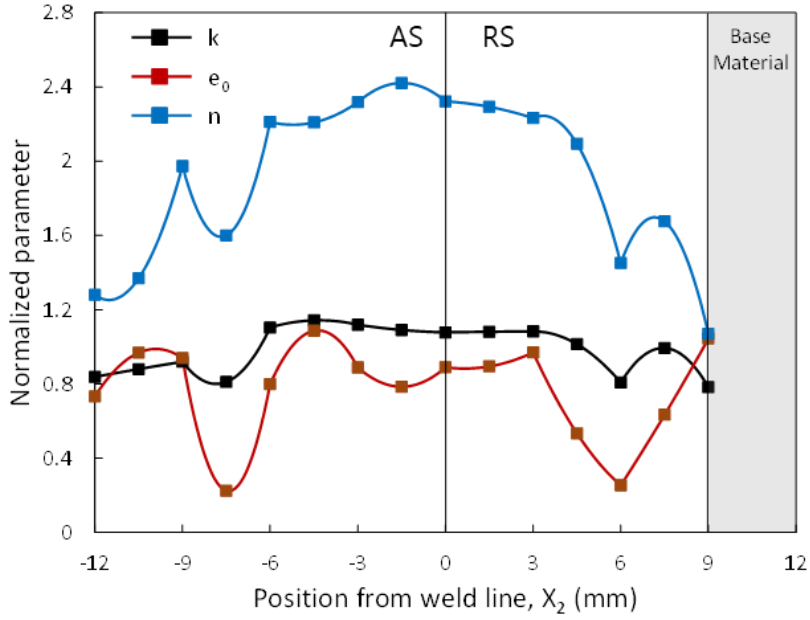

(a)

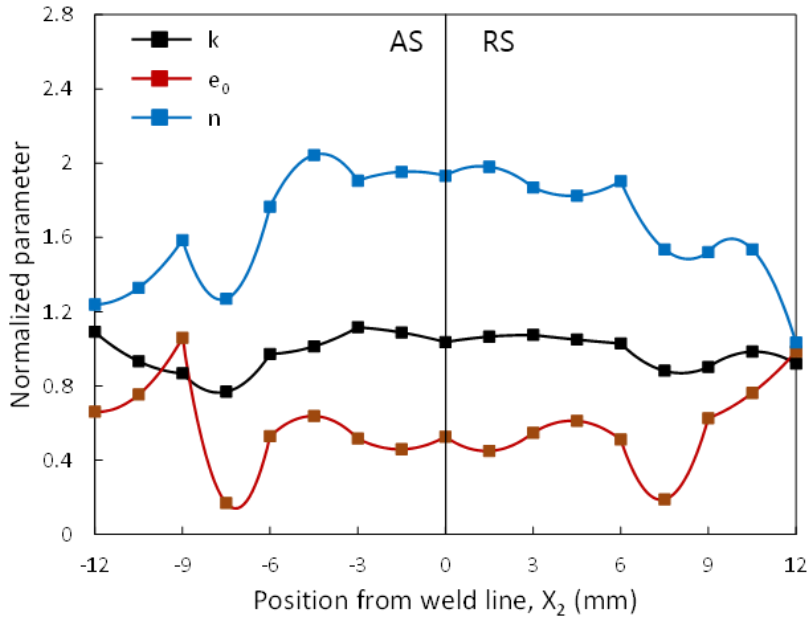

(b)

Fig. 5-18. Normalized parameter distributions of Swift hardening law measured by FE-VFM. (a) 1200 RPM, and (b) 1600 RPM.

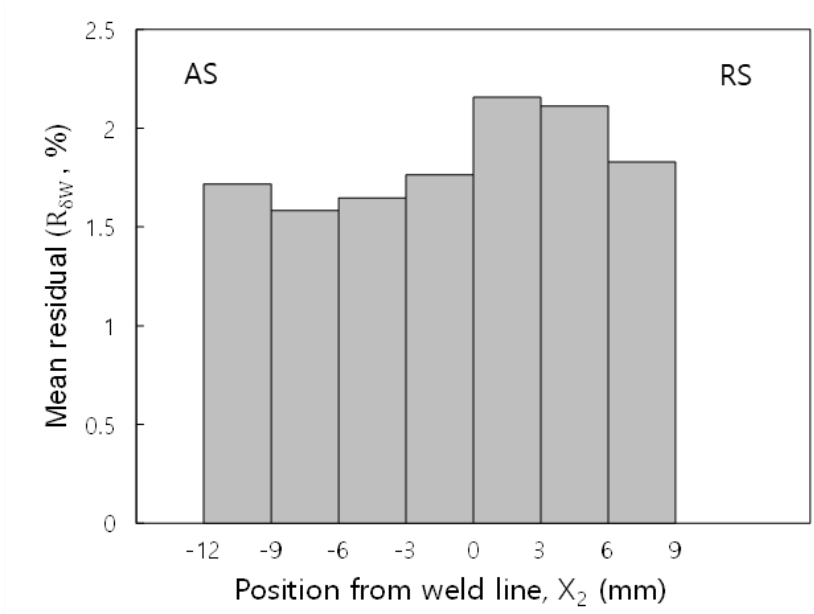

(a)

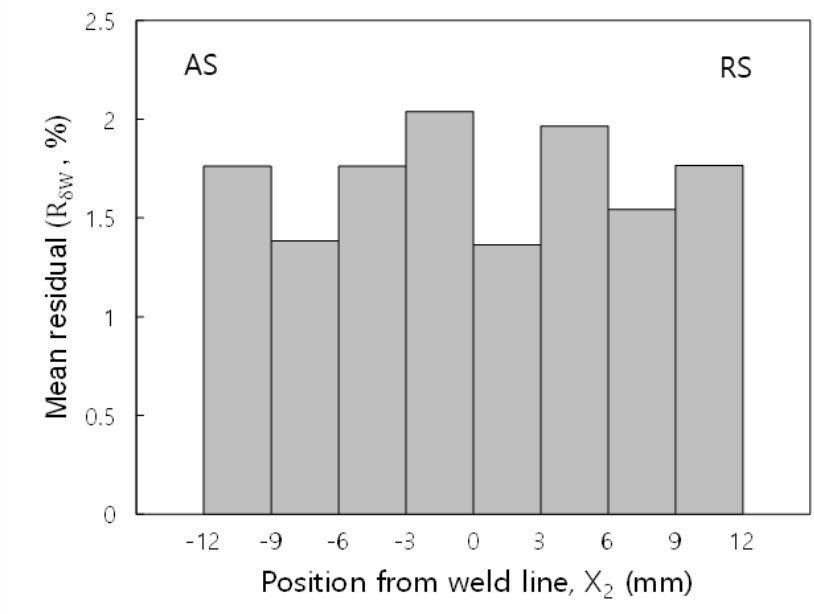

(b)

Fig. 5-19. VW residuals after constitutive parameter optimization. (a) 1200 RPM, and (b) 1600 RPM

Table 5-4. Identified nodal normalized parameters for 1200 RPM.

Position (mm)	Normalized parameters		
	k	e_0	n
-12.0	0.8383	0.7327	1.2800
-10.5	0.8800	0.9687	1.3695
-9.0	0.9197	0.9401	1.9733
-7.5	0.8107	0.2248	1.5999
-6.0	1.1038	0.7994	2.2117
-4.5	1.1424	1.0868	2.2093
-3.0	1.1187	0.8897	2.3176
-1.5	1.0908	0.7854	2.4215
0	1.0777	0.8902	2.3224
1.5	1.0809	0.8946	2.2932
3.0	1.0829	0.9702	2.2324
4.5	1.0145	0.5340	2.0937
6.0	0.8074	0.2541	1.4521
7.5	0.9933	0.6342	1.6761
9.0	0.7820	1.0451	1.0700

Table 5-5. Identified nodal normalized parameters for 1600 RPM.

Position (mm)	Normalized parameters		
	k	e_0	n
-12.0	1.0912	0.6617	1.2383
-10.5	0.9334	0.7536	1.3290
-9.0	0.8677	1.0592	1.5853
-7.5	0.7690	0.1684	1.2695
-6.0	0.9726	0.5284	1.7661
-4.5	1.0136	0.6378	2.0444
-3.0	1.1163	0.5168	1.9059
-1.5	1.0883	0.4590	1.9536
0	1.0364	0.5270	1.9323
1.5	1.0661	0.4500	1.9807
3.0	1.0748	0.5483	1.8687
4.5	1.0501	0.6117	1.8254
6.0	1.0292	0.5109	1.9034
7.5	0.8816	0.1889	1.5359
9.0	0.9019	0.6263	1.5204
10.5	0.9848	0.7625	1.5356
12.0	0.9200	0.9854	1.0342

These can be more clearly interpreted using Figs. 5-20 and 5-21. Fig. 5-20 shows the theoretical U-EL calculated with considerè condition. For the Swift law, theoretical U-El is given as (n-e_0). Fig. 21 shows that the U-EL is increased in the -6 to 6 mm range, and that range corresponds to the width of the FSW tool in Fig. 5-13. Then, the U-El decreases if the materials are far from the weld line. In other words, ductility in the SZ increased due to the welding, and it continuously decreased in the HAZ to the similar values of the base materials. Note that the U-EL presented in Fig. 5-20 is only the theoretical values based on the Siwft law, hence it can give a general tendency only, and other factors can affect the real U-EL such as anisotropy. (Which is not considered in this study)

Fig. 5-21 illustrates the distributions of normalized yield stresses. For the comparison, Vickers hardness distributions were measured, and normalized hardnesses were illustrated in Fig. 5-21 together. (Hardness of the base materials was 112 HV) Though normalized yields and normalized hardnesses show a similar tendency, the absolute magnitude of the two values shows a considerable difference. It can be analyzed as two-fold. First, it validates that the nonhomogeneous material properties were accurately measured with the FE-VFM. Second, hardness cannot be a material property in a strict sense, and it only represents the tendency of the difference in material properties.

Meanwhile, the yield stresses in the -6 to 6 mm range decreased compared to base materials, and it increased to a similar level of the base materials

outside of the width of the FSW tool. This is just the opposite trend to the U-EL. Also, the lowest yields were shown at the edge of the FSW tool (near the -7.5 and 7.5 mm positions) for both 1200 and 1600 RPM. Normalized hardness also shows minimum values at the same point, similarly. In other words, the materials at these positions yield before the other region, and the ductility is smaller compared to the SZ (-6 to 6 mm range). Thus, materials at these locations can be the weakest points in the forming process.

Tensile tests with a specimen in Fig. 5-22(a) were performed for the validation of the FE-VFM results. Displacements were measured using a virtual extensometer in the DIC postprocessing, and the gauge length of the virtual extensometer was 40 mm. Then, FE simulations were conducted with the material properties measured by FE-VFM, in the same conditions of the validation tensile tests. Fig. 5-22(b) illustrate the 3D half symmetric model used in the simulation. In Fig.5-22(c) load-displacements are compared for both simulations and experiments. Both 1200 and 1600 RPM cases show that the predicted load-displacement curves are in good agreement with experiments. Hence, it indicates that the proposed FE-VFM approach can accurately measure the nonhomogeneous strain hardening in the WAZ.

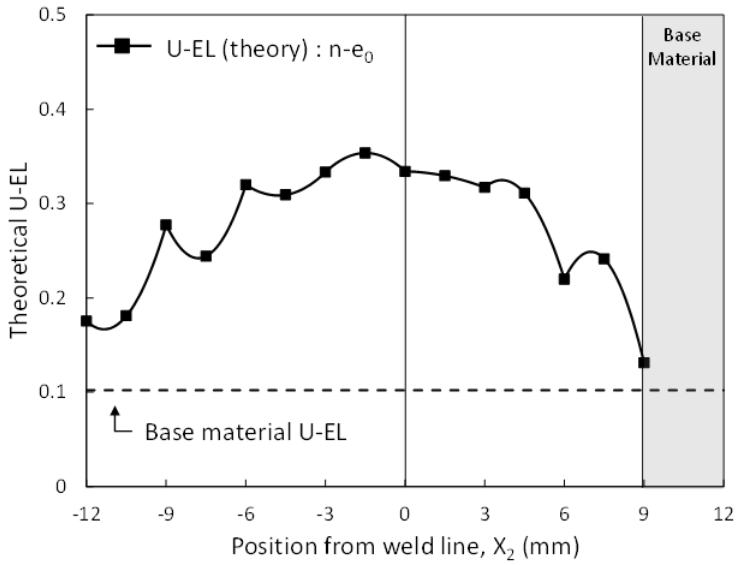

(a)

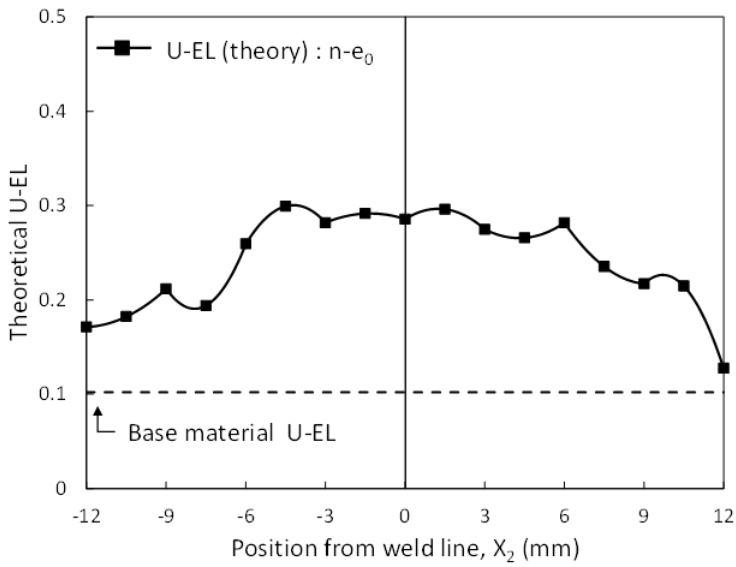

(b)

Fig. 5-20. Theoretical uniform elongation distributions measured by FE-VFM. (a) 1200 RPM, and (b) 1600 RPM.

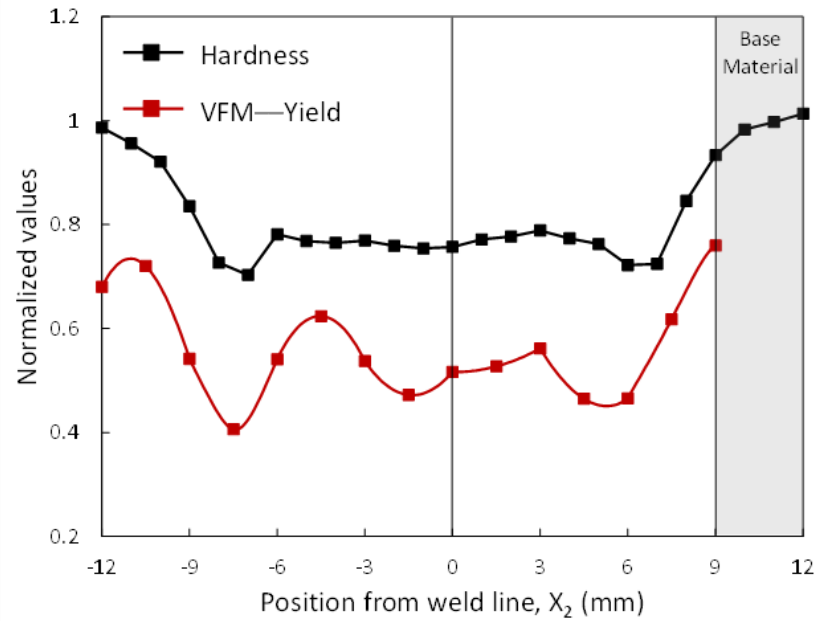

(a)

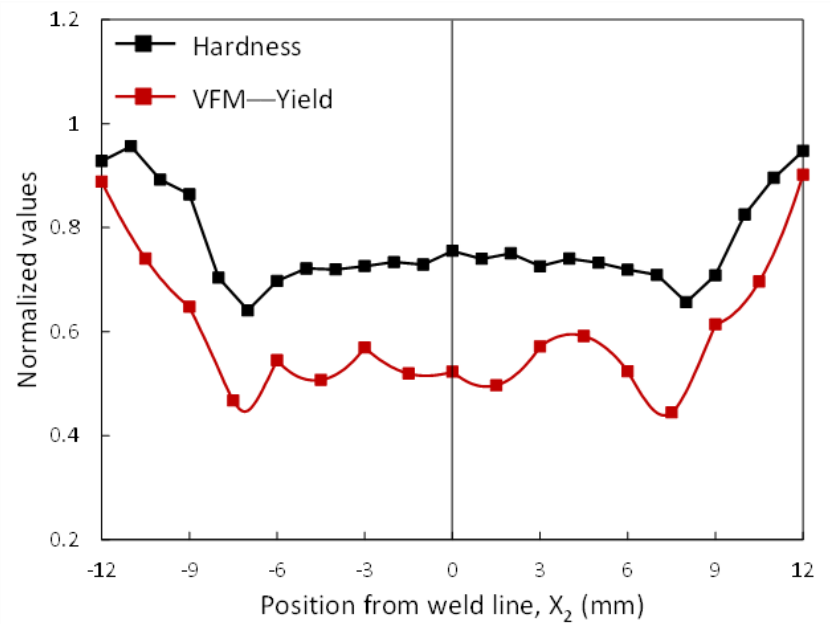

(b)

Fig. 5-21. Comparison of normalized yield stresses measured by FE-VFM. (a) 1200 RPM, and (b) 1600RPM.

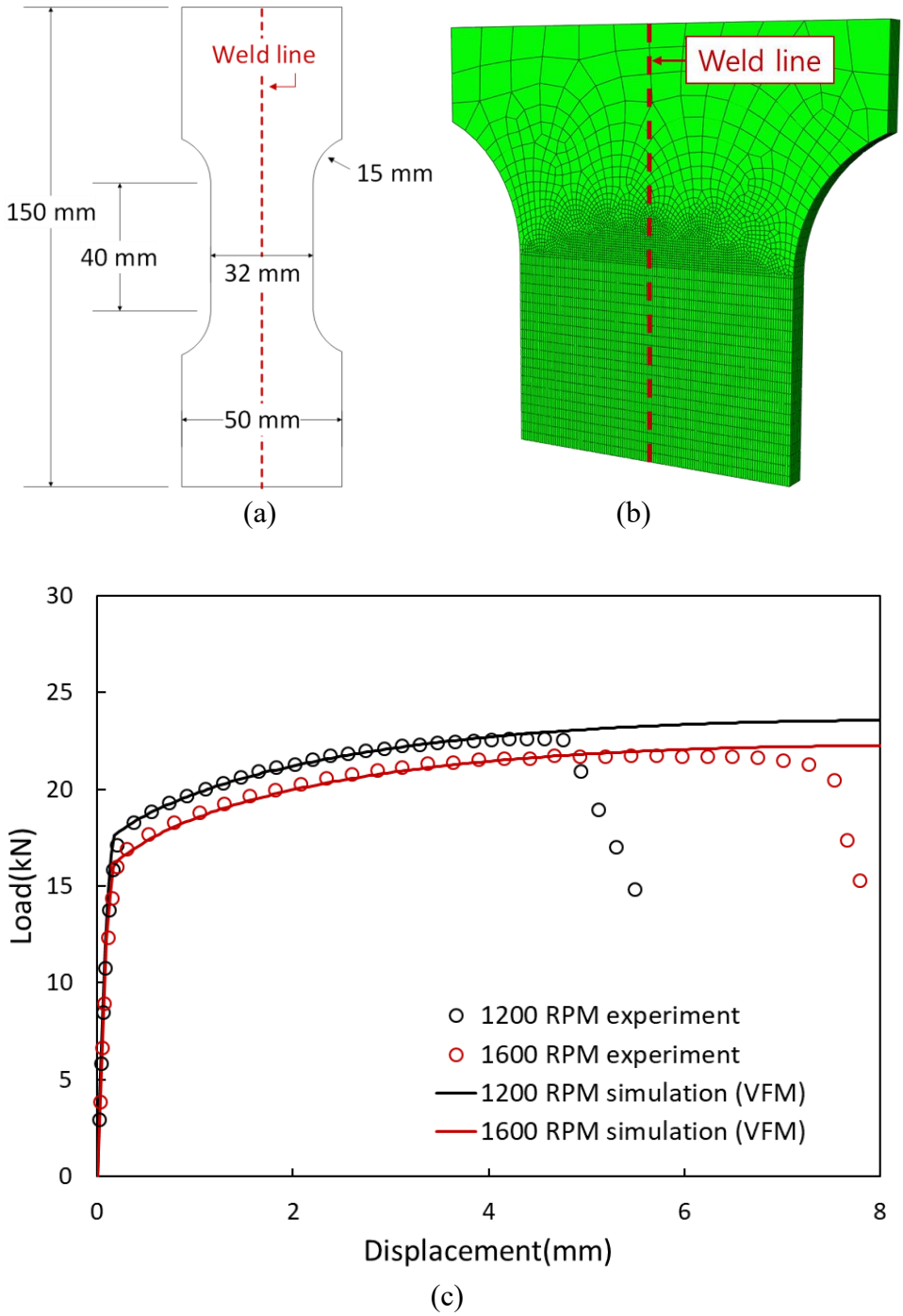

Fig. 5-22. Validation of obtained local flow stresses. (a) tests specimen geometry, (b) 3D half FE model, and (c) comparison of predicted load-displacement curves with experiments

5.6. Summary

The FE-VFM was applied for identifying nonhomogeneous strain hardening of the friction stir welded aluminum alloy sheets, as an advanced application. A two-step identification procedure is introduced. First, weld affected zone boundary was identified (STEP1), then, local flow stresses were identified in the WAZ (STEP2). In addition, the area of interest was divided into subdomains, and FE-VFM was applied to each subdomain independently. Also, material constants in each subdomain are interpolated with a quadratic function. To uniquely identify the interpolated material parameters, normal distribution type virtual fields were used. These numerical approaches were is validated through feasibility tests based on FE simulation data. Feasibility tests demonstrated that the boundary of the WAZ and the non-homogeneous strain hardening could be successfully identified using FE-VFM owing to the virtual fields defined with a normal distribution function and higher-order Gauss quadrature.

The validated method was applied to identify the local flow stresses of the friction stir welded AA6061-T6 sheets for two different FSW conditions, which were tool rotation speeds of 1200 RPM and 1600 RPM cases. In STEP1, the WAZ of the 1200 and 1600 RPM cases were identified as -9 to 12 mm and -12 to 12 mm from the weld line, respectively. Followed by STEP1, the distribution of the parameters was identified as STEP2 using FE-VFM. The results of the FE-VFM showed that the strength in the WAZ was weakened

due to the welding, whereas the ductility of the aluminum alloys was increased in the WAZ. Finally, FE simulations were conducted with identified non-homogeneous strain hardening, to validate the identified results. The predictions using FE-VFM results were in good agreement with experiments, and this confirms that the FE-VFM can accurately identify the non-homogeneous strain hardening distributions for the welded aluminum alloys.

6. Conclusions

In this study, a novel virtual fields method (VFM) based on the finite element (FE) scheme, namely FE-VFM, is proposed as an inverse method for identifying the parameters of constitutive models. In the FE-VFM, experimentally measured full-field displacements are mapped onto FE meshes using global and local shape functions, and the internal virtual work is integrated using the Gauss quadrature rule.

Extensive sensitivity tests for the validation of the proposed FE-VFM were performed with ideal deformation fields generated by finite element simulations for both orthotropic linear elastic and isotropic elastic-plastic cases. FE-VFM conditions tested in this study were (1) FE mesh size from 1 mm to 5mm, (2) FE order from linear to cubic elements, and (3) Gauss quadrature order from 1 to 3. The sensitivity study showed that the element size and order of the shape function had a minor effect on the quality of the VFM for the elastic material. The virtual fields selection, rather than the FE meshes, critically affects the quality of the results. Moreover, a higher-order Gauss quadrature improves the accuracy of calculating the IVW when complex virtual fields are used. In the case of elastic-plastic material, the element size and the order of an element, and the order of the Gauss quadrature had a considerable effect on the accuracy of the identified material parameters, which resulted from the spatial non-linearity of the large plastic

deformation. It was also shown by validation that even coarse FE meshes could give satisfactory accuracy in the FE-VFM when higher order elements and Gauss quadrature were adopted.

As an applications of the FE-VFM, homogeneous and nonhomogeneous strain hardening of the metal sheets were identified. New virtual fields based on real nodal displacements were proposed to improve the accuracy of VFM at large plastic deformation. This approach was named pseudo-real deformation fields in this study to highlight the use of varying real deformation fields. FE-VFM is applied for the identification of plastic hardening in 1470 MPa PHS sheets with the PDF. In the FE-VFM, notched tensile test data was used, and obtained strain hardening is validated using U-notch tensile tests. The U-notch tension load–displacement curve predicted using the FE-VFM hardening parameters showed better agreement with the experimental results than did the conventional fitting-based hardening parameters. The improved accuracy relative to the conventional method is explained as follows. First, the commonly adopted 0.2% offset method for determining yield stress ignores the transition from elastic to plastic yielding. In this case, the conventionally determined yield stress may be overestimated, while the FE-VFM reflects the transition behavior near the yield. Second, the simple tension-based fitting to a prescribed hardening law is only valid before uniform elongation because the deformation becomes non-uniform beyond this point. The investigated PHS had a low uniform elongation (only 5%),

which led to a discrepancy in the predicted deformation at large strain for the U-notched tension. However, in the case of the FE-VFM, stress-strain data in a large plastic strain range can be utilized for identification, which resulted in better identification accuracy for plastic hardening.

As an advanced application, the FE-VFM was applied for identifying nonhomogeneous strain hardening of the friction stir welded aluminum alloy sheets, as an advanced application of the FE-VFM. In this study, weld affected zone boundary was identified, then, local flow stresses were identified in the WAZ. In addition, the area of interest was divided into subdomains, and FE-VFM was applied to each subdomain independently. Also, material constants in each subdomain are interpolated with a quadratic function. To uniquely identify the interpolated material parameters, normal distribution type virtual fields were used. These numerical approaches were is validated through feasibility tests based on FE simulation data. Feasibility tests show that constitutive parameters interpolated with piecewise polynomials within a subdomain cannot be uniquely identified using conventional polynomial virtual fields, however, three independent virtual fields defined with normal distribution functions—that enhance different local data within a subdomain—show a good capability to identify the interpolated constitutive parameters. Also, higher-order Gauss quadrature was required due to the large non-linearity originated from the constitutive parameter interpolation and normal distribution type virtual fields.

Then, the validated method was applied to identify the local flow stresses of the friction stir welded AA6061-T6 sheets with two different tool rotation speeds of 1200 and 1600 RPM. Identified WAZs were -9 to 12 mm and -12 to 12 mm for 1200 and 1600 RPM cases, respectively. Also, identified non-homogeneous strain hardening in the WAZ showed that the strength of the aluminum alloy sheets in the WAZ was decreased, whereas the ductility was increased. Finally, validation tensile tests were conducted with a loading direction parallel to the weld line, and FE simulations were conducted to validate the FE-VFM results. The predicted load-displacement curves of the FE simulations showed a good match with experiments, and it confirms that FE-VFM can accurately identify the non-homogeneous material properties due to the welding.

Overall, numerical sensitivity tests and real applications with experiments validate that the proposed FE-VFM can be effective and accurate for characterizing the material properties. In particular, the FE-VFM can be used to identify the plastic properties of the metal sheets, especially the properties that are hardly obtainable with conventional mechanical tests.

Reference

[1] ASTM international, ASTM D3039D3039M Standard Test Method for Tensile Properties of Polymer Matrix Composite Materials, (n.d.).

[2] ASTM International, ASTM E8/E8M -13A Standard Test Methods for Tension Testing of Metallic Materials, n.d.

[3] H. Choi, S. Choi, S.-C. Kang, C. Kim, M.-G. Lee, Prediction of anisotropic strengths of steel plate after prior bending-reverse bending deformation: Application of distortional hardening model, International Journal of Mechanical Sciences. 204 (2021) 106512-undefined.

[4] C. Kim, K.M. Min, H. Choi, H.J. Kim, M.-G. Lee, Development of analytical strength estimator for self-piercing rivet joints through observation of finite element simulations, International Journal of Mechanical Sciences. 202–203 (2021) 106499-undefined.

[5] R. Hill, A theory of the yielding and plastic flow of anisotropic metals, Proceedings of the Royal Society of London. Series A. Mathematical and Physical Sciences. 193 (1948).

[6] H. Choi, S. Choi, S.-C. Kang, C. Kim, M.-G. Lee, Prediction of anisotropic strengths of steel plate after prior bending-reverse bending deformation: Application of distortional hardening model, International Journal of Mechanical Sciences. 204 (2021).

[7] F. Barlat, H. Aretz, J.W. Yoon, M.E. Karabin, J.C. Brem, R.E. Dick, Linear transfomation-based anisotropic yield functions, International Journal of Plasticity. 21 (2005).

[8] G. Marckmann, G. Chagnon, M. le Saux, P. Charrier, Experimental investigation and theoretical modelling of induced anisotropy during stress-softening of rubber, International Journal of Solids and Structures. 97–98 (2016).

[9] N. Tardif, S. Kyriakides, Determination of anisotropy and material hardening for aluminum sheet metal, International Journal of Solids and Structures. 49 (2012).

[10] B. Tang, Y. Lou, Effect of Anisotropic Yield Functions on the Accuracy of Material Flow and its Experimental Verification, Acta Mechanica Solida Sinica. 32 (2019) 50–68.

[11] R.M. Jones, Mechanics of Composite Materials, 2nd Edition, CRC Press, 2018.

[12] Q. Yin, C. Soyarslan, K. Isik, A.E. Tekkaya, A grooved in-plane torsion test for the investigation of shear fracture in sheet materials, International Journal of Solids and Structures. 66 (2015) 121–132.

[13] Q. Yin, B. Zillmann, S. Suttner, G. Gerstein, M. Biasutti, A.E. Tekkaya, M.F.X. Wagner, M. Merklein, M. Schaper, T. Halle, A. Brosius, An experimental and numerical investigation of different shear test configurations for sheet metal characterization, International Journal of Solids and Structures. 51 (2014) 1066–1074.

[14] S. Suttner, M. Merklein, Experimental and numerical investigation of a strain rate controlled hydraulic bulge test of sheet metal, Journal of Materials Processing Technology. 235 (2016).

[15] S. Kim, J. Lee, F. Barlat, M.-G. Lee, Formability prediction of advanced high strength steels using constitutive models characterized by uniaxial and biaxial experiments, Journal of Materials Processing Technology. 213 (2013).

[16] M. Grédiac, The use of full-field measurement methods in composite material characterization: interest and limitations, Composites Part A: Applied Science and Manufacturing. 35 (2004).

[17] K.A. Stetson, A Review of Speckle Photography and Interferometry, Optical Engineering. 14 (1975).

[18] R.S. Sirohi, Speckle Metrology: Some Newer Techniques and Applications, in: Springer Series in OPTICAL SCIENCES Book Series, 1999.

[19] Y. Surrel, Moiré and grid methods: a signal-processing approach, Interferometry'94: Photomechanics, Nternational Society for Optics and Photonics. 2342 (1994).

[20] J.-L. Piro, M. Grediac, Producing and transfering low-spatial-frequency grids for measuring displacement fields with moiré and grid methods, Experimental Techniques. 28 (2004).

[21] D. Post, B. Han, P. Ifju, Moiré Interferometry, in: Mechanical Engineering Series Book Series , 1994.

[22] B. Han, D. Post, P. Ifju, Moiré interferometry for engineering mechanics: Current practices and future developments, The Journal of Strain Analysis for Engineering Design. 36 (2001).

[23] J.N. Petzing, J.R. Tyrer, Recent developments and applications in electronic speckle pattern interferometry, The Journal of Strain Analysis for Engineering Design. 33 (1998).

[24] O.J. Løkberg, Electronic Speckle Pattern Interferometry, in: Optical Metrology, Springer Netherlands, Dordrecht, 1987.

[25] M. Sutton, W. Wolters, W. Peters, W. Ranson, S. McNeill, Determination of displacements using an improved digital correlation method, Image and Vision Computing. 1 (1983) 133–139.

[26] T.C. Chu, W.F. Ranson, M.A. Sutton, Applications of digital-image-correlation techniques to experimental mechanics, Experimental Mechanics. 25 (1985) 232–244.

[27] H. Schreier, J.-J. Orteu, M.A. Sutton, Image Correlation for Shape, Motion and Deformation Measurements, Springer US, Boston, MA, 2009.

[28] R. Bigger, B. Blaysat, C. Boo, M. Grewer, J. Hu, A. Jones, M. Klein, K. Raghavan, P. Reu, T. Schmidt, T. Siebert, M. Simenson, D. Turner, A. Vieira, T. Weikert, A Good Practices Guide for Digital Image Correlation, 2018.

[29] X. Xu, Y. Su, Y. Cai, T. Cheng, Q. Zhang, Effects of Various Shape Functions and Subset Size in Local Deformation Measurements Using DIC, Experimental Mechanics. 55 (2015).

[30] S. Avril, M. Bonnet, A.-S. Bretelle, M. Grédiac, F. Hild, P. Ienny, F. Latourte, D. Lemosse, S. Pagano, E. Pagnacco, F. Pierron, Overview of Identification Methods of Mechanical Parameters Based on Full-field Measurements, Experimental Mechanics. 48 (2008) 381–402.

[31] F. Pierron, M. Grédiac, The Virtual Fields Method, Springer New York, New York, NY, 2012.

[32] M. Grédiac, F. Pierron, S. Avril, E. Toussaint, The Virtual Fields Method for Extracting Constitutive Parameters From Full-Field Measurements: a Review, Strain. 42 (2008) 233–253.

[33] T. He, L. Liu, A. Makeev, Uncertainty analysis in composite material properties characterization using digital image correlation and finite element model updating, Composite Structures. 184 (2018) 337–351.

[34] J. Aquino, A.G. Andrade-Campos, J.M.P. Martins, S. Thuillier, Design of heterogeneous mechanical tests: Numerical methodology and experimental validation, Strain. 55 (2019) e12313-.

[35] G. Lubineau, A goal-oriented field measurement filtering technique for the identification of material model parameters, Computational Mechanics. 44 (2009) 591–603.

[36] Z. Ktari, C. Leitão, P.A. Prates, A. Khalfallah, Mechanical design of ring tensile specimen via surrogate modelling for inverse material parameter identification, Mechanics of Materials. 153 (2021) 103673-.

[37] E. Florentin, G. Lubineau, Using constitutive equation gap method for identification of elastic material parameters: technical insights and illustrations, International Journal on Interactive Design and Manufacturing (IJIDeM). 5 (2011) 227–234.

[38] E. Florentin, G. Lubineau, Identification of the parameters of an elastic material model using the constitutive equation gap method, Computational Mechanics. 46 (2010) 521–531.

[39] D. Claire, F. Hild, S. Roux, A finite element formulation to identify damage fields: the equilibrium gap method, International Journal for Numerical Methods in Engineering. 61 (2004) 189–208.

[40] L. Crouzeix, J.N. Périé, F. Collombet, B. Douchin, An orthotropic variant of the equilibrium gap method applied to the analysis of a biaxial test on a composite material, Composites Part A: Applied Science and Manufacturing. 40 (2009) 1732–1740.

[41] C. Karadogan, P. Cyron, M. Liewald, Potential use of machine learning to determine yield locus parameters, IOP Conference Series: Materials Science and Engineering. 1157 (2021) 012064-.

[42] F. Pierron, M. Grédiac, Identification of the through-thickness moduli of thick composites from whole-field measurements using the Iosipescu fixture: theory and simulations, Composites Part A: Applied Science and Manufacturing. 31 (2000) 309–318.

[43] M. Grédiac, F. Pierron, A T-shaped specimen for the direct characterization of orthotropic materials, International Journal for Numerical Methods in Engineering. 41 (1998) 293–309.

[44] C. Kim, J.-H. Kim, M.-G. Lee, A virtual fields method for identifying anisotropic elastic constants of fiber reinforced composites using a single tension test: Theory and validation, Composites Part B: Engineering. 200 (2020) 108338-undefined.

[45] N. Promma, B. Raka, M. Grédiac, E. Toussaint, J.-B. le Cam, X. Balandraud, F. Hild, Application of the virtual fields method to mechanical characterization of elastomeric materials, International Journal of Solids and Structures. 46 (2009).

[46] J.-H. Kim, S. Avril, A. Duprey, J.-P. Favre, Experimental characterization of rupture in human aortic aneurysms using a full-field measurement technique, Biomechanics and Modeling in Mechanobiology. 11 (2012) 841–853.

[47] S. Yoon, C.R. Siviour, Application of the Virtual Fields Method to a relaxation behaviour of rubbers, Journal of the Mechanics and Physics of Solids. 116 (2018) 416–431.

[48] J.-H. Kim, A. Serpantié, F. Barlat, F. Pierron, M.-G. Lee, Characterization of the post-necking strain hardening behavior using the virtual fields method, International Journal of Solids and Structures. 50 (2013).

[49] J.-H. Kim, F. Barlat, F. Pierron, M.-G. Lee, Determination of Anisotropic Plastic Constitutive Parameters Using the Virtual Fields Method, Experimental Mechanics. 54 (2014) 1189–1204.

[50] S. Avril, F. Pierron, M.A. Sutton, J. Yan, Identification of elasto-visco-plastic parameters and characterization of Lüders behavior using digital image correlation and the virtual fields method, Mechanics of Materials. 40 (2008) 729–742.

[51] D. Leem, J.-H. Kim, F. Barlat, J.H. Song, M.-G. Lee, Identification of Dynamic Flow Stress Curves Using the Virtual Fields Methods: Theoretical Feasibility Analysis, Metals and Materials International. 24 (2018) 351–361.

[52] A. Berry, O. Robin, F. Pierron, Identification of dynamic loading on a bending plate using the Virtual Fields Method, Journal of Sound and Vibration. 333 (2014) 7151–7164.

[53] Y. Su, X. Yao, S. Wang, Y. Ma, Simultaneous determination of virtual fields and material parameters for thermo-mechanical coupling deformation in orthotropic materials, Mechanics of Materials. 124 (2018) 33–44.

[54] H. Chalal, F. Meraghni, F. Pierron, M. Grédiac, Direct identification of the damage behaviour of composite materials using the virtual fields method, Composites Part A: Applied Science and Manufacturing. 35 (2004).

[55] R. Moulart, S. Avril, F. Pierron, Identification of the through-thickness rigidities of a thick laminated composite tube, Composites Part A: Applied Science and Manufacturing. 37 (2006).

[56] K. Syed-Muhammad, E. Toussaint, M. Grédiac, S. Avril, J.H. Kim, Characterization of composite plates using the virtual fields method with optimized loading conditions, Composite Structures. 85 (2008).

[57] J.-H. Kim, F. Pierron, M.R. Wisnom, K. Syed-Muhamad, Identification of the local stiffness reduction of a damaged composite plate using the virtual fields method, Composites Part A: Applied Science and Manufacturing. 38 (2007) 2065–2075.

[58] M. Rossi, F. Pierron, M. Štamborská, Application of the virtual fields method to large strain anisotropic plasticity, International Journal of Solids and Structures. 97–98 (2016) 322–335.

[59] J.-H. Kim, F. Barlat, F. Pierron, M.-G. Lee, Determination of Anisotropic Plastic Constitutive Parameters Using the Virtual Fields Method, Experimental Mechanics. 54 (2014) 1189–1204.

[60] J.M.P. Martins, A. Andrade-Campos, S. Thuillier, Calibration of anisotropic plasticity models using a biaxial test and the virtual fields method, International Journal of Solids and Structures. 172–173 (2019).

[61] M. Grédiac, E. Toussaint, F. Pierron, Special virtual fields for the direct determination of material parameters with the virtual fields method. 1— Principle and definition, International Journal of Solids and Structures. 39 (2002) 2691–2705.

[62] M. Grédiac, E. Toussaint, F. Pierron, Special virtual fields for the direct determination of material parameters with the virtual fields method. 2—Application to in-plane properties, International Journal of Solids and Structures. 39 (2002) 2707–2730.

[63] M. Grédiac, E. Toussaint, F. Pierron, Special virtual fields for the direct determination of material parameters with the virtual fields method. 3. Application to the bending rigidities of anisotropic plates, International Journal of Solids and Structures. 40 (2003) 2401–2419.

[64] E. Toussaint, M. Grédiac, F. Pierron, The virtual fields method with piecewise virtual fields, International Journal of Mechanical Sciences. 48 (2006).

[65] A. Marek, F.M. Davis, F. Pierron, Sensitivity-based virtual fields for the non-linear virtual fields method, Computational Mechanics. 60 (2017) 409–431.

[66] A. Marek, F.M. Davis, M. Rossi, F. Pierron, Extension of the sensitivity-based virtual fields to large deformation anisotropic plasticity, International Journal of Material Forming. 12 (2019) 457–476.

[67] A. Marek, F.M. Davis, J.-H. Kim, F. Pierron, Experimental Validation of the Sensitivity-Based Virtual Fields for Identification of Anisotropic Plasticity Models, Experimental Mechanics. 60 (2020) 639–664.

[68] M. Rossi, F. Pierron, Identification of plastic constitutive parameters at large deformations from three dimensional displacement fields, Computational Mechanics. 49 (2012) 53–71.

[69] A. Buljac, C. Jailin, A. Mendoza, J. Neggers, T. Taillandier-Thomas, A. Bouterf, B. Smaniotto, F. Hild, S. Roux, Digital Volume Correlation: Review of Progress and Challenges, Experimental Mechanics. 58 (2018) 661–708.

[70] S. Avril, J.M. Huntley, F. Pierron, D.D. Steele, 3D Heterogeneous Stiffness Reconstruction Using MRI and the Virtual Fields Method, Experimental Mechanics. 48 (2008) 479–494.

[71] F. Meng, X. Zhang, J. Wang, C. Li, J. Chen, C. Sun, 3D Strain and Elasticity Measurement of Layered Biomaterials by Optical Coherence Elastography based on Digital Volume Correlation and Virtual Fields Method, Applied Sciences. 9 (2019).

[72] M. Rossi, P. Lava, F. Pierron, D. Debruyne, M. Sasso, Effect of DIC spatial resolution, noise and interpolation error on identification results with the VFM, Strain. 51 (2015) 206–222.

[73] K. Chung, M.-G. Lee, Basics of Continuum Plasticity, Springer Singapore, Singapore, 2018.

[74] F. Barlat, J. Ha, J.J. Grácio, M.G. Lee, E.F. Rauch, G. Vincze, Extension of homogeneous anisotropic hardening model to cross-loading with latent effects, International Journal of Plasticity. 46 (2013) 130–142.

[75] K. Chung, M.G. Lee, D. Kim, C. Kim, M.L. Wenner, F. Barlat, Spring-back evaluation of automotive sheets based on isotropic-kinematic hardening laws and non-quadratic anisotropic yield functions: Part I: Theory and formulation, International Journal of Plasticity. 21 (2005) 861–882.

[76] Correlated Solutions, VIC-3D user manual, SC: Correlated Solutions , Columbia, 2005.

[77] LaVision GmbH, Product-manual for DaVis 8.2.0, StrainMaster, 2014.

[78] N. Chen, F. Qin, J. Wei, A Smoothing Algorithm for Strain Measurement by Digital Image Correlation Method, in: 2007 8th International Conference on Electronic Packaging Technology, IEEE, 2007.

[79] S. Yoneyama, Smoothing Measured Displacements and Computing Strains Utilising Finite Element Method, Strain. 47 (2011) 258–266.

[80] J. Zhao, P. Zeng, B. Pan, L. Lei, H. Du, W. He, Y. Liu, Y. Xu, Improved Hermite finite element smoothing method for full-field strain measurement over arbitrary region of interest in digital image correlation, Optics and Lasers in Engineering. 50 (2012) 1662–1671.

[81] J.-H. Kim, A. Serpantié, F. Barlat, F. Pierron, M.-G. Lee, Characterization of the post-necking strain hardening behavior using the virtual fields method, International Journal of Solids and Structures. 50 (2013) 3829–3842.

[82] S. Avril, P. Badel, A. Duprey, Anisotropic and hyperelastic identification of in vitro human arteries from full-field optical measurements, Journal of Biomechanics. 43 (2010) 2978–2985.

[83] L. Wang, G. Liu, T. Xing, H. Zhu, S. Ma, Boundary deformation measurement by mesh-based digital image correlation method, Applied Sciences (Switzerland). 11 (2021) 1–13.

[84] N. Promma, B. Raka, M. Grédiac, E. Toussaint, J.B. le Cam, X. Balandraud, F. Hild, Application of the virtual fields method to mechanical characterization of elastomeric materials, International Journal of Solids and Structures. 46 (2009) 698–715.

[85] K. Chung, M.-G. Lee, D. Kim, C. Kim, M.L. Wenner, F. Barlat, Spring-back evaluation of automotive sheets based on isotropic-kinematic hardening laws and non-quadratic anisotropic yield functions, International Journal of Plasticity. 21 (2005).

[86] V. Cvitanić, F. Vlak, Ž. Lozina, A finite element formulation based on non-associated plasticity for sheet metal forming, International Journal of Plasticity. 24 (2008).

[87] H. Choi, J.W. Yoon, Stress integration-based on finite difference method and its application for anisotropic plasticity and distortional hardening under associated and non-associated flow rules, Computer Methods in Applied Mechanics and Engineering. 345 (2019).

[88] H. Choi, S. Choi, S.-C. Kang, M.-G. Lee, Fully Implicit Stress Update Algorithm for Distortion-Based Anisotropic Hardening with Cross-Loading Effect: Comparative Algorithmic Study and Application to Large-Size Forming Problem, Applied Sciences. 11 (2021).

[89] R. Ahamad, M. Shajedul Karim, Study on derivation of shape functions in global coordinates and exact computation of element matrices for quadrilateral finite elements, IOSR Journal of Mathematics. 12 (2016) 90–103.

[90] Olek C. Zienkiewicz, Robert L. Taylor, Jian Z. Zhu, The Finite Element Method: its Basis and Fundamentals, Elsevier, 2013.

[91] Klaus-Jürgen Bathe, Finite element procedures, Prentice-Hall, New Jersey, 2006.

[92] X. Deng, A.J. Rosakis, Negative plastic flow and its prevention in elasto-plastic finite element computation, Finite Elements in Analysis and Design. 7 (1990) 181–191.

[93] M.A. Sutton, X. Deng, J. Liu, L. Yang, Determination of elastic-plastic stresses and strains from measured surface strain data, Experimental Mechanics. 36 (1996) 99–112.

[94] H. Zhang, S. Coppieters, C. Jiménez-Peña, D. Debruyne, Inverse identification of the post-necking work hardening behaviour of thick HSS through full-field strain measurements during diffuse necking, Mechanics of Materials. 129 (2019).

[95] M. ZANGANEH, Y.H. TAI, J.R. YATES, An optical method of measuring anisotropic deformation and necking in material testing, Fatigue & Fracture of Engineering Materials & Structures. 35 (2012).

[96] S. Coppieters, S. Cooreman, H. Sol, P. van Houtte, D. Debruyne, Identification of the post-necking hardening behaviour of sheet metal by comparison of the internal and external work in the necking zone, Journal of Materials Processing Technology. 211 (2011).

[97] Y. Choi, J. Lee, S.S. Panicker, H.-K. Jin, S.K. Panda, M.-G. Lee, Mechanical properties, springback, and formability of W-temper and peak aged 7075 aluminum alloy sheets: Experiments and modeling, International Journal of Mechanical Sciences. 170 (2020) 105344-.

[98] W. Wu, D. Zhou, D. Adamski, D. Young, Y.-W. Wang, Evaluation of Prog-Die Wear Properties on Bare DP1180 Steel, SAE International Journal of Engines. 10 (2017) 258–265.

[99] J. Hannula, D.A. Porter, A. Kaijalainen, J. Kömi, Evaluation of Mechanical Properties and Microstructures of Molybdenum and Niobium Microalloyed Thermomechanically Rolled High-Strength Press Hardening Steel, JOM. 71 (2019) 2405–2412.

[100] X. Chen, C. Niu, C. Lian, J. Lin, The Evaluation of Formability of the 3rd Generation Advanced High Strength Steels QP980 based on Digital Image Correlation Method, in: Procedia Engineering, Elsevier Ltd, 2017: pp. 556–561.

[101] K. Chung, W. Noh, X. Yang, H.N. Han, M.-G. Lee, Practical failure analysis of resistance spot welded advanced high-strength steel sheets, International Journal of Plasticity. 94 (2017).

[102] D. Mohr, S.J. Marcadet, Micromechanically-motivated phenomenological Hosford-Coulomb model for predicting ductile fracture initiation at low stress triaxialities, International Journal of Solids and Structures. 67–68 (2015) 40–55.

[103] S.K. Paul, S. Roy, S. Sivaprasad, H.N. Bar, S. Tarafder, Identification of Post-necking Tensile Stress–Strain Behavior of Steel Sheet: An Experimental Investigation Using Digital Image Correlation Technique, Journal of Materials Engineering and Performance. 27 (2018).

[104] S.K. Paul, S. Roy, S. Sivaprasad, S. Tarafder, A Simplified Procedure to Determine Post-necking True Stress–Strain Curve from Uniaxial Tensile Test of Round Metallic Specimen Using DIC, Journal of Materials Engineering and Performance. 27 (2018).

[105] H. Zhang, S. Coppieters, C. Jiménez-Peña, D. Debruyne, Inverse identification of the post-necking work hardening behaviour of thick HSS through full-field strain measurements during diffuse necking, Mechanics of Materials. 129 (2019).

[106] M. Grédiac, F. Pierron, Applying the Virtual Fields Method to the identification of elasto-plastic constitutive parameters, International Journal of Plasticity. 22 (2006) 602–627.

[107] W.M. Thomas, E.D. Nicholas, J.C. Needham, M.G. Murch, P. Templesmith, C.J. Dawes, Friction welding, 5460317, 1991.

[108] X. He, F. Gu, A. Ball, A review of numerical analysis of friction stir welding, Progress in Materials Science. 65 (2014) 1–66.

[109] C.M. Chen, R. Kovacevic, Finite element modeling of friction stir welding—thermal and thermomechanical analysis, International Journal of Machine Tools and Manufacture. 43 (2003).

[110] P. Ulysse, Three-dimensional modeling of the friction stir-welding process, International Journal of Machine Tools and Manufacture. 42 (2002).

[111] H.J. Liu, H. Fujii, M. Maeda, K. Nogi, Tensile properties and fracture locations of friction-stir-welded joints of 2017-T351 aluminum alloy, Journal of Materials Processing Technology. 142 (2003).

[112] L. Commin, M. Dumont, J.-E. Masse, L. Barrallier, Friction stir welding of AZ31 magnesium alloy rolled sheets: Influence of processing parameters, Acta Materialia. 57 (2009).

[113] S. Park, S. Yutaka, H. Kokawa, Effect of micro-texture on fracture location in friction stir weld of Mg alloy AZ61 during tensile test, Scripta Materialia. 49 (2003).

[114] N. Afrin, D.L. Chen, X. Cao, M. Jahazi, Microstructure and tensile properties of friction stir welded AZ31B magnesium alloy, Materials Science and Engineering: A. 472 (2008).

[115] Y. Zhang, Y.S. Sato, H. Kokawa, S.H.C. Park, S. Hirano, Microstructural characteristics and mechanical properties of Ti–6Al–4V friction stir welds, Materials Science and Engineering: A. 485 (2008).

[116] K. Gangwar, M. Ramulu, Friction stir welding of titanium alloys: A review, Materials & Design. 141 (2018).

[117] D. Myung, W. Noh, J.-H. Kim, J. Kong, S.-T. Hong, M.-G. Lee, Probing the Mechanism of Friction Stir Welding with ALE Based Finite Element Simulations and Its Application to Strength Prediction of Welded Aluminum, Metals and Materials International. 27 (2021) 650–666.

[118] P.L. Threadgilll, A.J. Leonard, H.R. Shercliff, P.J. Withers, Friction stir welding of aluminium alloys, International Materials Reviews. 54 (2009) 49–93.

[119] Y.-J. Kwon, I. Shigematsu, N. Saito, Mechanical Property Improvements in Aluminum Alloy through Grain Refinement using Friction Stir Process *, Materials Transactions. 45 (2004) 2304–2311.

[120] M.X. Milagre, N. v. Mogili, U. Donatus, R.A.R. Giorjão, M. Terada, J.V.S. Araujo, C.S.C. Machado, I. Costa, On the microstructure characterization of the AA2098-T351 alloy welded by FSW, Materials Characterization. 140 (2018).

[121] J.H. Kim, F. Barlat, C. Kim, K. Chung, Themo-mechanical and microstructural modeling of friction stir welding of 6111-T4 aluminum alloys, Metals and Materials International. 15 (2009).

[122] W. Gan, K. Okamoto, S. Hirano, K. Chung, C. Kim, R.H. Wagoner, Properties of Friction-Stir Welded Aluminum Alloys 6111 and 5083, Journal of Engineering Materials and Technology. 130 (2008).

[123] D. Kim, W. Lee, J. Kim, C. Kim, K. Chung, Formability evaluation of friction stir welded 6111-T4 sheet with respect to joining material direction, International Journal of Mechanical Sciences. 52 (2010).

[124] D. Rao, J. Heerens, G. Alves Pinheiro, J.F. dos Santos, N. Huber, On characterisation of local stress-strain properties in friction stir welded aluminium AA 5083 sheets using micro-tensile specimen testing and instrumented indentation technique, Materials Science and Engineering A. 527 (2010) 5018–5025.

[125] C. Cho, S. Choi, O.M. Kwon, S. Lee, J. hwan Kim, D. Kwon, Evaluation of Ballistic Limit Velocity Using Instrumented Indentation Test of 7xxx Aluminum Alloys After Friction Stir Welding, Metals and Materials International. (2020) 1–12.

[126] G. Cao, M. Ren, Y. Zhang, W. Peng, T. Li, A partitioning method for friction stir welded joint of AA2219 based on tensile test, Metals. 10 (2020) 65-.

[127] M.A. Sutton, J.H. Yan, S. Avril, F. Pierron, S.M. Adeeb, Identification of heterogeneous constitutive parameters in a welded specimen: Uniform stress and virtual fields methods for material property estimation, Experimental Mechanics. 48 (2008) 451–464.

[128] C. Leitão, I. Galvão, R.M. Leal, D.M. Rodrigues, Determination of local constitutive properties of aluminium friction stir welds using digital image correlation, Materials & Design. 33 (2012).

[129] H. Suthar, A. Bhattacharya, S.K. Paul, Determination of local constitutive properties in similar and dissimilar friction stir welded joints from DIC based surface strain measurement in two mutually perpendicular surfaces, Mechanics of Materials. 160 (2021) 103930-.

[130] C. Kim, J.-H. Kim, M.-G. Lee, Identification of Inhomogeneous Plastic Constitutive Models of Friction Stir Welded Aluminum Alloy Sheets Using Virtual Fields Method, in: Conference Proceedings of the Society for Experimental Mechanics Series, 2020: pp. 157–161.

[131] G. le Louëdec, F. Pierron, M.A. Sutton, C. Siviour, A.P. Reynolds, Identification of the Dynamic Properties of Al 5456 FSW Welds Using the Virtual Fields Method, Journal of Dynamic Behavior of Materials. 1 (2015) 176–190.

[132] G. le Louëdec, F. Pierron, M.A. Sutton, A.P. Reynolds, Identification of the Local Elasto-Plastic Behavior of FSW Welds Using the Virtual Fields Method, Experimental Mechanics. 53 (2013) 849–859.

[133] A. Shahmirzaloo, M. Farahani, M. Farhang, Evaluation of local constitutive properties of Al2024 friction stir-welded joints using digital image correlation method, The Journal of Strain Analysis for Engineering Design. (2020) 1–11.

Appendix A. Higher-order finite elements and shape functions

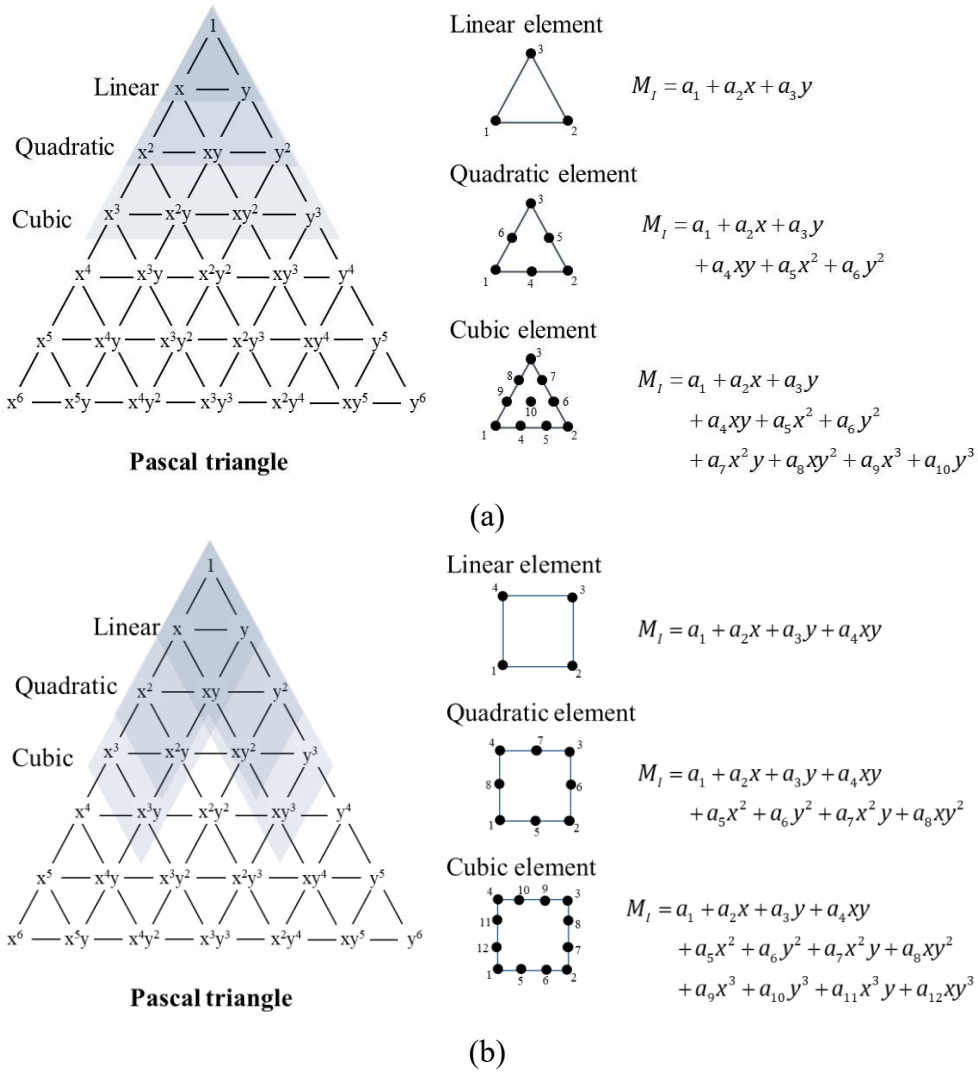

Fig. A.1. Pascal triangle, finite elements, and shape functions in general polynomial function form. (a) Triangular elements and (b) quadrilateral elements [90,91]

Linear element

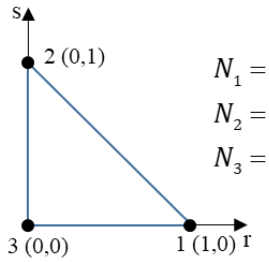

$$N_1 = L_1 = r$$
$$N_2 = L_2 = s$$
$$N_3 = L_3 = 1 - r - s$$

Quadratic element

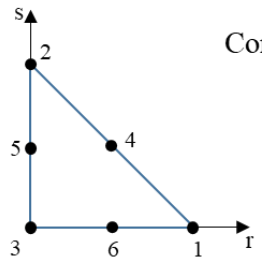

Corner nodes

$$N_1 = (2L_1 - 1)L_1$$
$$N_2 = (2L_2 - 1)L_2$$
$$N_3 = (2L_3 - 1)L_3$$

Mid-side nodes

$$N_4 = 4L_1L_2$$
$$N_5 = 4L_2L_3$$
$$N_3 = 4L_3L_1$$

Cubic element

Corner nodes

$$N_1 = \frac{1}{2}(3L_1 - 1)(3L_1 - 2)L_1$$
$$N_2 = \frac{1}{2}(3L_2 - 1)(3L_2 - 2)L_2$$
$$N_3 = \frac{1}{2}(3L_3 - 1)(3L_3 - 2)L_3$$

Internal node

$$N_{10} = 27L_1L_2L_3$$

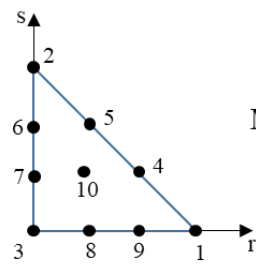

Mid-side nodes

$$N_4 = \frac{9}{2}L_1L_2(3L_1 - 1) \quad N_5 = \frac{9}{2}L_1L_2(3L_2 - 1)$$
$$N_6 = \frac{9}{2}L_2L_3(3L_2 - 1) \quad N_7 = \frac{9}{2}L_2L_3(3L_3 - 1)$$
$$N_8 = \frac{9}{2}L_3L_1(3L_3 - 1) \quad N_9 = \frac{9}{2}L_3L_1(3L_1 - 1)$$

Fig A.2. Local shape functions of triangular elements [90,91]

Linear element

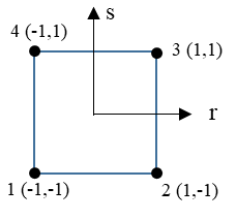

$$N_I = \frac{1}{4}(1 + r_I r)(1 + s_I s)$$

Quadratic element

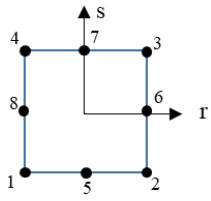

Corner nodes

$$N_I = \frac{1}{4}(1 + r_I r)(1 + s_I s)(r_I r + s_I s - 1)$$

Mid-side nodes

$$N_I = \frac{1}{2}(1 - r^2)(1 + s_I s) \quad \text{when } r_I = 0$$

$$N_I = \frac{1}{2}(1 - s^2)(1 + r_I r) \quad \text{when } s_I = 0$$

Cubic element

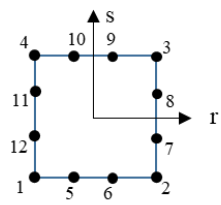

Corner nodes

$$N_I = \frac{1}{32}(1 + r_I r)(1 + s_I s)\left[9(s^2 + r^2) - 10\right]$$

Mid-side nodes

$$N_I = \frac{9}{32}(1 + r_I r)(1 - s^2)\left[1 + 9 s_I s\right] \quad \text{when } s = \pm 1,\ r = \pm\frac{1}{3}$$

$$N_I = \frac{9}{32}(1 + s_I s)(1 - r^2)\left[1 + 9 r_I r\right] \quad \text{when } s = \pm\frac{1}{3},\ r = \pm 1$$

*r_I ans s_I denotes natural coordinates of node number I

Fig. A.3. Local shape functions of quadrilateral elements (serendipity family) [90,91]

The shape functions in matrix form (M_I), the derivatives of basis function vector ($\frac{df_i}{dX_j}$), the matrix of natural nodal coordinates (r_{Ii}), and coefficients of local shape function (b_{iI}) of each element are given below. Note that the matrix form can be more efficient for the implementations, though the general polynomial form and matrix form of the shape function is identical. Also, the global and local shape functions are essentially the same types of function except for their coefficients. Therefore, only the global shape functions M_I and their derivatives are shown. in bellow.

Triangular linear element (T3)

$$M_I = \begin{pmatrix} 1 & X & Y \end{pmatrix} \begin{pmatrix} a_{1,1} & a_{1,2} & a_{1,3} \\ a_{2,1} & a_{2,2} & a_{2,3} \\ a_{3,1} & a_{3,2} & a_{3,3} \end{pmatrix} \tag{A.1}$$

$$\left(\frac{df_j}{dX_i} \right)^T = \begin{pmatrix} 0 & 1 & 0 \\ 0 & 0 & 1 \end{pmatrix} \tag{A.2}$$

$$r_{iI} = \begin{pmatrix} 1 & 0 & 0 \\ 0 & 1 & 0 \end{pmatrix} \tag{A.3}$$

$$b_{iI} = \begin{pmatrix} 1 & 0 & 1 \\ 0 & 1 & -1 \\ 0 & 0 & -1 \end{pmatrix} \tag{A.4}$$

Triangular quadratic element (T6)

$$M_I = \begin{pmatrix} 1 & X & Y & XY & X^2 & Y^2 \end{pmatrix} \begin{pmatrix} a_{1,1} & \cdots & a_{1,6} \\ \vdots & \ddots & \vdots \\ a_{6,1} & \cdots & a_{6,6} \end{pmatrix} \tag{A.5}$$

$$\left(\frac{df_j}{dX_i} \right)^T = \begin{pmatrix} 0 & 1 & 0 & Y & 2X & 2 \\ 0 & 0 & 1 & X & 0 & 2Y \end{pmatrix} \tag{A.6}$$

$$r_{il} = \begin{pmatrix} 1 & 0 & 0 & 0.5 & 0 & 0.5 \\ 0 & 1 & 0 & 0.5 & 0.5 & 0 \end{pmatrix} \tag{A.7}$$

$$b_{il} = \begin{pmatrix} 0 & 0 & 1 & 0 & 0 & 0 \\ -1 & 0 & -3 & 0 & 0 & 4 \\ 0 & -1 & -3 & 0 & 4 & 0 \\ 0 & 0 & 4 & 4 & -4 & -4 \\ 2 & 0 & 2 & 0 & 0 & -4 \\ 0 & 2 & 2 & 0 & -4 & 0 \end{pmatrix} \tag{A.8}$$

Triangular cubic element (T10)

$$M_I = \begin{pmatrix} 1 & X & Y & XY & X^2 & Y^2 & X^2Y & XY^2 & X^3 & Y^3 \end{pmatrix} \begin{pmatrix} a_{1,1} & \cdots & a_{1,10} \\ \vdots & \ddots & \vdots \\ a_{10,1} & \cdots & a_{10,10} \end{pmatrix} \tag{A.9}$$

$$\left(\frac{df_j}{dX_i} \right)^T = \begin{pmatrix} 0 & 1 & 0 & Y & 2X & 0 & 2XY & Y^2 & 3X^2 & 0 \\ 0 & 0 & 1 & X & 0 & 2Y & X^2 & 2XY & 0 & 3Y^2 \end{pmatrix} \tag{A.10}$$

$$r_{il} = \begin{pmatrix} 1 & 0 & 0 & 2/3 & 1/3 & 0 & 0 & 1/3 & 2/3 & 1/3 \\ 0 & 1 & 0 & 1/3 & 2/3 & 2/3 & 1/3 & 0 & 0 & 1/3 \end{pmatrix} \tag{A.11}$$

$$b_{il} = \begin{pmatrix} 0 & 0 & 1 & 0 & 0 & 0 & 0 & 0 & 0 & 0 \\ 1 & 0 & -5.5 & 0 & 0 & 0 & 0 & 9 & -4.5 & 0 \\ 0 & 1 & -5.5 & 0 & 0 & -4.5 & 9 & 0 & 0 & 0 \\ 0 & 0 & 18 & -4.5 & -4.5 & 4.5 & -22.5 & -22.5 & 4.5 & 27 \\ -4.5 & 0 & 9 & 0 & 0 & 0 & 0 & -22.5 & 18 & 0 \\ 0 & -4.5 & 9 & 0 & 0 & 18 & -22.5 & 0 & 0 & 0 \\ 0 & 0 & -13.5 & 13.5 & 0 & 0 & 13.5 & 27 & -13.5 & -27 \\ 0 & 0 & -13.5 & 0 & 13.5 & -13.5 & 27 & 13.5 & 0 & -27 \\ 4.5 & 0 & -4.5 & 0 & 0 & 0 & 0 & 13.5 & -13.5 & 0 \\ 0 & 4.5 & -4.5 & 0 & 0 & -13.5 & 13.5 & 0 & 0 & 0 \end{pmatrix} \tag{A.12}$$

Quadrilateral linear element (Q4)

$$M_I = \begin{pmatrix} 1 & X & Y & XY \end{pmatrix} \begin{pmatrix} a_{1,1} & \cdots & a_{1,4} \\ \vdots & \ddots & \vdots \\ a_{4,1} & \cdots & a_{4,4} \end{pmatrix} \tag{A.13}$$

$$\left(\frac{df_j}{dX_i} \right)^T = \begin{pmatrix} 0 & 1 & 0 & Y \\ 0 & 0 & 1 & X \end{pmatrix} \tag{A.14}$$

$$r_{iI} = \begin{pmatrix} -1 & 1 & 1 & -1 \\ -1 & -1 & 1 & 1 \end{pmatrix} \tag{A.15}$$

$$b_{iI} = \begin{pmatrix} 0.25 & 0.25 & 0.25 & 0.25 \\ -0.25 & 0.25 & 0.25 & -0.25 \\ -0.25 & -0.25 & 0.25 & 0.25 \\ 0.25 & -0.25 & 0.25 & -0.25 \end{pmatrix} \tag{A.16}$$

Quadrilateral quadratic element (Q8)

$$M_I = \begin{pmatrix} 1 & X & Y & XY & X^2 & Y^2 & X^2Y & XY^2 \end{pmatrix} \begin{pmatrix} a_{1,1} & \cdots & a_{1,8} \\ \vdots & \ddots & \vdots \\ a_{8,1} & \cdots & a_{8,8} \end{pmatrix} \tag{A.17}$$

$$\left(\frac{df_j}{dX_i}\right)^T = \begin{pmatrix} 0 & 1 & 0 & Y & 2X & 0 & 2XY & Y^2 \\ 0 & 0 & 1 & X & 0 & 2Y & X^2 & 2XY \end{pmatrix} \tag{A.18}$$

$$r_{il} = \begin{pmatrix} -1 & 1 & 1 & -1 & 0 & 1 & 0 & -1 \\ -1 & -1 & 1 & 1 & -1 & 0 & 1 & 0 \end{pmatrix} \tag{A.19}$$

$$b_{il} = \begin{pmatrix} -0.25 & -0.25 & -0.25 & -0.25 & 0.5 & 0.5 & 0.5 & 0.5 \\ 0 & 0 & 0 & 0 & 0 & 0.5 & 0 & -0.5 \\ 0 & 0 & 0 & 0 & -0.5 & 0 & 0.5 & 0 \\ 0.25 & -0.25 & 0.25 & -0.25 & 0 & 0 & 0 & 0 \\ 0.25 & 0.25 & 0.25 & 0.25 & -0.5 & 0 & -0.5 & 0 \\ 0.25 & 0.25 & 0.25 & 0.25 & 0 & -0.5 & 0 & -0.5 \\ -0.25 & -0.25 & 0.25 & 0.25 & 0.5 & 0 & -0.5 & 0 \\ -0.25 & 0.25 & 0.25 & -0.25 & 0 & -0.5 & 0 & 0.5 \end{pmatrix} \tag{A.20}$$

Quadrilateral cubic element (Q12)

$$M_I = \begin{pmatrix} 1 & X & Y & XY & X^2 & Y^2 & X^2Y & XY^2 & X^3 & Y^3 & X^3Y & XY^3 \end{pmatrix} \begin{pmatrix} a_{1,1} & \cdots & a_{1,12} \\ \vdots & \ddots & \vdots \\ a_{12,1} & \cdots & a_{12,12} \end{pmatrix} \tag{A.21}$$

$$\left(\frac{df_j}{dX_i}\right)^T = \begin{pmatrix} 0 & 1 & 0 & Y & 2X & 0 & 2XY & Y^2 & 3X^2 & 0 & 3X^2Y & Y^3 \\ 0 & 0 & 1 & X & 0 & 2Y & X^2 & 2XY & 0 & 3Y^2 & X^3 & 3XY^2 \end{pmatrix} \tag{A.22}$$

$$r_{il} = \begin{pmatrix} -1 & 1 & 1 & -1 & -1/3 & 1/3 & 1 & 1 & 1/3 & -1/3 & -1 & -1 \\ -1 & -1 & 1 & 1 & -1 & -1 & -1/3 & 1/3 & 1 & 1 & 1/3 & -1/3 \end{pmatrix} \tag{A.23}$$

$$b_{il} = \frac{1}{32}\begin{pmatrix} -10 & -10 & -10 & -10 & 9 & 9 & 9 & 9 & 9 & 9 & 9 & 9 \\ 10 & -10 & -10 & 10 & -27 & 27 & 9 & 9 & 27 & -27 & -9 & -9 \\ 10 & 10 & -10 & -10 & -9 & -9 & -27 & 27 & 9 & 9 & 27 & -27 \\ -10 & 10 & -10 & 10 & 27 & -27 & -27 & 27 & 27 & -27 & -27 & 27 \\ 9 & 9 & 9 & 9 & -9 & -9 & 0 & 0 & -9 & -9 & 0 & 0 \\ 9 & 9 & 9 & 9 & 0 & 0 & -9 & -9 & 0 & 0 & -9 & -9 \\ -9 & -9 & 9 & 9 & 9 & 9 & 0 & 0 & -9 & -9 & 0 & 0 \\ -9 & 9 & 9 & -9 & 0 & 0 & -9 & -9 & 0 & 0 & 9 & 9 \\ -9 & 9 & 9 & -9 & 27 & -27 & 0 & 0 & -27 & 27 & 0 & 0 \\ -9 & -9 & 9 & 9 & 0 & 0 & 27 & -27 & 0 & 0 & -27 & 27 \\ 9 & -9 & 9 & -9 & -27 & 27 & 0 & 0 & -27 & 27 & 0 & 0 \\ 9 & -9 & 9 & -9 & 0 & 0 & 27 & -27 & 0 & 0 & 27 & -27 \end{pmatrix} \quad \text{(A.24)}$$

Appendix B. Example of FE based displacements reconstruction: linear quadrilateral elements

In this section, reconstruction full-field displacements with a linear quadrilateral element (Q4) is presented as an example. The global shape function of the Q4 element can be given as follows.

$$\mathrm{M_I}\left(X,Y\right)=\left(f_\mu\right)^T a_{\mu I}=a_{1I}+a_{2I}X+a_{3I}Y+a_{4I}XY \tag{B.1}$$

where f_i is the basis function vector of global Q4 shape function, which is given as

$$\left(f_i\right)^T=\begin{bmatrix}1 & X & Y & XY\end{bmatrix}. \tag{B.2}$$

and the coefficients of the global shape function can be obtained using $\delta_{JI}=F_{Ji}a_{iI}$ as below.

$$a_{iI}=F_{Ii}^{-1}=\begin{pmatrix}a_{11} & a_{12} & a_{13} & a_{14}\\ a_{21} & a_{22} & a_{23} & a_{24}\\ a_{31} & a_{32} & a_{33} & a_{34}\\ a_{41} & a_{42} & a_{43} & a_{44}\end{pmatrix}=\begin{pmatrix}1 & X_1 & Y_1 & X_1Y_1\\ 1 & X_2 & Y_2 & X_2Y_2\\ 1 & X_3 & Y_3 & X_3Y_3\\ 1 & X_4 & Y_4 & X_4Y_4\end{pmatrix}^{-1} \tag{B.3}$$

where $\mathrm{X_1}$ to $\mathrm{X_4}$ and $\mathrm{Y_1}$ to $\mathrm{Y_4}$ are the initial nodal positions of Q4 mesh in global coordinates, and subscripts 1 to 4 denote the local nodal index of a single Q4 element. In other words, coefficients of the global shape functions are equal to the inverse of the basis function matrix constructed with undeformed nodal coordinates of an element.

Using global shape functions, the positions of the natural coordinates matrix of full-field data points are given as follows.

$$\begin{pmatrix} r_1^d & s_1^d \\ r_2^d & s_2^d \\ \vdots & \vdots \\ r_m^d & s_m^d \end{pmatrix} = \begin{pmatrix} 1 & X_1^d & Y_1^d & X_1^d Y_1^d \\ 1 & X_2^d & Y_2^d & X_2^d Y_2^d \\ & & \vdots & \\ 1 & X_m^d & Y_m^d & X_m^d Y_m^d \end{pmatrix} \begin{pmatrix} a_{11} & a_{12} & a_{13} & a_{14} \\ a_{21} & a_{22} & a_{23} & a_{24} \\ a_{31} & a_{32} & a_{3,3} & a_{34} \\ a_{41} & a_{42} & a_{43} & a_{44} \end{pmatrix} \begin{pmatrix} r_1^n & s_1^n \\ r_2^n & s_2^n \\ r_3^n & s_3^n \\ r_4^n & s_4^n \end{pmatrix} . \quad \text{(B.4)}$$

And, the local shape functions are

$$N_I = \left(\mathrm{g}_i\right)^T \cdot b_{iI} = b_{1I} + b_{2I} r + b_{3I} s + b_{4I} rs \ . \quad \text{(B.5)}$$

Here, $\mathrm{g_i}$ is the basis function vector of the local Q4 shape functions, which are given as,

$$\left(\mathrm{g}_i\right)^T = \begin{bmatrix} 1 & r & s & rs \end{bmatrix} . \quad \text{(B.6)}$$

And, the coefficients of local shape functions can be given as,

$$b_{iI} = \begin{pmatrix} 0.25 & 0.25 & 0.25 & 0.25 \\ -0.25 & 0.25 & 0.25 & -0.25 \\ -0.25 & -0.25 & 0.25 & 0.25 \\ 0.25 & -0.25 & 0.25 & -0.25 \end{pmatrix} . \quad \text{(B.7)}$$

Note that coefficients of local shape functions are fixed values for each element since the nodes in a FE element are fixed in the natural coordinates.

The displacements of the full-field measurement points in the element can be described using the local shape function as follows.

$$\begin{pmatrix} u_1^d & v_1^d \\ u_2^d & v_2^d \\ \vdots & \vdots \\ u_m^d & v_m^d \end{pmatrix} = \begin{pmatrix} 1 & r_1^d & s_1^d & r_1^d s_1^d \\ 1 & r_2^d & s_2^d & r_2^d s_2^d \\ & & \vdots & \\ 1 & r_m^d & s_m^d & r_m^d s_m^d \end{pmatrix} \begin{pmatrix} b_{11} & b_{12} & b_{13} & b_{14} \\ b_{21} & b_{22} & b_{23} & b_{24} \\ b_{31} & b_{32} & b_{33} & b_{34} \\ b_{41} & b_{42} & b_{43} & b_{44} \end{pmatrix} \begin{pmatrix} u_1^n & v_1^n \\ u_2^n & v_2^n \\ u_3^n & v_3^n \\ u_4^n & v_4^n \end{pmatrix} \tag{B.8}$$

where the matrix of local shape function N_{Ii}^e is

$$N_{Ii}^e = \begin{pmatrix} 1 & r_1^d & s_1^d & r_1^d s_1^d \\ 1 & r_2^d & s_2^d & r_2^d s_2^d \\ & & \vdots & \\ 1 & r_m^d & s_m^d & r_m^d s_m^d \end{pmatrix} \begin{pmatrix} b_{11} & b_{12} & b_{13} & b_{14} \\ b_{21} & b_{22} & b_{23} & b_{24} \\ b_{31} & b_{32} & b_{33} & b_{34} \\ b_{41} & b_{42} & b_{43} & b_{44} \end{pmatrix}. \tag{B.9}$$

N_{Ii}^e can be easily calculated since the local coordinates of data points and coefficients of local shape functions are all-known. After assembling of N_{Jj}^g from N_{Ii}^e of each element, the least-square operator can be performed, and displacements are reconstructed into Q4 FE mesh.

Korean abstract

본 연구에서는 구성방정식 변수 역해석 최적화를 위한 새로운 유한요소 기반 가상필즈법 (Finite element-based virtual fields method, FE-VFM) 을 제안하였다. FE-VFM에서는 전 영역 측정법(Full-field measurement)을 통해 측정된 실험 변위를 전역 및 형상 함수 (global and local shape function) 를 이용해 유한요소 메시로 재구축한다. 구성방정식 변수 최적화 과정에서는 유한요소에 맵핑된 변위를 기반으로 가상일의 원리 (Principle of virtual work) 수식을 풀이하는데, 이때 FE-VFM은 내부 가상일 (Internal virtual work)을 적분 시 가우스 구적법을 활용한다.

새롭게 제안한 FE-VFM을 검증하기 위하여, 잘 디자인된 민감도 분석 연구가 진행되었다. 민감도 분석 연구에는 유한요소해석으로 생성된 이상적인 변형 정보가 FE-VFM의 입력 정보로 활용되었으며, 민감도 분석은 비등방 선형 탄성 재료와 등방 탄소성 재료 두 가지에 대해 수행하였다. 민감도 분석 조건으로 변위장 재구축을 위한 유한요소의 크기 및 차수, 그리고 가우스 구적법의 차수에 대한 민감도 분석을 수행행하였다. 정량적인 분석을 위해 내부 가상일과 외부 가상일의 잔차를 계산하여 각 조건을 평가하였다. 이방성 선형 탄성 소재 조건의 경우, 가상일 잔차가 유한요소의 크기 및 차수에 크게 영향을 받지 아니하였으며, 가우스 구적법 차수 많이 제한적인 범위에서 약간의 정확도를 향상시켰다. 반면, 소성 물성의 경우, 유한요소의 크기, 차수, 그리고 가우스 구적법 차수 모두 결과에 크게 영향을 주었다. 이러한 차이는

선형 탄성의 경우 변형의 비선형성이 작은 반면, 탄소성 소재의 경우 국부적이고 비선형성이 큰 변형이 발생에 기인한 것으로 보인다.

한편, FE-VFM의 응용으로서 금속 판재의 균질, 그리고 비균질한 소성 경화 거동 측정이 수행되었다. 첫번째 응용으로서 고강도강의 소성 경화 거동을 측정하였다. 이 응용 연구에서는 FE-VFM의 소성 물성 측정 정밀도를 높이기 위하여 실제 변위에 기반한 의사 실제 변형장(Pesudo-real deformation field, PDF)을 새로운 형태의 가상변위로 제안하였다. 이후 응용으로서 PDF와 FE-VFM을 함께 활용하여 프레스 경화 강(press hardened steel)의 소성 경화 거동을 측정하였다. FE-VFM 적용을 위해서는 노치 인장실험 (notched tensile tests)이 수행되었다. 그 결과 요소 크기가 크고 고차 요소로 이루어진 유한요소메시를 활용 시, 비교적 낮은 품질의 전영역 측정 결과를 활용하여도 성공적으로 변위장을 모사할 수 있음을 확인하였다. 나아가, 이러한 FE-VFM의 효과로 인해 프레스 경화강의 소성 경화 거동이 성공적으로 측정될 수 있음을 확인하였다.

측정된 결과를 검증하기 위해, U 노치 인장 실험(U notched tensile tests)을 수행하였다. 실험 결과와 유한 요소해석 결과를 비교하였을 때, FE-VFM으로 측정된 물성을 유한요소해석 결과가 일반적인 표준 일축 실험을 기반으로 한 것 보다 하중-변위 곡선이 실험과 더 잘 일치함을 확인하였다. 이는 크게 두 가지 이유에 기인한다. 첫째, 일축인장 실험 으로 항복강도를 결정할 때 사용 사용하는 0.2% 오프셋 방법은 매우 큰 강도의 프레스 경화 강의 항복점 근처의 탄성에서 소성으로의 비선형적인 변화 거동을 무시하게 되는 반면, FE-VFM의 경우 임의이 항복강도 결정 기준을 사용하지 않고, 비용 함수(cost function)

값을 비선형적으로 최적화하는 과정에서 탄성한계점이 항복강도로 결정된다. 그러므로 U 노치 인장 결과에서 초반 하중-변위 거동이 FE-VFM을 통해 계산된 유한요소해석 결과가 더 잘 맞게된다. 둘째, 일반적인 일축 인장에서 UTS 이후에는 넥킹(necking) 현상이 일어나므로, UTS 전 까지의 실험 데이터를 활용하여 소성 경화식을 최적화 하고 그 이후는 외삽으로 예측하게 된다. 그러나 연구된 프레스 경화 강은 균일 연신율이 5% 내외로 짧아, UTS 이후 큰 변형율에서의 실험 정보가 부족하다. 반면 FE-VFM의 경우 일축인장에서는 쓸 수 없었던 균일 연신율 이후의 응력-변위 정보도 사용하여 소성 경화식을 최적화 할 수 있으며, 따라서 U 노치 실험의 하중-변위 곡선이 최대값 이후에서 FE-VFM 결과를 기반으로 한 예측 결과가 일축인장보다 더 잘 맞을 수 있었다.

또한, 고등 응용으로서 마찰 교반 용접(Firction stir welding, FSW)된 알루미늄 판재의 비균질 소성 경화거동을 FE-VFM을 활용하여 측정하였다. 이 연구에서는 먼저 용접영향부(weld affected zone, WAZ) 경계를 확인한 뒤, 확인된 용접영향부 내의 국부 물성 분포를 측정하는 2단계 측정 방법이 활용되었다. 관심영역을 하위도메인으로 구분하는 접근법과 구성방정식 변수를 각 하위도메인 안에서 이차 함수로 보간하는 기법이 함께 사용되었다. 이러한 비선형성이 심한 문제를 적절히 풀기 위하여, 가상 필즈를 하위도메인 내의 서로 다른 위치의 정보를 강화 할 수 있는 정규 분포 함수로 정의하였다.

이러한 FE-VFM 기반 방법론을 유한요소해석 데이터 기반으로 실현가능성을 평가 및 검증하였다. 실현 가능성 검증에서 일반적인 다항식

함수로 정의된 가상 필즈를 사용할 경우 구성방정식 상수 분포가 유니크니스 문제(uniqueness problem)으로 인해 특정 값으로 제대로 결정되지 않음을 확인하였다. 그리고 구성방정식 상수 보간 및 정규 분포 함수로 정의된 가상 필즈의 높은 비선형성으로 인해 고차 가우스 구적 사용이 필수임을 확인하였다. 검증된 방법론을 적용한 결과, 마찰교반용접 된 AA6061-T6 판재 물성을 적절히 평가할 수 있었다. 그 결과 1200 및 1600 RPM 각각 용접 영향부가 -9 mm 부터 12 mm, 그리고 9 mm 부터 12 mm로 확인되었다. 또한, 용접 영향부 내의 알루미늄 합금은 강도는 전반적으로 약해진 반면, 연성은 모재 대비 증가한 것을 확인할 수 있었다. 마지막으로 검증 실험을 진행하여, FE-VFM으로 도출된 물성을 활용한 유한요소해석 결과와 실험값을 비교하였다. 그 결과 실험과 유한요소해석으로 예측된 결과가 잘 일치함을 확인하였다. 이를 통하여 FE-VFM을 통해 마찰 교반 용접된 알루미늄 합금의 비균질 경화 거동을 정확히 측정할 수 있음을 확인하였다.

결론적으로, 두 가지 응용 연구는 FE-VFM으로 통상의 방법으로 얻기 어렵거나 번거로운 재료의 기계적 물성을 효과적이고 정확하게 얻을 수 있음을 보여주었다.

핵심어: 가상필즈법, 유한요소, 전 영역 측정 평활화, 구성방정식, 소성 경화, 비균질 국부 물성 평가

학번: 2018-39025

감사의 글

드디어 긴 학위과정이 끝났습니다. 사실 잠시 전까지도 제가 박사가 된다는, 멀게만 느껴졌던 학위과정의 마침표가 찍혔다는 사실이 믿기지 않았습니다. 연구실에 앉아 학위논문을 마지막으로 점검하고, 이제 이렇게 감사의 글을 적으니 드디어 끝이다 하는 실감이 나며 가슴이 두근거립니다. 지난 6년간을 돌아보면 다시 한다면 더 잘할 수 있었을 텐데 하는 아쉬운 순간들과 함께 약간의 그리움과 아련함이 섞인 추억들이 생각납니다. 그리고 무엇보다 저를 도와주시고 응원해주셨던 많은 분들께 감사함을 느낍니다.

누구보다 먼저 제게 학문의 길을 밟을 수 있는 기회를 주시고, 제 학위과정 끝까지 지도와 지원을 아끼지 않으셨던 지도교수님이신 이명규 교수님께 감사를 드립니다. 아무 것도 모르던 학부생으로 마지막 학기 때, 저를 연구실에 받아주셨던 교수님의 말씀이 생각납니다. 학부 연구생으로 지원해 놓고는 예비 지도교수 수업에서 맨 앞에 앉아 꾸벅꾸벅 졸고 있는 모습을 보고 있노라면, 이 녀석을 받은 것이 잘한 일인가 하는 생각에 계속 어이없었다 하셨지요. 돌이켜보면 이것을 시작으로 제가 학위 과정동안 이런저런 사고를 참 많이 저질렀습니다. 연구실에 지각도 잦고 다양한 기상천외한 사고를 저지르는 학생을 인내심으로 기다려주시고, 너그럽게 시간을 주셔서 참 감사합니다. 또한 학문적으로도 많은 것을 배웠습니다. 주어진 공학적 문제를 어떻게 탐구하고 해결해 가야 하는지 방향성을 일러주셨고, 무엇보다 연구자는 주어진 문제의 결과를 내는 것이 아니라 그 결과를 다각적으로

분석할 줄 알아야한다며 언제나 강조하셨던 그 말씀으로 제가 성장할 수 있었습니다.

또한 학위 과정 중, 제 연구에 직간접적으로 많은 것을 알려주셨던 두 분의 선배 연구자님께 감사드립니다. 우선 노우람 박사님께 감사드립니다. 지금은 없어진 좁디좁은 고려대학교 공학별관 연구실에서, 여름에는 에어컨도 시원치 않아 땀을 뻘뻘 흘리며 함께했었던 일이 생각납니다. 그 시절 기초가 부족한 저희에게 유한요소해석은 무엇인지, 역학은 어떻게 이해해야 하는 지, 열정을 다해 공별에 있는 학생들에게 설명해주시던 모습이 여전이 눈에 선합니다. 무엇보다 이 졸업논문에는 담기지 못했지만 제 학위과정 중 절반의 연구 제목이었던 연성파괴모델의 기초를 노우람 박사님께서 전수해 주셨습니다. 너무나도 감사드립니다.

두 번째로 이 학위논문의 주제인 가상필즈법에 전문가이신 김진환 교수님께 감사드립니다. 김진환 교수님께서 역해석법의 기초, 참고할 문헌을 적절히 소개해주시고, 때론 제가 하는 연구에 아낌없는 조언과 지지를 주셔서 이 학위 논문을 무사히 쓸 수 있었습니다. 그리고 김진환 교수님께서 연구하셨던 예시 문제 자료와 직접 작성하셨던 코드를 바탕으로 제가 가상필즈법을 배웠고, 또 2019 SEM 학회 교수님과 나누었던 논의들에서 얻은 아이디어가 이 학위논문 주제의 시발점이 될 수 있었습니다. 진심으로 감사드립니다.

그리고 바쁘신 중에 제 학위 논문의 심사위원이 되어주셨던 한흥남 교수님, 유웅열 교수님, 김대용 박사님께 감사드립니다.

6년 반 동안 함께 했던 연구실 동료들도 고마웠습니다. 연구실 동료 중에서는 가장 먼저 정우진씨에게 감사를 표하고 싶네요. 우진이형! 고려대에서 연구실 문을 열었을 때부터 마지막 졸업때 까지 함께해줘서 고마워요. 학부 한 한번 후배인데도 까탈스럽고, 귀찮게 굴고, 또 한편으로는 약간 무례하기까지 했던 나에게 잘 맞장구 쳐 줘서 고마워요. 학위 시작 때부터 친구처럼 편하면서도 또 연구실에 유일한 형으로 많이 의지했습니다. 그리고 먼저 석사로 졸업해서 지금은 연구실에 없지만 고려대 시절 창립 멤버였던 재민이! 처음 학부연구생으로 시작했을 때, 교수님께서 낡은 책상만 덩그러니 있는 공별 방에 같이 가셔서는 이제 여기가 연구실이다 했을 때 얼마나 어리둥절하고 막막했는지 몰라. 너와 우진이형이 함께해줘서 아무것도 없던 상태에서 연구실을 하나씩 같이 꾸며갈 수 있었어. 아쉽게도 연구실을 서울대로 옮기며 새로 시작하게 되었지만 큰 힘이 되었어, 고마워. 너와 동준이 그리고 내가 shames 책으로 고체역학을 서로 아무것도 모르면서 돌아가며 준비해서 공부하고, 또 석동윤 박사님께 같이 아바쿠스 사용법 배우던 것이 기억난다. 동준아! 그 때가 힘들었지만 그립네.

후배 중에서는 가장 내가 많이 의지했던 홍진이. 내가 언제나 너에게 말하지만, 네가 투덜투덜하면서도 가장 같이 일을 잘해줘서 후배들 중에서는 편하게 너에게 많은 부분을 부탁했었어. 부족한 선배 참고 따라주느라 항상 미안하고 고마웠다. 부족한 내가 방장 역할을 하는 동안 네가 큰 힘이 되었어. 그리고 자주 티격태격 했던 기정이. 우리가 서로 많이 달라서 많이 충돌했는데 이제는 어느덧 서로에게 많이 익숙해졌네. 나와 싸우면서도 그래도 다시

화해하기도 하고 서로 맞춰가며 지내줘서 고마워. 마지막으로 유미. 내가 가끔 선 넘는 농담을 하는데도 또 금방 이해하고 즐겁게 여러 가지로 이야기를 나눈 기억이 많네. 그리고 유미, 기정 그리고 Kaushik 박사와 넷이 함께 갔던 즐거웠던 제주도 학회 출장이 크게 기억에 남는다. 여러가지로 고마워. 그리고 나에게는 영원한 연구실 막내, 경문이. 처음 학부연구생으로 들어왔을 때부터 내가 많이 괴롭혔지. 서울대로 와서는 다들 졸업이 가깝다고 너에게 연구실 잡무가 집중되어 언제나 고맙고 미안했다. 연구적으로도 새로운 것을 금방 스스로 잘 하는 너 같은 후배가 있어 든든했다.

서울대 옮겨와서 생긴 후배들, 진흥, 찬미, 재승, 서준, 정윤, 건진, 성환. 까다롭고 톡톡 튀는 말투에, 참견하기 좋아하는 선배에게 맞춰주며 지내느라 고생 많았고, 많은 나이차이에도 친밀하게 대해주어 고마웠다. 그리고 나머지 함께했었던 연구실 멤버들, 조금 멀리 있지만 같이한 방준호부터, 석동윤 박사님, 이정연 박사님, 김원재 박사님, Dr. Kaushik and Dr. Shamik, 서정환, 곽수현, 정영민 대위님, 이형림 형님, 김혜진씨, 김지영님, 모두 감사하고 즐거운 시간이었습니다. 코로나 19가 아니었다면 엠티도 더 자주 가고 좋은 추억을 많이 만들었을 텐데, 너무 아쉽습니다. 그리고 같은 연구실은 아니지만 많은 일을 같이 했던 이충안 박사님, 김주희씨, 예정원씨, 재미있는 연구 같이 해볼 수 있어서 감사했습니다.

가족들에게도 감사합니다. 대학원을 진학하겠다 말을 꺼냈을 때, 내심 걱정하시면서도 언제나 기도하고 응원해주셨던 부모님. 학위 과정 동안 바쁘다는 핑계로 전화도 자주 안 드리고 무심했던 장남을 이해하고

격려해주셔서 감사합니다. 제가 박사학위를 드디어 받게 되었다 전해드렸을 때, 두 분이 누구보다 자랑스러워하시고 기뻐해주셔서 뿌듯했습니다. 그리고 학부 때부터 고려대 석사 학위 마칠 때 까지 팍팍한 서울살이를 같이 해줬던 동생 온유. 까칠한 말투에 이기적으로 굴 때도 많은 형과 함께 오랫동안 단 둘이 지내느라 고생 많았다. 네가 서울에서 함께 살아서 때론 힘들고 바쁘단 핑계로 이기적으로 집안일도 미루기도 하고, 또 연구에 지칠 때 같이 영화도 보러 다니고 음식도 해먹으며 활기를 충전할 수 있어 의지가 많이 되었다. 진심으로 고맙다. 그리고 막내 은빈이도 사랑한다.

마지막으로 매사 만물을 주관하시는 존귀하신 사랑의 하나님. 부족한 저에게 총명과 의지, 그리고 무엇보다 학위 공부를 할 수 있는 기회를 주시고, 매 순간 저를 축복으로 이끌어주셔서 감사드리나이다. 제게 주신 이 모든 은혜에 감사드리며 모든 영광과 찬양을 주께 돌리옵니다. 하나의 끝마침과 새로운 시작이 기다리는 제게, 앞으로도 주님께서 주신 이 능력으로 제 이름 찬양에 걸맞도록 제 삶이 하나님께 영광 돌릴 수 있도록 인도와 사랑을 주시옵소서.